LA-UR-16-26212
Approved for public release; distribution is unlimited.

Title: Crystalline and Crystalline International Disposal Activities

Author(s): Viswanathan, Hari S.
Chu, Shaoping
Dittrich, Timothy M.
Hyman, Jeffrey De'Haven
Karra, Satish
Makedonska, Nataliia
Reimus, Paul William

Intended for: Report

Issued: 2017-03-06 (rev.1)

Crystalline and Crystalline International Disposal Activities

Fuel Cycle Research & Development

Prepared for
U.S. Department of Energy
Used Fuel Disposition
Hari Viswanathan,
Shaoping Chu, Timothy Dittrich,
Jeffrey Hyman, Satish Karra,
Natallia Makendonska, Paul Reimus
Los Alamos National Laboratory

August 2016
FCRD-UFD-2016-000626
LA-UR-16-26212

FCT Quality Assurance Program Document

Appendix E
FCT Document Cover Sheet

Name/Title of Deliverable/Milestone	LANL input to SNL L2 MS: Report entitled - "Crystalline and Crystalline International Disposal Activities"
Work Package Title and Number	DR Crystalline Disposal R&D – LANL: FT-16LA08030302, FT-16LA0803030
Work Package WBS Number	**1.02.08.03.03**
Responsible Work Package Manager	Hari S. Viswanathan (Name/Signature)
Date Submitted	August 2016

Quality Rigor Level for Deliverable/Milestone	☐ QRL-3	☐ QRL-2	☐ QRL-1 ☐ Nuclear Data	☒ N/A*

This deliverable was prepared in accordance with Los Alamos National Laboratory
(Participant/National Laboratory Name)

QA program which meets the requirements of
☒ DOE Order 414.1 ☐ NQA-1-2000

This Deliverable was subjected to:

☐ Technical Review

Technical Review (TR)

Review Documentation Provided

☐ Signed TR Report or,
☐ Signed TR Concurrence Sheet or,
☒ Signature of TR Reviewer(s) below

Name and Signature of Reviewers

Phil Stauffer

Philip H Stauffer Digitally signed by Philip H Stauffer DN: cn=Philip H Stauffer, o=Los Alamos National Laboratory, ou=EES-16, email=stauffer@lanl.gov, c=US Date: 2016.08.18 09:20:32 -06'00'

☐ Peer Review

Peer Review (PR)

Review Documentation Provided

☐ Signed PR Report or,
☐ Signed PR Concurrence Sheet or,
☐ Signature of PR Reviewer(s) below

*Note: In some cases there may be a milestone where an item is being fabricated, maintenance is being performed on a facility, or a document is being issued through a formal document control process where it specifically calls out a formal review of the document. In these cases, documentation (e.g., inspection report, maintenance request, work planning package documentation or the documented review of the issued document through the document control process) of the completion of the activity along with the Document Cover Sheet is sufficient to demonstrate achieving the milestone. QRL for such milestones may be also be marked N/A in the work package provided the work package clearly specifies the requirement to use the Document Cover Sheet and provide supporting documentation.

This page left blank intentionally.

CONTENTS

FIGURES

TABLES

CRYSTALLINE AND CRYSTALLINE INTERNATIONAL ACTIVITIES

EXECUTIVE SUMMARY

This report presents the results of work conducted between September 2015 and July 2016 at Los Alamos National Laboratory in the crystalline disposal and crystalline international disposal work packages of the Used Fuel Disposition Campaign (UFDC) for DOE-NE's Fuel Cycle Research and Development program. Los Alamos focused on two main activities during this period: Discrete fracture network (DFN) modeling to describe flow and radionuclide transport in complex fracture networks that are typical of crystalline rock environments, and a comprehensive interpretation of three different colloid-facilitated radionuclide transport experiments conducted in a fractured granodiorite at the Grimsel Test Site in Switzerland between 2002 and 2013. Chapter 1 presents the results of the DFN work and is divided into three main sections: (1) we show results of our recent study on the correlation between fracture size and fracture transmissivity (2) we present an analysis and visualization prototype using the concept of a flow topology graph for characterization of discrete fracture networks, and (3) we describe the Crystalline International work in support of the Swedish Task Force. Chapter 2 presents interpretation of the colloid-facilitated radionuclide transport experiments in the crystalline rock at the Grimsel Test Site.

In the first section of Chapter 1, we evaluate the correlation between fracture size and fracture transmissivity correlation. We characterize how different fracture size-transmissivity relationships influence flow and transport simulations through sparse three- dimensional discrete fracture networks, loosely based on Forsmark fracture characteristics provided by SKB. Although it is generally accepted that there is a positive correlation between a fracture's size and its transmissivity/aperture, the functional form of that relationship remains a matter of debate. Relationships that assume perfect correlation, semi-correlation, and non-correlation between the two have been proposed. To study the impact that adopting one of these relationships has on transport properties, we generate multiple sparse fracture networks composed of circular fractures whose radii follow a truncated power law distribution. We observe that adopting a correlation between a fracture size and its transmissivity leads to earlier breakthrough times and higher effective permeability when compared to networks where no correlation is used. While fracture network geometry plays the principal role in determining where transport occurs within the network, the relationship between size and transmissivity controls the flow speed. These observations indicate DFN modelers should be aware that breakthrough times and effective permeabilities can be strongly influenced by such a relationship in addition to fracture and network statistics.

In the second section of Chapter 1, we present an analysis and visualization prototype using the concept of a flow topology graph (FTG) for characterization of flow in constrained networks, with a focus on DFN. Our method allows users to understand and evaluate flow and transport in DFN simulations by computing statistical distributions, segment paths of interest, and cluster particles based on their paths. The new approach enables to evaluate the accuracy of the simulations, visualize features of interest, and compare multiple realizations over a specific domain of interest. It allows to simulate complex transport phenomena modeling large sites for networks consisting of several thousand fractures without compromising the geometry of the network. However, few tools exist for performing higher-level analysis and visualization of simulated DFN data. The prototype system we present addresses this need. We demonstrate its effectiveness for increasingly complex examples of DFNs, covering two distinct use

cases – hydrocarbon extraction from unconventional resources and transport of dissolved contaminant from a spent nuclear fuel repository.

The third section of Chapter 1 is based on LANL contribution to Task 9 "Increasing the realism on solute transport modeling of LTDE and REPRO experiments" which are both long term diffusion test in granitic crystalline rock. In frame of Task 9A, modeling of REPRO experiment, only the first stage was performed. A high quality mesh was generated for simulation of diffusion processes of pulse injected tracer through boreholes. Afterward, the LANL team focused on Task 9B, where LTDE experimental results did not follow those predicted by conventional diffusion modeling. Using DFN model we tried to verify the hypothesis, that injected tracer rather moves through micro fractures, which exist in the rock sample, than move by pure diffusion through rock matrix. Our simulation results show that micro fractures can play an important role in solute movement, however, the transport process observed in the experiment is not fully understood.

Generally speaking, the results of the Grimsel Test Site (GTS) colloid-facilitated radionuclide transport tests indicate that the actinides Th, Pu and Am, and the fission product ^{137}Cs, are the most likely radionuclides to experience colloid-facilitated transport over long time and distance scales (at least for bentonite colloids in a fractured crystalline setting). However, the time and distance scales of the GTS tests were very short relative to time and distance scales of relevance for nuclear waste repository performance assessments, so it should not necessarily be concluded that colloid-facilitated transport of these radionuclides will be a concern in such performance assessments. The GTS results collectively suggest that colloid-facilitated radionuclide transport is likely to be more efficient at lower radionuclide concentrations than at higher concentrations because a greater fraction of the radionuclide mass will then tend to become associated with strong, low abundance adsorption sites on the colloids. Stated differently, the GTS results suggest that colloid-facilitated transport over very long time and distance scales is much more likely to involve very small concentrations of radionuclides rather than large concentrations.

Future work will include continued development of the DFNWORKS computational suite, including application of the suite to model/interpret data sets from Swedish Task Force. This collaboration will provide an excellent opportunity to build and test additional capabilities in DFNWORKS and also to further examine upscaling behavior in discrete fracture networks that could have a significant impact on repository performance assessments. We will also investigate if reduced order models of discrete fracture networks can be developed using graph and machine learning based methods so that these can be used in performance assessment frameworks of interest to GDSA. Also, evaluations of the circumstances under which it may be appropriate to use a more computationally-efficient heterogeneous porous medium representation of discrete fracture networks (started in FY 2015) will continue with UFDC colleagues. There will be no future formal interactions with participants of the Colloids Formation and Migration project (at the Grimsel Test Site) because DOE participation in that international collaboration has concluded.

1. DEVELOPMENT AND CAPABILITY DEMONSTRATION OF DISCRETE FRACTURE NETWORK MODEL, DFNWORKS

1.1 Introduction

In this document we report recent technical and scientific developments of the Los Alamos National Laboratory computational suite, dfnWorks, for simulating flow and transport in fractured rocks such as the Crystalline rocks that are the focus of this work package. dfnWorks can be used to stochastically generate three-dimensional discrete fracture networks where fracture geometry is retained and flow and transport are simulated therein without using one-dimensional pipe network approximations.

In the first section of this report, we show results of our recent study on fracture size and fracture transmissivity correlation. We characterize how different fracture size-transmissivity relationships influence flow and transport simulations through sparse three-dimensional discrete fracture networks, loosely based on Forsmark fracture characteristics provided by SKB. Although it is generally accepted that there is a positive correlation between a fracture's size and its transmissivity/aperture, the functional form of that relationship remains a matter of debate. Relationships that assume perfect correlation, semi-correlation, and non-correlation between the two have been proposed. To study the impact that adopting one of these relationships has on transport properties, we generate multiple sparse fracture networks composed of circular fractures whose radii follow a truncated power law distribution. The distribution of transmissivities are selected so that the mean transmissivity of the fracture networks are the same and the distributions of aperture and transmissivity in models that include a stochastic term are also the same. We observe that adopting a correlation between a fracture size and its transmissivity leads to earlier breakthrough times and higher effective permeability when compared to networks where no correlation is used. While fracture network geometry plays the principal role in determining where transport occurs within the network, the relationship between size and transmissivity controls the flow speed. These observations indicate DFN modelers should be aware that breakthrough times and effective permeabilities can be strongly influenced by such a relationship in addition to fracture and network statistics.

In the second section we present an analysis and visualization prototype using the concept of a flow topology graph (FTG) for characterization of flow in constrained networks, with a focus on DFN. Our method allows users to understand and evaluate flow and transport in DFN simulations by computing statistical distributions, segment paths of interest, and cluster particles based on their paths. The new approach enables to evaluate the accuracy of the simulations, visualize features of interest, and compare multiple realizations over a specific domain of interest. It allows to simulate complex transport phenomena modeling large sites for networks consisting of several thousand fractures without compromising the geometry of the network. However, few tools exist for performing higher-level analysis and visualization of simulated DFN data. The prototype system we present addresses this need. We demonstrate its effectiveness for increasingly complex examples of DFNs, covering two distinct use cases – hydrocarbon extraction from unconventional resources and transport of dissolved contaminant from a spent nuclear fuel repository.

1.2 Fracture Size and Transmissivity Correlations: Implications for Transport Simulations in Sparse Three-Dimensional Discrete Fracture Networks Following a Truncated Power Law Distribution of Fracture Size

1.2.1 Introduction

Interconnected networks of fractures are the primary pathway for fluid flow and the associated transport of dissolved contaminants through low permeability rocks. These

fracture networks are common in hydrocarbon extraction, aquifer storage and management, geothermal energy extraction, environmental restoration of contaminated fractured rock sites, and the disposal of spent nuclear fuel (Adler et al., 2012; Berkowitz, 2002; Faybishenko, 2005; Karra et al., 2015; National Research Council,1996; Neuman, 2005). However, the limited amount of available information leads to significant uncertainty when trying to determine the influence of fracture properties on flow and transport through the subsurface (Bonnet et al., 2001). Models used to simulate flow and transport through fractured rock address these uncertainties in different ways and each has its own advantages and disadvantages (Molz et al., 2004; National Research Council, 1996; Neuman, 2005). The two main methodologies in use are continuum models, where the rock mass is represented as a porous medium and the hydraulic conductivity is a scale-dependent correlated stochastic field, and discrete fracture network (DFN) models, where the geometry and properties of individual fractures are explicitly represented. Other models that consider the combined effect of fracture and matrix have also been recently developed (Ahmed et al., 2015a, b; Roubinet et al., 2010; Willmann et al., 2013). Although DFN models can typically represent a wider range of transport phenomena than continuum models (Painter and Cvetkovic, 2005; Painter et al., 2002), the inclusion of detailed features introduces additional layers of uncertainty because more parameters have to be calibrated (Neuman, 2005). For example, it is possible to include in-fracture aperture variability into high fidelity DFN simulations (de Dreuzy et al., 2012; Makedonska et al., 2016) but constraining the in-fracture variability requires detailed knowledge of the particular rock formation.

One source of uncertainty in DFN modeling is the relationship between a fracture's size and its transmissivity. A correlation between size and aperture implicitly define a correlation between a fracture size and its transmissivity if one assumes that the aperture controls flow rate through a fracture, e.g., if the cubic law (Witherspoon et al., 1980) or variant there of is used. However, in comparison to studies on fracture length, there are relatively few on aperture distributions. Although it is generally accepted that there is a positive correlation between fracture length and aperture (Bonnet et al., 2001), a functional form of that relationship remains a matter of debate. Proposed relationships between a fracture's length and its aperture include: Lévy stable (Belfield, 1998), lognormal (Charlaix et al., 1987; de Dreuzy et al., 2001; Margolin et al., 1998), and power law (Gudmundsson et al., 2001; Hatton et al., 1994; Patriarche et al., 2007; Vermilye and Scholz, 1995; Walmann et al., 1996). Each of these models exhibit a range of parameter values based on scale and site data. In particular, an extensive range of exponent values in power law relationships, the most widely used relationship, has been reported in the literature, cf. section 6.4.2 in Bonnet et al. (2001). Moreover, any calibrated exponent is likely not universal at all scales (Hatton et al., 1994; Renshaw and Park,1997).

A direct link between fracture size and transmissivity is also difficult to obtain from field observations and proper characterization of this relationship is essential for upscaled flow and transport behavior if a correlation is adopted (Frampton and Cvetkovic, 2010). The influence of adopting a correlation between fracture size and aperture (transmissivity) on effective network permeability was investigated using two-dimensional fracture networks by de Dreuzy et al. (2004) and Baghbanan and Jing (2007), but they did not consider transport processes. de Dreuzy et al. (2004) observed that the effective permeability of the networks was enhanced when a correlation between fracture size and aperture width was included and Baghbanan and Jing (2007) observed that the overall permeability of the DFN was controlled by large fractures that were assigned higher apertures. Joyce et al. (2014) and Follin et al. (2014) performed a site-specific study using three-dimensional networks and calibrated three different size-transmissivity models by matching specific capacities. They found that uncorrelated models had higher mean transmissivity values when compared to correlated models.

We characterize the influence that selecting a particular relationship between fracture size and transmissivity (aperture) has on transport processes in large (kilometer-scale) semi-generic sparse discrete fracture networks. We use the dfnWorks (Hyman et al., 2015a) computational suite to create three-dimensional fracture networks loosely based on the fractured granite at the Forsmark site in Sweden, a potential host for spent nuclear fuel (Svensk Kärnbränslehantering AB, 2011), and resolve flow and transport therein. We select four different relationships and quantify the impact that each of them has on flow and transport observables. The four relationships we consider are: 1) a positively correlated power law, 2) a log-normal distribution around a positively correlated power law, 3) a log-normal distribution around a prescribed mean, and 4) constant (all fractures have the same transmissivity). Each of these models represents various degrees of uncertainty about the relationship between fracture size and transmissivity. Adoption of a positively correlated power law model assumes a fairly low degree of uncertainty, log-normal distribution around a positively correlated power law includes a stochastic term to account for variability of transmissivities in fractures of the same size, and the log-normal distribution around a prescribed mean assumes a high degree of uncertainty asserting that there is no correlation between the fracture size and transmissivity; the constant relationship is used for comparison. Their influence on observables is compared in terms of the effective permeability of the network, transport properties of a conservative solute passing through DFN, and where transport occurs in the network.

We observe that networks with a correlated relationship have consistently higher effective permeability values and earlier breakthrough times than networks without correlation. Specifically, fracture network geometry plays a principal role in determining where transport occurs within the network and the adopted relationship between fracture size and transmissivity controls the speed of flow and transport times. The results suggest the breakthrough times and effective permeabilities are influenced by the adopted relationship in addition to fracture and network statistics.

1.2.2 Methods

In the DFN approach, geologic field investigations are used to create a network of fractures where the geometry and properties of individual fractures are explicitly represented as $N-1$ dimensional objects in an N dimensional space, e.g., lines in two dimensions or planar polygons in three dimensions. Fractures in the network are assigned a shape, location, and orientation based on distributions obtained in a site characterization. Once a network is constructed, the individual fractures are meshed for computation and the flow equations are numerically integrated on the resulting computational mesh. In most DFN methodologies, the matrix is considered impervious due to its low permeability (Trimmer et al., 1980). Examples of the various DFN methodologies and their applications are found in Cacas et al. (1990); de Dreuzy et al. (2004, 2012); Dershowitz (2014); Erhel et al. (2009); Hyman et al. (2015b); Ji et al. (2011); Mustapha and Mustapha (2007); Pichot et al. (2010, 2012) and Xu et al. (2006).

1.2.2.1 Transmissivity Models

Under the assumption of aperture uniformity, flow through the fractures is equivalent to flow through two parallel plates, and the volumetric flow rate Q per unit fracture width normal to the direction of flow is given by the Boussinesq equation (Boussinesq, 1868).

$$Q = -b^3 \frac{\rho g}{12\nu} \nabla h \tag{1-1}$$

where b is the fracture aperture, ρ is the fluid density (which we assume is constant), ν is the fluid viscosity, and h it the hydraulic head. This relationship between aperture and flow rate can be used to derive a similar relationship between aperture and transmissivity.

$$T = b^3 \frac{\rho g}{12 v} \tag{1-2}$$

referred to as the cubic law (Witherspoon et al., 1980). For heterogeneous fracture apertures with significant fracture roughness and/or fracture closing, measured values of transmissivity can deviate from predictions obtained using the cubic law (Konzuk and Kueper, 2004; Zimmerman and Bodvarsson, 1996). A host of corrections and reformulations of the cubic law have been proposed. There are reformulations based on other powers of aperture such as the quadratic law $T \propto b^2$ (Uchida, 1994) and the quintic law $T \propto b^5$ (Klimczak et al., 2010). Cvetkovic et al. (2004) and Cvetkovic and Frampton (2012) investigated the influence that adoption of either the cubic law or the quadratic law had on transport properties in three-dimensional DFN. They determined the selection of how aperture relates to transmissivity can influence transport and retention properties. Others have proposed correction factors based on geometric and empirical considerations (Renshaw, 1995; Witherspoon et al., 1980). We only consider the cubic law because it is already established the choice of aperture-transmissivity relationship can influence transport properties. Additionally, using a similar computational setup, Makedonska et al. (2016) found that in-fracture aperture variability has little effect on transport properties in sparse three-dimensional fracture networks. In light of their field each fracture is assigned a uniform aperture representative of the mean value of variable apertures within a fracture plane.

We consider four different size-transmissivity relationships and quantify the impact that their adoption has on flow and transport observables. The four relationships are: 1) a positively correlated power law, 2) a log-normal distribution around a positively correlated power law, 3) a log-normal distribution around a prescribed mean, and 4) constant. The functional forms of the relationships between transmissivity T and radius r are the following. The first model we consider is a positively correlated power law relationship with parameters α and β,

$$\log(T) = \log(\alpha \cdot r^{\beta}) \tag{1-3}$$

We refer to this model as *correlated*.

The second model includes a stochastic term into (5),

$$\log(T) = \log(\alpha \cdot r^{\beta}) + \sigma_T N(0, 1) \tag{1-4}$$

to account for uncertainty and variability between fractures of the same size. The strength of the stochastic term is determined by the variance of a log-normal distribution σ_T and the stochastic term is an independent identically distributed random variable sampled from a normal distribution with mean 0 and variance 1, $N(0, 1)$. This model results in a log-normal distribution of fracture transmissivities around a positively correlated power law mean. We refer to this model as *semi-correlated*.

The third model assumes that there is no correlation between the fracture size and transmissivity and all values are independent identically distributed random variables from a log-normal distribution with specified mean μ_T and variance σ_T,

$$\log(T) = \mu_T + \sigma_T N(0, 1) \tag{1-5}$$

We refer to this model as *uncorrelated*.

The fourth model represents an assumption that in addition to no relationship between r and T, and there is no variation between fractures,

$$\log(T) = \mu_T \tag{1-6}$$

We refer to this model as *constant*. Equation (1-6) provides a control case for comparison between the other models.

Each of these models represents various degrees of uncertainty about the relationship between fracture size and transmissivity. Adoption of the perfectly correlated model (1-3) implicitly assumes a fairly low degree of uncertainty about the relationship between fracture size and transmissivity. While there are indications that such a relationship between size and transmissivity is useful (Dershowitz et al., 2003), the deterministic formulation is an idealization where all fractures of the same size are assigned the same transmissivity. Such a model disregards all mechanical, chemical, and hydrological processes that can result in variation between transmissivity of fractures of the same size. However, the formulation is convenient because each realization of network geometry requires a single realization of the transmissivity field Frampton and Cvetkovic (2010) calibrated the parameters of a perfectly correlated model in a DFN representation of fractured crystalline rock at Laxemar, Sweden using soft conditioning based on Posiva flow logs (PFL). The conditioning is soft in the sense that the objective is to match the distribution of borehole flows with the distribution PFL flows rather than specific data. Other research teams have also used the perfectly correlated model (Bogdanov et al., 2007; de Dreuzy et al., 2002; Joyce et al., 2014; Wellman et al., 2009). The semi-correlated model (1-4) attempts to address the some of the issues associated with its deterministic counterpart. While still not resolving the physical processes that cause variations between the transmissivities of fractures of the same size, it includes a stochastic term to account for these variations (Hartley et al., 2006). While this term might increase realism of the network, it is more cumbersome than the perfectly correlated model, both in terms of computational demands (multiple transmissivity field realizations for the same network geometry are required) and calibration data (the semi-correlated model requires additional support from field data to constrain its additional parameters (Frampton and Cvetkovic, 2010)). The semi-correlated model is the least common of the models considered here, even though some researchers consider it the most realistic (Follin et al., 2014). In the uncorrelated model (1-5), a lognormal distribution around a prescribed mean transmissivity is used to include variability between fractures. Here the mechanical, chemical, and hydrological processes are assumed principally responsible for variations between fracture transmissivities rather than assuming a correlation between a fracture's size and its transmissivity. In other words, this model is the opposite extreme of the perfectly correlated model and the semi-correlated is a combination of the two. Examples of studies that use the uncorrelated DFN models are Cacas et al. (1990); Cvetkovic et al. (2004); de Dreuzy et al. (2001); Dverstorp and Andersson (1989) and Kang et al. (2015).

We begin by comparing all four models on a single DFN realization to explore what differences occur due to assumptions of correlation and the inclusion of stochastic terms. Because there is no randomness in the correlated and constant models, only one transmissivity field is generated for each network for these models. To sample the stochastic term in the semi-correlated and uncorrelated models, thirty independent transmissivity fields are generated on a fracture network geometry for each relationship. The average statistics are studied for each set, as well as those obtained for individual realizations. This results in sixty-two flow solutions for this particular fracture network. Next, we compare the correlated and constant models using thirty independent network realizations to determine what variation exists between realizations of the fracture networks. These two relationships, correlated and constant, are selected because statistics obtained from the semi-correlated

and uncorrelated center around their deterministic counterparts. In sum 112 different flow field on 31 different network geometries are considered.

The adopted parameters of the four different relationships for the single DFN realization are provided in Table 1-1. The parameters are selected so that the mean transmissivity of the fracture networks are all the same and that the distributions of aperture and transmissivity in models that include a stochastic term are also the same. In all cases the P_{32} values are nearly identical; differences between samples are less than 10^{-5}. The parameter values and variances are taken from those provided in Table 6-75 in the SKB report TR-10-52 (Svensk Kärnbränslehantering AB, 2010). Figure 1-1 shows the distributions of fracture apertures and transmissivities for the correlated (blue), semi-correlated (red), and uncorrelated models (green). The values are normalized by the aperture of the constant model for comparison. Figure 1-1 (a) shows the distribution of apertures for the correlated, semi- correlated, and uncorrelated models. Even though the mean values of aperture are all the same, there is a clear difference between the distributions of the deterministic model (correlated) and the two stochastic models (semi-correlated and uncorrelated) due to the stochastic term. In the correlated case, the apertures (and transmissivities) are determined by the power law distribution for the fracture radius, which has a hard cutoff. This lower bound results in distributions with a sharp cutoff in the distribution of apertures as well, reminiscent of a power law distribution. The stochastic term in the semi-correlated and uncorrelated models results in wider distributions with heavier tails. Figure 1-1 (b) shows the distribution of transmissivities for the correlated, semi-correlated, and uncorrelated models. The distributions of the two stochastic models different from the correlated model, but are nearly indistinguishable from one another. The distribution of transmissivities for the stochastic models have a much fatter tail at high values of transmissivity, include more small transmissivity values, and have a higher variance than the deterministic model.

Table 1-1. DFN generation parameters. The values are loosely based on fractured granite at the Forsmark repository site in Sweden (Svensk Kärnbränslehantering AB, 2010). The domain is a cube with sides of length (L) 1000 [m]. Parameters of the Fisher distribution for fracture orientation, Eq. 1: Mean Trend (θ^1), Mean Plunge (φ^1), and the concentration parameter (κ). Parameters for the power law distribution of fracture radii, power law exponent (α), upper cutoff (r_u/L) [-], and lower cutoff (r_0/L) [-]. The required number of fractures from each increased to reach the percolation threshold. Mean P_{32} (surface area of the fractures over the total volume) value for the fracture network that connects the inflow and outflow boundaries of this DFN is 0.057 m^{-1}.

Set	**Fisher Distribution**			**Power Law Distribution**			**Fracture Density**
	θ^1	φ^1	κ	γ	r_u/L [-]	r_0/L [-]	Number of fractures
1. (NS)	90.0°	0.0°	21.7	2.5	560	15	2093
						20	1019
						25	583
2. (NE)	135.0°	0.0°	21.5	2.7	560	15	2000
						20	919
						25	503
3. (HZ)	360.0°	90.0°	8.2	2.38	560	15	7711
						20	3887
						25	2285

Table 1-2. Four different relationships between fracture radius r and transmissivity T. Parameters are selected so that all models have the same mean and the two stochastic relationships have similar distributions.

Model	**Relationship**	**Parameters**
Correlated	$\log(T) = \log(\alpha \cdot r^{\beta})$	$(\alpha, \beta) = (1.3 \cdot 10^{-9}, 0.5)$
Semi-Correlated	$\log(T) = \log(\alpha \cdot r^{\beta}) + \sigma_T N(0,1)$	$(\alpha, \beta, \sigma_T) = (1.3 \cdot 10^{-9}, 0.5, 0.7)$
Uncorrelated	$\log(T) = \mu_T + \sigma_T N(0,1)$	$(\mu_T, \sigma_T) = (-18.79, 0.8)$
Constant	$\log(T) = \mu_T$	$\mu_T = -18.79$

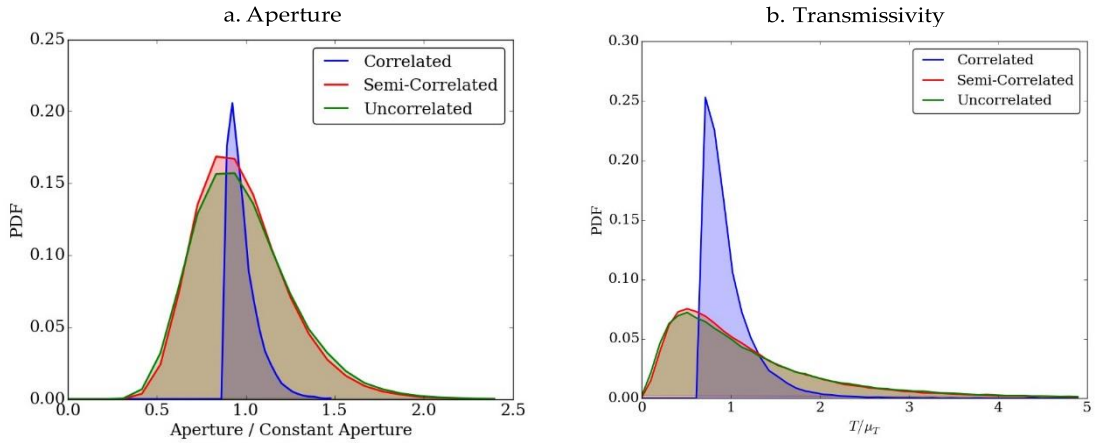

Figure 1-1. Empirical probability density functions of the (a) fracture apertures and (b) transmissivities for the correlated (blue), semi-correlated (red), and uncorrelated models (green). Model parameters, provided in Table 1-2, are selected so that the mean transmissivity of the fracture networks are all the same and that the distributions of aperture and transmissivity in models that include a stochastic term are similar. Values are normalized by the value of the constant model for comparison. (a) Even though the mean values of aperture are all the same, there is a clear difference between the distributions of the deterministic model (correlated) and the two stochastic models (semi-correlated and uncorrelated) due to the stochastic term. The stochastic term in the semi-correlated and uncorrelated models results in wider distributions with heavier tails that do not exhibit a sharp cutoff in the distribution, which occurs in the correlated case due to the truncated power law distribution of fracture radii. (b) The distributions of transmissivity for the two stochastic models different from the correlated model, but are close to one another. The distribution of transmissivities for the stochastic models display a much fatter tail at high values of transmissivity, include more small transmissivity fractures, and have a higher variance than the deterministic model.

1.2.3 Results

In this section we report how the adopted relationships between fracture size and transmissivity influence flow and transport behavior in terms of the effective permeability of the network, particle breakthrough times and transport resistance curves, and network backbone. We begin with a single DFN realization to

focus our discussion and presentation of results and then report observations for multiple fracture networks.

1.2.3.1 Effective Permeably

To estimate the effective permeability of each network in the direction of flow, we compute the Darcy velocity at the outlet plane and then invert Darcy's law using the imposed pressure gradient and domain size. Values of mean, variance, minimum and maximum for the samples are reported in Table 1-3. For comparison, effective permeability values are normalized by the effective permeability of the constant fracture network. Figure 1-2 shows a scatter plot of the semi-correlated and uncorrelated values along with a black dotted line of the effective permeability of the constant fracture network and a blue dotted line for the effective permeability of the perfectly correlated network.

Table 1-3. Effective permeabilities. Values are normalized by the effective permeability of the constant fracture network for comparison.

Model	Mean	Variance	Minimum	Maximum
Correlated	2.56	-	-	-
Semi-Correlated	2.62	0.13	3.35	2.03
Uncorrelated	0.98	0.04	1.46	0.66

The effective permeabilities of the networks are within a factor of two to three of one another. The perfectly correlated model resulted in a value of effective permeability two and one-half times that of the constant network even though the mean values of transmissivity in the two networks are the same. The reported value of the semi-correlated model center around that of the perfectly correlated value, which is expected because the semi-correlated relationship is based on the perfected correlation relationship, and the uncorrelated networks' effective permeabilities center around that of the constant network, which is expected because the uncorrelated relationship is based on the constant relationship. There is more variation between realizations using the semi-correlated relationship when compared to the uncorrelated relationship.

The observed difference between effective permeability values of the correlated/semi-correlated and constant/uncorrelated models demonstrates that correlation between fracture size and transmissivity influence the effective permeability of a DFN. Considering that the mean values of the fracture based transmissivities are the same and the distributions of the two stochastic models are nearly identical, cf. Fig. 1-1 (b), it appears that correlations between fracture size and transmissivity impact upscaled transport properties in a manner that cannot be known *a priori* when considering only the distributions of aperture and transmissivity. In other words, fracture network geometry also plays a key role in determining upscaled flow properties. *de Dreuzy et al*. (2004) observed similar results in two-dimension DFN simulations, but the impact on transport, which we consider in the next section, was not investigated.

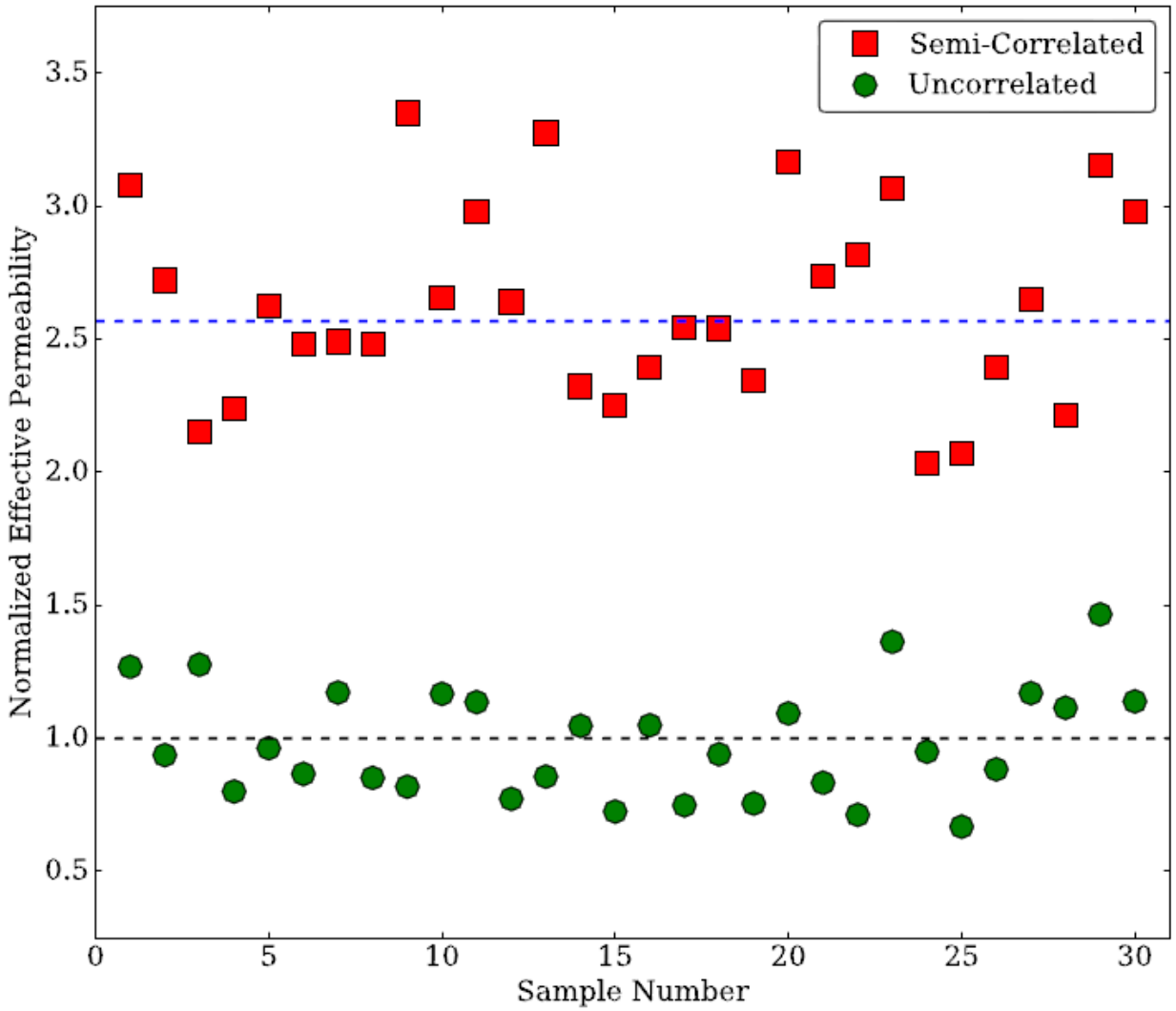

Figure 1-2. Effective permeability of the fracture networks. Values are normalized by the effective permeability of the constant fracture network for comparison (black dotted line). The effective permeability for the perfectly correlated model (blue dotted line) is 2.56 times that of the constant fracture network. Values for the uncorrelated model center around the value of the constant model. Values for the semi-correlated model are higher than the constant and center around the value of the correlated model and exhibit more variation than the uncorrelated model.

1.2.3.2 Travel Time and Transport Resistance Distributions

Figure 1-3 (a) reports the empirical cumulative distribution function (CDF) for the particle travel times (breakthrough curves). Figure 1-3 (b) reports the compliment of the cumulative distribution function (CCDF) on a log-log plot. Semi-translucent lines represent individual realizations and thick lines are the aggregate of all realizations for a given relationship. DFN with semi-correlated relationships are red, uncorrelated: green, correlated: blue, and constant: black. For comparison, time (ordinate) is rescaled by the 50% breakthrough of particles in the constant fracture network.

Breakthrough times for the correlated and semi-correlated networks are significantly earlier than those observed for constant and uncorrelated networks. Table 1-4 reports the 50% breakthrough times and exponent of a power law field to CCDF tail. The earliest breakthroughs are observed in semi-correlated networks and the latest breakthrough times are observed in the uncorrelated model. The aggregate values of the semi-correlated networks are very close to the correlated values, similarly for the uncorrelated and constant networks. This is not surprising however, because the semi-correlated relationship is based on the correlated and the uncorrelated relationship is based on the constant model. However, at early times the stochastic models have slightly earlier breakthroughs than their deterministic counterparts. This deviation is more pronounced in the uncorrelated/constant case. There are particular realizations of the semi-correlated model where the 50% breakthrough is later than particular realizations of the uncorrelated model. While it is already known that the effect of transmissivity variability on the DFN scale can be significant, these distributions provide evidence that the effect it is increased when transmissivity is correlated with fracture size. The exponent of the power laws fit to the tail of the distributions are all approximately the same ≈ 2. These observations suggest that a correlated relationship between fracture size and transmissivity leads to earlier breakthrough time but the scaling of the distribution at later times is not significantly influenced.

Considering each fracture network as a homogenous permeability field with an effective permeability k_e, a straightforward calculation using Darcy's law shows that increase of effective permeability by a factor of 2.5, as reported in Table 1-3 for the correlated cases, results in a decrease of travel time by 60%, i.e., breakthrough in the higher permeability fields is 0.4 times the breakthrough in the lower permeability field. This analytical value is quite close to the observed values that are reported in Table 1-4 where the median breakthrough of particles in the perfectly correlated network is 0.34 times the breakthrough of that observed in the constant network. This similarity is not surprising because both the effective permeability and breakthrough curves are upscaled observables of the networks. However, the reported value is slightly smaller than what is expected analytically indicating that particles in the correlated networks move faster than what would be expected in an equivalent continuum representation.

Table 1-4. 50% breakthrough times and exponent of power law fit for particle travel time and retention parameter. Times are normalized by the 50% breakthrough time for the constant network.

Model		Correlated	Semi-Correlated	Uncorrelated	Constant
τ	50% Breakthrough	0.34	0.31	1.01	1.00
	power law Exponent	1.95	1.90	2.00	2.18
β	50% Breakthrough	0.27	0.24	1.02	1.00
	power law Exponent	1.87	1.84	1.96	2.18

In general, the CDF and CCDF of β are rather similar to those of τ and thus are not shown. There are a few differences worth commenting on however. The mean values of the semi-correlated networks is rather close to that of the correlated network, similarly for the constant and uncorrelated networks, but less so than for values of τ. Deviations of the stochastic models are more pronounced in the CDF of β than of τ. Distributions of β are more sensitive to changes in aperture than τ, because b is used in the computation of β. Therefore variations in aperture along the pathlines are more reflected in plots of β than of τ, which likely leads to these deviations. At early times, the models that include a stochastic component have slightly

earlier breakthroughs than their deterministic counterparts. All tails exhibit roughly the same power law scaling suggesting that the adopted fracture-size transmissivity relationship influences the early retention times more than long-term transport behavior in the DFN. Table 1-4 reports the 50% breakthrough times and exponent of a power law fit to CCDF tail, which are nearly identical to those reported for τ.

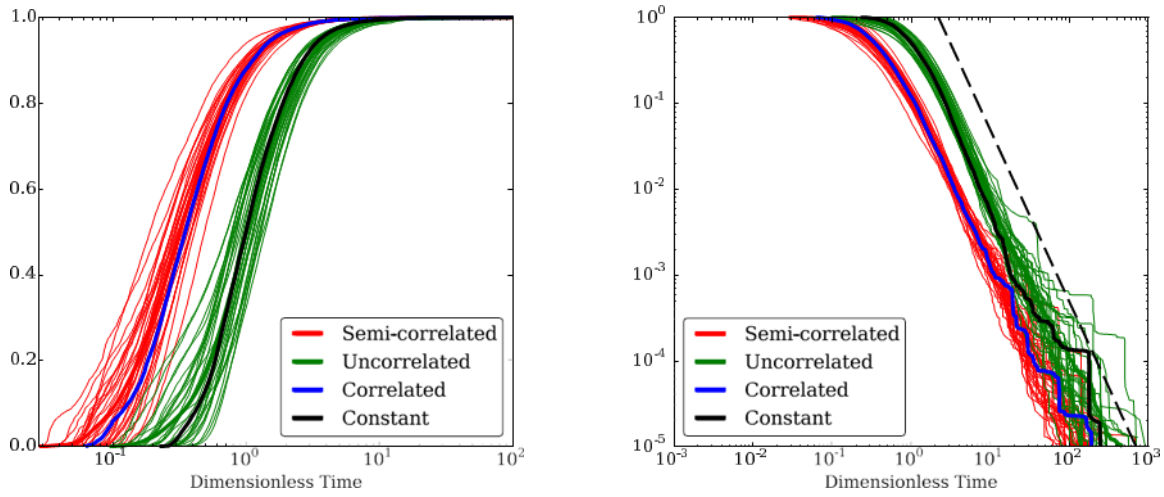

Figure 1-3. Breakthrough times (τ). Semi-correlated relationships between fracture size and transmissivity are red, uncorrelated: green, correlated: blue, and constant: black. For comparison, time on the ordinate is rescaled by the 50% breakthrough of the constant fracture network. (a) Cumulative distribution of travel times. Breakthrough times for the correlated and semi-correlated networks are much earlier than that observed for constant and uncorrelated. The earliest breakthroughs are observed in semi-correlated networks, and the latest breakthrough times are observed in the uncorrelated model. The aggregate values of the semi-correlated networks are very close to the correlated values, similarly for the uncorrelated and constant networks. (b) Compliment of cumulative distribution of travel times. All tails exhibit the similar exponents of power law scaling (Table 1-4) suggesting that the adopted relationship does not influence long-term transport behavior in the DFN. The dashed black line is a power law with an exponent of two.

1.2.3.3 Active Specific Surface Area

Although the distributions of τ and β are quite similar, their relationship with one another varies with the adopted size-transmissivity model. Figure 1-4 shows scatter plots of β as a function of τ for the (a) perfectly correlated model, (b) the semi-correlated model, and (c) the uncorrelated model. Values of τ and β are normalized by the median value of the constant model for comparison. The constant model is not included because $\beta = 2\,\tau\,/b$, as b is constant. A linear model fits the data well; R2 greater than 0.9 for all size-transmissivity relationships. The specific surface area associated with each model is approximated by taking the median value of $\beta\,/\,\tau$ across all particles. Relative to the active surface area of the constant model, the active surface area of perfectly correlated model is 0.82 (variance of 0.003), 0.84 (variance of 0.02) for the semi-correlated, and 1.04 (variance of 0.02) for the uncorrelated models. In other words, the active surface area in the two correlated models is around 15-20% lower than the uncorrelated models. Such values indicate that size-transmissivity relationship could influence transport mechanisms like diffusion, retention and fracture-matrix exchanges because the active surface area available for these processes depends on the adopted model.

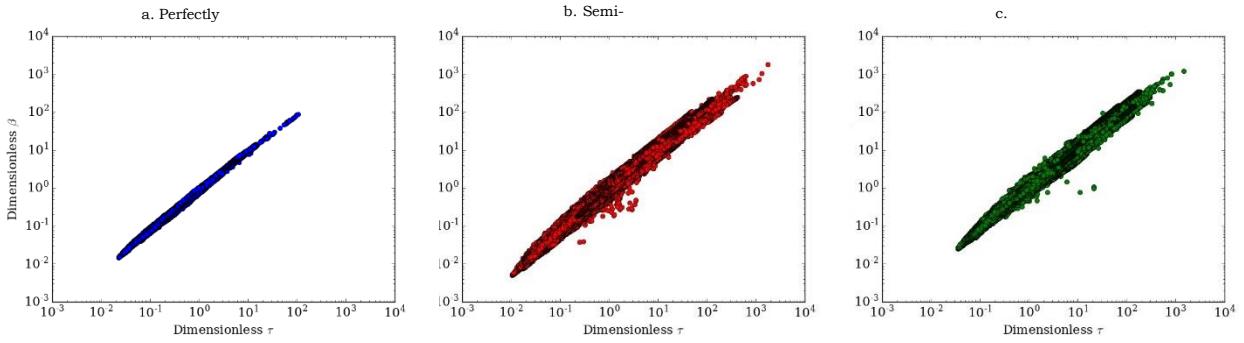

Figure 1-4. Scatter plots of β as a function of τ for the (a) perfectly correlated model, (b) the semi-correlated model, and the uncorrelated model (c). Values of τ and β are normalized by the median values from the constant model for comparison. Best linear fits to the scatter plots provide an estimate of the active specific surface area associated with each model.

1.2.3.4 Multiple Geometry Realizations

We generate thirty additional fracture networks using the same statistics (Table 1-1) and compare breakthrough curves assuming either a correlated or constant fracture size-transmissivity relationship. This results in an additional sixty flow solutions. These two relationships, correlated and constant, are selected because breakthrough curves of the semi-correlated and uncorrelated center around these values respectively, cf. Fig. 1-3. Therefore general differences in overall flow and transport for the stochastic models in these DFN can be inferred by their deterministic counterparts.

Figure 1-5 (a) shows the CDF for the ten DFN realizations and (b) shows the CCDF. One hundred thousand particles are tracked through each DFN for both the constant and correlated cases. Time is normalized by the fifty percent breakthrough time of the aggregate constant breakthrough times. Semi-transparent lines are single realizations and thick lines are the aggregate of all realizations. Differences between realizations are more pronounced in the correlated networks. Similar to what is observed in Fig. 1-3, these plots indicate that including correlations between size and transmissivity results in significantly earlier breakthroughs than if correlations are not included. The aggregate 50% breakthrough time of the trajectories through correlated networks is about 50% faster than through the constant networks. The standard error for the 50% breakthrough time for the constant networks is 0.018 and 0.013 for the perfectly correlated indicating that the observed differences in 50% breakthrough times are not a result of an insufficient number of realizations. The CCDF for these curves is shown in Figure 1-5 (b) and demonstrates that these differences persist at later times. The dashed black line is a power law with exponent of two and shows that both relationships exhibit similar power law scaling suggesting that scaling of the distribution at later times is not significantly influenced by the adopted relationship. These plots demonstrate that the large discrepancies in travel times resulting from the adopted size and transmissivity relationships do not depend on the particular realization.

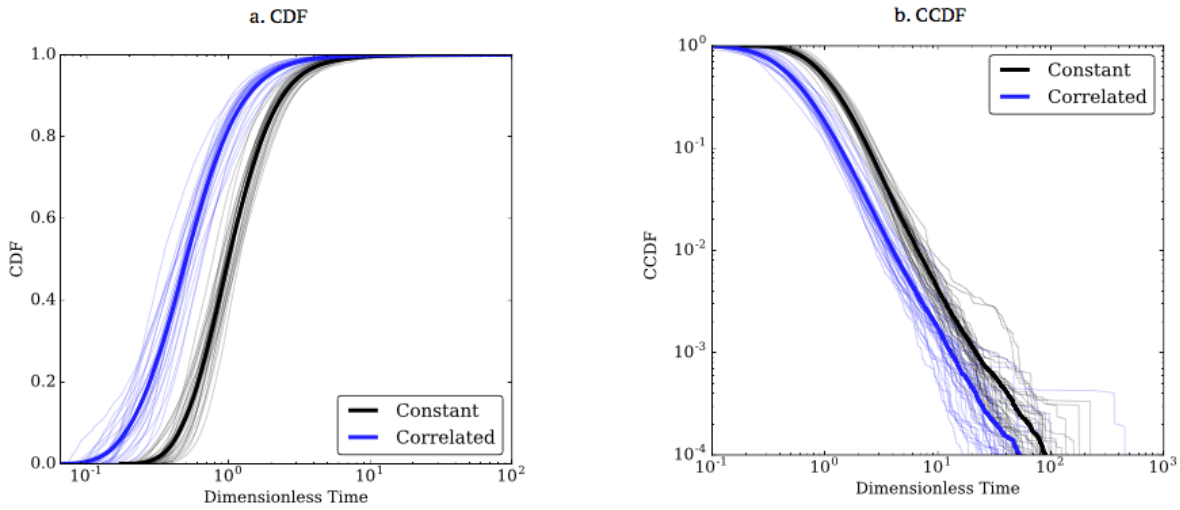

Figure 1-5. Breakthrough time distributions for thirty independent DFN realizations. Time is normalized by the fifty percent breakthrough of the aggregate constant breakthrough times. Semi-transparent lines are single realizations and thick lines are the aggregate of all realizations. For the same fracture network geometry, correlating transmissivity with size results in earlier breakthrough times when compared to simulations where no correlation is adopted.

1.2.4 Discussion

We have characterized the influence that selecting a particular relationship between fracture size and aperture has on flow and transport processes in a large-scale sparsely fractured three-dimensional networks. We compared four different fracture size-transmissivity relationships to investigate the potential impact that each model has on flow and transport. Comparisons are made in terms of the network effective permeability, transport properties including travel time, retention, active surface area, and fracture network backbone structure.

The principal observation of this study is that adopting a correlation between fracture size and transmissivity in a three-dimensional DFN can result in significantly earlier breakthrough times and higher effective permeabilities than if a correlation is not included. We also found that fracture network geometry has a stronger influence in determining where transport occurs within a sparsely fractured DFN network than the adopted relationship between fracture size and transmissivity, which controls the speed of flow and transport. The following list summarizes our key observations:

1. Even though the mean values of the fracture transmissivities are the same for all models and the distribution of transmissivities of the two stochastic models are nearly identical (Fig. 1-1) the perfectly correlated and semi-correlated relationships resulted in consistently higher effective permeability values than the constant and uncorrelated relationships (Fig. 1-2 and Table 1-3). These results suggest that correlations between fracture size and transmissivity influence upscaled transport properties in a manner that cannot be predicted by solely considering distributions of aperture and transmissivity due to the constraints put on the flow field by the fracture network geometry.

2. Breakthrough times for the correlated and semi-correlated networks are consistently and significantly earlier than those observed in the constant and uncorrelated models (Fig. 1-

3, Table 1-4). These observations suggest that flow moves faster through the entire network when larger fractures are assigned higher values of transmissivity.

3. The distribution of particle travels times in the correlated and semi-correlated networks are very close, as are the constant and uncorrelated networks (Fig. 1-3 (a) and Table 1-4). This is not surprising however, because the semi-correlated relationship is based on the correlated and the uncorrelated relationship is based on the constant model. Models that include a stochastic component, semi-correlated and uncorrelated, have earlier breakthroughs than their deterministic counterparts.

4. The tails of the travel time and retention parameter distributions exhibit the same power law scaling behavior, with exponents that are close to 2 (Fig. 1-3 (b) and Table 1-4). This similarity suggests that the adopted fracture-size transmissivity relationship does not have a pronounced influence on long-term transport scaling behavior.

5. The active surface area, computed using τ and β, for the two correlated models is between 15 to 20% lower than the uncorrelated models. These differences could have significant impact on reactive transport modeling because the active specific surface area indicates the amount of surface area available for a dissolved solute.

6. Flow channeling occurs in all of the fracture networks. If correlations between fracture size and transmissivity are included, then it is more pronounced.

7. Fractures that make up the primary backbones of the networks are similar regardless of the adopted relationship between fracture size and transmissivity. Fracture network backbones are comprised of relatively large fractures that are primarily aligned with the direction of flow. These results indicate that the fractures where the majority of transport through the network occurs are primarily determined by the network geometry and the adopted relationship between fracture size and transmissivity is a secondary effect with respect to determining where flow occurs.

1.2.5 Conclusions

A possible explanation for the deviation between the models in terms of flow and transport observables is that the majority of flow and transport occurs in big fractures due to geometrical induced channeling. In the case of the perfectly correlated and semi-correlated models this channeling is further encouraged by the reduced resistance offered by the higher transmissivity values associated with these large fractures. This flow channeling results in higher effective permeability values and faster breakthrough times for these two relationships. Another possibility is that including a correlation between fracture size and aperture influences the overall fracture volumes, which could partially account for the observed differences. In the case of the correlated relationships, the total volume of the fracture network is higher than the uncorrelated, averaging $1.5 \cdot 10^{-4}$ [m^3/m^3] compared to $1.2 \cdot 10^{-4}$ [m^3/m^3]. Recall that the mean transmissivity and P_{32} values were constant between realizations, but not total fracture volume. This difference can thus explain some of the differences between the breakthrough curves. It is more likely that the increased volume of the large fractures, resulting in higher transmissivity in the principal flow regions, is more responsible for the differences, than the overall increase in volume fraction.

Within any DFN simulation several assumptions and conceptualizations have to be invoked. For this study, we assumed that: fracture aperture is constant within each fracture, transmissivity is controlled by the cube of the aperture, a relatively low variability of transmissivity is considered, particles are inserted according to flux weighting, the network is sparse, fractures are circles, fracture radii follow a truncated power law distribution with hard upper and lower cutoffs, and fracture centers are uniformly distributed. Some of these assumptions, such as uniform fracture aperture; network sparsity; and the adoption of the

cubic law, could influence the magnitude of the observed differences due to adoption of a particular size-aperture relationship. For example, it is possible that discrepancies between size-transmissivity models might be exacerbated/reduced if different aperture-transmissivity relationships are considered. The adoption of the cubic law has been shown to influence the computation of τ and β (Cvetkovic et al., 2004; Cvetkovic and Frampton, 2012) and combining our results with those of Cvetkovic and Frampton (2012), who found that adopting the cubic law can lead to early breakthrough up to 4 times faster than those obtained using the quadratic law, it could be possible that the same fracture network geometry could produce mean breakthrough times that are an order of magnitude different from one another, e.g., a perfectly correlated model using the cubic law compared to a uncorrelated model using the quadratic law. Whether these assumptions combine in a linear or non-linear fashion is an open area of research. A better understanding of both the hydraulic relationship between aperture and transmissivity and size-transmissivity relationships and their joint sensitivity is imperative for robust modeling using discrete fracture networks. Similarly, although Makedonska et al. (2016) found that in-fracture variability had little effect on global transport properties in similar networks it is possible that different internal aperture structures representative of various physical processes such as channelization of apertures due to erosion, could have more significant impacts when combined with a correlation relationships between size and aperture. Furthermore, our problem setup was designed so that distributions of transmissivity were identical, albeit with low variance. While the similarity between the constant and uncorrelated networks under such setup is not terribly remarkable, it is remarkable that a single fracture network geometry with identical transmissivity distributions (Fig. 1-1) but different size-transmissivity correlation relationships can produce differences of mean breakthrough times that can be up to half an order of magnitude different. While it is already known that the effect of transmissivity variability on the DFN scale can be significant, this study provides evidence that the effect is increased when transmissivity is correlated with fracture size.

Regardless of the assumptions made here, the observed differences between transport properties serves as a warning for DFN modelers. If fracture network statistics are such that geometrically induced flow channeling through a few large fractures parallel to the primary direction of flow are common, then the differences resulting from the use of different fracture-size transmissivity relationships will likely be more pronounced than networks where fractures sizes are relatively uniform. Thus the DFN modeler should take care to not only consider the distribution of transmissivities in the network, but also the distributions of fracture size, transmissivity, and orientation relative to the flow domain if they want different size-transmissivity relationships to result in similar flow behaviors. In the absence of good estimates of aperture (T) distributions, then using flow measurements is the only viable option to calibrate DFN parameters. Another project comparing these models using data from the Laxemar site, similar to the study of Frampton and Cvetkovic (2010), could help shed light on the variations induced by adoption of one these models. However, calibration of model parameters by matching specific capacities and flow has resulted in higher values of mean transmissivity for uncorrelated models when compared to correlated models (Joyce et al., 2014; Follin et al., 2014). The calibrated values resulted in a significant difference of mean log transmissivities between models. In light of the findings reported here, the higher values likely compensate for the increased flow channeling encouraged by the correlated relationships by globally increasing the transmissivity of the entire model to match flow parameters. While this modification might decrease the difference between model outputs in terms of effective permeability and breakthrough curves, the absence of a physical reason for these higher permeabilities warrants further consideration. If there are aperture distributions to match against flow as well, an analysis similar to that presented here could be used to determine which correlation model is most plausible for a given site. Explicitly, when trying to honor aperture (T) distributions, it may not be possible to also match observed flow properties, which would identify poor quality models.

The prevalence of flow channeling indicates that there is a large percentage of these sparse networks which is fairly stagnant, and that percentage is increased when a correlation between size and transmissivity is included in the model setup. The transport of solutes in these stagnant regions could

result in increased matrix diffusion, retention and fracture-matrix exchanges due to the additional amount of time that solutes would remain there. Therefore it is not unreasonable to expect that reaction of a solute with the fracture walls would be highly variability throughout the network and that variability would depend on the assumed correlation between size and transmissivity. Through the use of particle tracking methods and the analysis tools used here it should be possible to identify these flow channeling pathways, as well as their compliment, to potentially investigate their field relevance and perhaps identify them a priori for a given hydraulic setup. The approximation of active surface area was a first step in this direction and we are currently designing additional studies to investigate such properties.

1.3 Analysis and Visualization of Discrete Fracture Networks Using a Flow Topology Graph

1.3.1 Introduction

We present a method for the analysis and visualization of constrained flow networks driven by applications in computational simulation of fluid flow and transport in fractured rock. Determining how subsurface fractures control flow and transport has various applications in engineering and scientific endeavors including hydrocarbon extraction, aquifer storage and management, geothermal energy extraction, environmental restoration of fractured rock contaminated sites and the disposal of spent nuclear fuel (Middleton et al., 2015; National Research Council, 1996; Neuman, 2005). Figure 1-7 shows a caricature of flow and transport in fractured porous media.

Discrete fracture networks (DFN) are one methodology that computational subsurface scientists use to simulate fluid transport within such fracture networks. Although DFN models were introduced over two decades ago, they are fairly novel to the visualization community. The need for this collaboration between the visualization researchers and geoscientists is the result of recent developments in the DFN community where three-dimensional fracture networks consisting of tens of thousands of fractures are now common. Accumulating local and global transport statistics such as the distribution of traversal times, velocities, and tortuosity of advected particles is not terribly difficult, but the analysis of these flow features and determining their relation to properties of the simulation domain is a demanding task. The large amount of data resulting from these physics based simulations has created a need for advanced analysis and visualizations techniques to more efficiently process and interpret model outputs. Our team has addressed this need by developing, implementing, and testing a new visualization workflow.

We identified three areas of analysis research needed by geoscientists concerned with flow and transport in fractured media: statistical analysis, topological path analysis, and topological trace clustering. Figure 1-6 shows an outline of the methodology we developed, which is described in this paper, to address these needs. Using particle trajectories in the DFN (Left) we build a flow topology graph (FTG) (Center Top) that embeds information about transport through the fracture network into a graph. This representation enables us to develop and use graph analytics based algorithms, which combine feature and statistical analysis, to analyze the simulation output. The analysis results are stored in the FTG and are used to generate geometry files and statistical plots which can be explored by the user (Right). Using this information, we evaluate and refine the FTG analysis to investigate specific features of flow and transport through each DFN (Center Bottom). Embedding analysis from the FTG directly into geometry files for the DFN allows for integration of the FTG data with standard visualization tools. Furthermore, these tools allow for the identification of backbones in the DFN, which are connected subsets of fractures on which a majority of flow and transport occurs.

The key contributions of this methodology development are:

- Advanced visualization for the analysis of fluid transport in DFN simulations.
- The direct transformation of the simulation results to a flow topology graph (FTG) with one-to-one correspondence with DFN geometry.

- A novel graph analysis algorithm for detecting back- bone paths on FTG.
- A new algorithm for clustering particle trajectories based their path topology that can be used to identify and quantify flow channeling within the DFN.

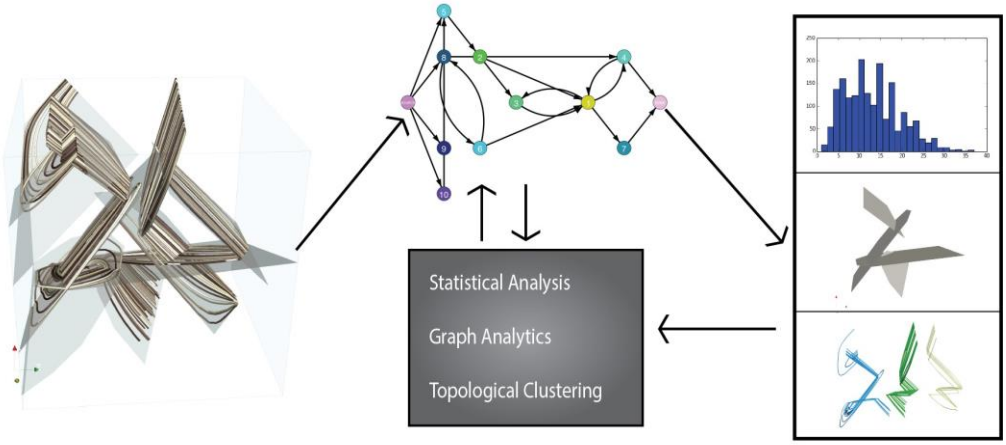

Figure 1-6. Overview of our analysis and visualization methodology. (Left) Transport through a discrete fracture network (DFN) is simulated using particle advection through a steady-state flow field. (Center Top). Pathlines obtained in the transport simulation are used to construct a flow topology graph (FTG) that embeds flow and transport information into a graph. (Right) Analysis of the FTG using statistics, graph theory, and topological clustering provides detailed information about various features of interest. Using this information, we can evaluate and refine the FTG analysis to investigate specific features of flow and transport through each DFN (Center Bottom).

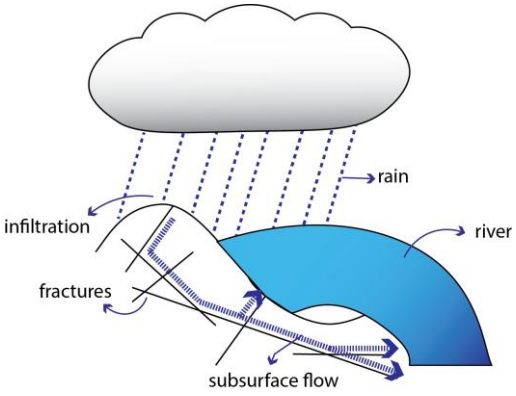

Figure 1-7. A caricature of a two-dimensional fracture network embedded within impermeable rock. Fractures are the principal pathway for flow and transport through low-permeability rocks in the subsurface. Beyond the difficulties associated with determining flow and transport within such networks, efficient and effective ways for the analysis of the data sets produced via such simulations are still lacking. Existing general data analysis and visualization methods must be specialized for the needs of particle tracking through fracture network data.

1.3.2 Analysis and Visualization of DFN

Using the FTG representation, we provide a workflow that produces three types of analysis products for DFN, namely statistical analysis, path analysis, and topological clustering. Statistical analysis can be

used for debugging and to compare multiple fracture networks based on the same geological distributions to address questions of ergodicity and resolve global and local trends in the flow field. Path analysis allows us to use a Lagrangian viewpoint to find features in the flow field and link them to the fracture geometry. One key feature of interest within a DFN are backbones, which are connected subsets of fractures on which a majority of flow and transport occur. Backbones are believed to be responsible for flow channelization in fractured media, where flow is concentrated in certain regions of fractured rock, and have been qualitatively identified (Hyman et al., 2015b; de Dreuzy et al., 2002). In this section, we provided a systematic methodology to identify them using the FTG. We describe a method of topological clustering to group particles which take similar paths through the network. This clustering allows us to better visualize and segment particle traces as well as verify backbones defined using path analysis.

1.3.2.1 Statistical Analysis

The construction of each DFN is stochastic, relying on randomly sampling known distributions of fracture size, orientation, aperture and shape; multiple realizations of a given site must therefore be created. Statistical analysis can be used to verify that an ensemble of fracture networks with different topologies, but modeling the same formation of rock, produce similar results. Sampling constraints in both time and space limit what experiment data can be obtained in the field; local measurements of key phenomena are not possible throughout a site. Therefore, upscaled quantities, are used for verification of flow and transport simulations at site specific locations. Statistical analysis can also be used to compare transport behavior on selected sets of fractures or paths (such as backbones) to global transport for the system.

By appending fracture and intersection attributes as well as statistics to the FTG for a transport simulation, we can readily accumulate global statistics for a single DFN, a local subset of the DFN, or multiple realizations. While global statistics are important for comparison between transport simulations, localized statistics taken from a subset of the network are useful for characterizing specific flow attributes. For example, the user can segment the parts of the network that are never reached by particles, find the set of fractures responsible for the fastest or slowest transport times, or segment the DFN into topological layers by finding all fractures where particles must travel through at least N fractures before entering.

Several attributes are stored in the FTG that are of interest to the domain experts analyzing the transport simulations of a DFN. Per-fracture attributes include the size; topological distances (E^i, S^i); the number of transported particles ($|P^i|$); and mean fracture tortuosity ($\bar{T}^i$). For each particle, we store both per-fracture and total transport time, path length, velocity, and particle tortuosity (T_j). For these integral values, we are also interested in how they change as particles traverse the network. To accomplish this investigation, we parameterize the derived values for each particle over time, trace-path length, and topological distance. For example, in Figure 1-9 the tortuosity is shown for all particles in a simulation that uses the DFN shown in Figure 1-8. In the top plot of Figure 1-9, the maximum path length for all particle trajectories is calculated L_{max}, and then divided evenly by the number of sample points. We parameterize each trajectory and sample the tortuosity starting at these points along the curve, discarding trajectories that have a shorter overall path length than the sample point. The result is a two-dimensional histogram, which we display as a heat map, in shades of blue. In addition, the mean tortuosity curve is plotted in green, and the number of particles sampled at that point (the occupancy) is plotted in magenta. When plotting the results we add a negative value to the distances that indicates the path length to the exit, as opposed to from the source. We can interpret from these plots that the farther a particle travels through the DFN, the more direct its path towards the exit becomes. In the bottom plot, the change in fracture tortuosity over topological distance to the exit, E^i, is shown. This parameterization is necessarily much coarser, and the number of fractures at each distance is given for reference. From this graph we show that fractures closer to the DFN exit, provide a more direct path.

Most often the statistical data is displayed by producing plots and graphs, however we also allow the user to directly visualize these distributions on the original geometry. For large DFN, rendering the entire network using a colormap to identify attributes is less useful, due to occlusion. However, this method of visualization is still relevant when applied to meaningful subsets of the DFN.

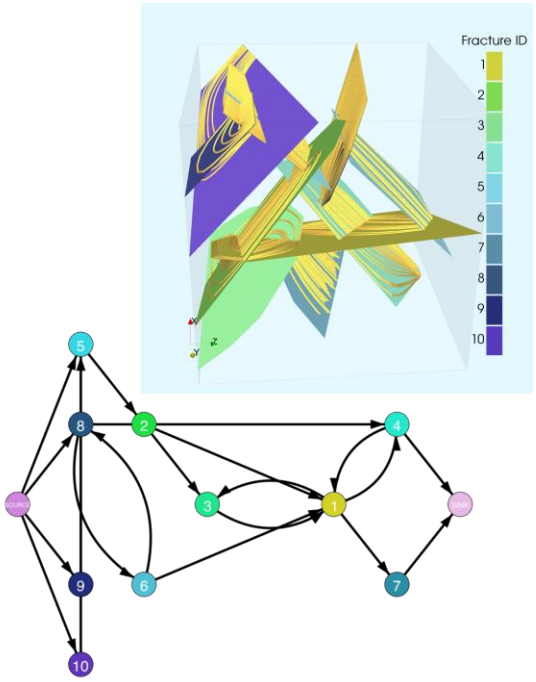

Figure 1-8. The flow topology graph (FTG) derived from the transport simulation. In the FTG each fracture polygon is represented by a vertex in the graph. Each edge represents particles that travel between two fractures over an intersection. We also add a "SOURCE" and "SINK" node (at the far left and right respectively) to the FTG from which all particles enter and exit.

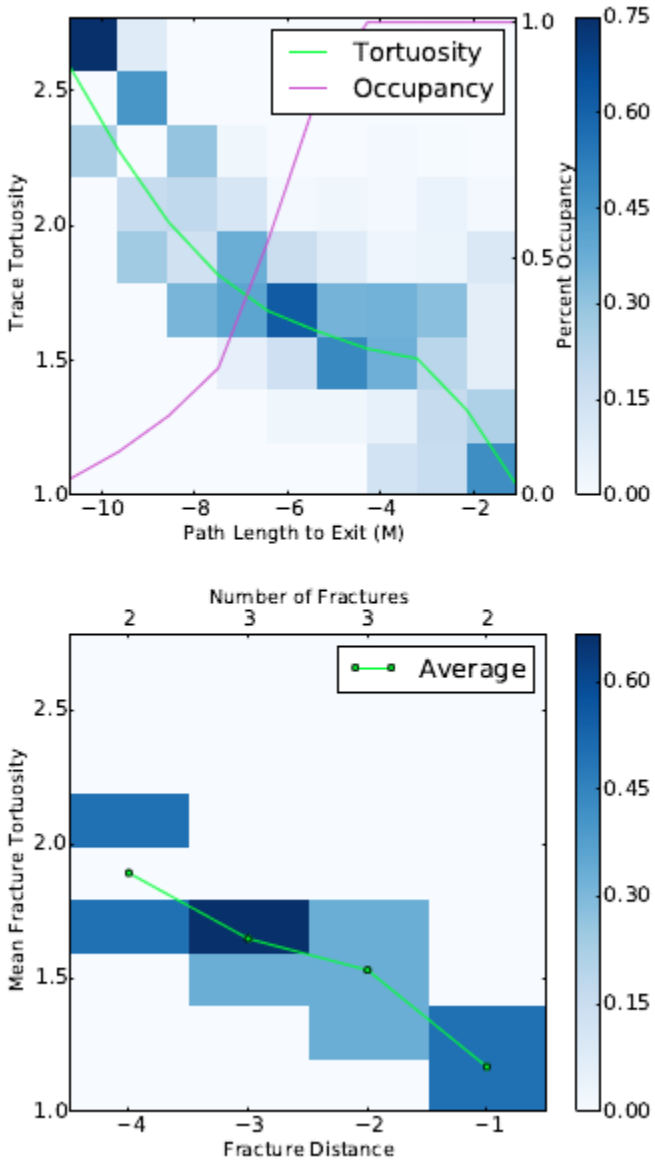

Figure 1-9. Plots of statistical qualities from a transport simulation in a DFN made up of ten fractures. Around 150 particles are advected through the DFN to produce these statistics. (Top) A blue heat map represents the two-dimensional histogram of tortuosity values sampled at discrete path lengths along particle traces (blue gradient), as well as the mean curve (green). The particle occupancy, or number of particles in the system at each sampled point is also shown in magenta. The coarseness of the plot is due to the simplistic nature of our example. (Bottom) Particle tortuosity distribution are sampled over topological distance indicating that as particles reach fractures closer to the exit, they take more direct, less tortuous, paths.

1.3.2.2 Topological Trace Clustering

Visually differentiating large numbers of integrated paths leads to an occlusion problem. A common approach to resolve this issue is to compare traces using a similarity metric and then apply a clustering algorithm to associate them with groups in accordance with their similarity. Once split into

groups, particle traces can be visualized either through rendering each group in a different color, by rendering a smaller but representative subset of the particles, or a combination of both techniques. This allows users to better understand the coherency between particle traces and observe trends in the flow field or network. Previous research has focused on defining similarity metrics by properties of the curves themselves, such as curvature (McLoughlin et al., 2013), shape (Yu et al., 2012), or statistical distributions (Lu et al., 2013). However, similarity in shape or structure of individual trajectories is less important for our application.

We define a similarity function using network topology in terms of the ordered set of fractures each trace traverses. By representing the trace path of a particle using the ordered set of fractures that it visits while traversing a DFN, and comparing the paths each trace takes through the FTG the similarity of traces can be readily computed. Explicitly, any two traces that travel on the same ordered set of fractures are considered topologically equivalent when clustering. Similarly, if two particles have nearly the same trace path, deviating only slightly in the fractures they traverse, then they will be considered to have small distance value between them. Finally, if two particles have completely different trace paths then they will be assigned a very large or infinite distance.

This trace distance function is inspired by the Levenshtein distance function for string-based comparisons (Levenshtein, 1966). The Levenshtein distance function finds the shortest edit distance between two strings by recursively comparing the ordered set of characters in the string and produces the minimum number of changes needed to convert one string into the other. The possible changes include insertion, removal or replacement of single characters. For example, when comparing 'skip' and 'sip' or 'show' and 'slow', the Levenshtein distance is one in both cases (a removal and a replacement, respectively). Wilson et al. (2004) used an adaptation of this metric to compare spectral representations of graphs. We have adapted this algorithm by considering strings of fracture IDs, F_i, representing the trace paths of particles, rather than strings of characters. For example, a particle could have the trace path, $\{F_1, F_3, F_{10}\}$, which would indicate that it entered the DFN on fracture F_1, was transported to fracture F_3 and exited the DFN through fracture F_{10}. A pseudocode implementation of the distance function is given in Algorithm 1.

The major difference between our algorithm and the original is the use of a topological cost function for making edits; $\phi(i,j)$ in Algorithm 1. In the Levenshtein distance, all edits are given a cost of 1, while we calculate the cost of replacing fractures in a trace path using the topological distance information encapsulated by the FTG. We define the cost function for replacing a fracture, F_i with another fracture F_j, $\phi(i,j)$, to be the number of edges in the shortest path from vertex v_i to v_j in the associated FTG. In other words, the replacement cost is represented by the minimum number of fractures that would be traversed for a particle on F_i to reach F_j. If no path exists in the FTG, then $\phi(i,j)$ = infinity. This definition also implies that the cost of insertion or deletion of a fracture is 1. This can be explained as follows: if there existed two trace paths, $R_a = \{F_a, F_b, F_c\}$ and $R_b = \{F_a, F_c\}$, then the FTG would have to contain edges $e_{a;b}$, $e_{a;c}$. Therefore the cost to either remove F_b from R_a or add it to R_b is 1, as that is the minimum distance between the associated vertices. The resulting algorithm uses a recursive function that returns the minimum cost.

Algorithm 1 Trace Distance Function

Let R_a be the ordered set of fracture ids, F_i, for trace a
Let $|R_a|$ be the number of fracture ids in R_a
Let $R_a|_k$ be the k_{th} fracture id
Let ϕ F_i, F_j be the cost function for replacing IDs s.t.

```
ϕ Fi, Fj ≡ the shortest path from vi to vj in the FTG
Initially La ← |Ra|
Initially Lb ← |Rb|
procedure TDF(Ra,La,Rb,Lb)
    if La = 0 then
        return Lb
    end if
    if Lb = 0 then
        return La
    end if
    if Ra|La = Rb|Lb then
        RC ← 0
    else
        RC ← min(ϕ(Ra|La,Rb|Lb), ϕ(Rb|Lb,Ra|La) )
    end if
    return MIN(
    TDF(Ra,La − 1,Rb,Lb) +1,
    TDF(Ra,La,Rb,Lb − 1) +1,
    TDF(Ra,La − 1,Rb,Lb − 1) +RC
    )
end procedure
```

To identify trace clusters given their mutual distances, we use the agglomerative hierarchical clustering (AHC) algorithm (Defays, 1977). This is one of the most commonly used method for clustering path traces and other integral curves (Salzbrunn et al., 2008; Pobitzer et al., 2011; McLoughlin et al., 2013; Yu et al., 2012; Lu et al., 2013). AHC builds a hierarchy by recursively merging pairs of clusters (initially each trace being its own cluster), until all clusters are merged. The resulting hierarchy can then be 'cut' by setting a maximum distance value for pairs of particle traces included in the same cluster. This gives the user control to define how similar the paths of particles must be. In practice we choose several distances and allow the user to select the most appropriate one during exploratory visualization.

In Figure 1-10(a) we show the results of our clustering algorithm for the ten-fracture system 2. Here, each cluster is rendered in a unique color. In Figure 1-10(b) we show only the two largest clusters to emphasize the paths taken by traces in each group. In particular the largest (yellow) cluster consists of particles that take similar, but not the same, path through the network. We note that the largest clusters lie primarily along the *backbone* path shown in Figure 1-10. By grouping and then visualizing large clusters of particles that take similar paths through the network, users are better able to observe and differentiate areas where channelization occurs. If a larger number of clusters is seen, then a single representative trace of each cluster will be rendered to further reduce occlusion retaining key information. The representative trace is chosen at random from particles which take the most common path in the cluster.

While our algorithm on its own performs well and produces clusters as expected, we have included two optional modifications to accommodate specific needs of DFN simulations. First, we allow users to disregard cycles in the fracture path by collapsing them in the trace path i.e.,

$\{\ldots, F_a, F_b, F_c, F_d, F_b, F_e, \ldots\} \rightarrow \{\ldots, F_a, F_b, F_e, \ldots\}$. In the context of a DFN, this corresponds to a particle that leaves a fracture, but later then returns to it and continues to travel therein.

The second modification accounts for potential bias due to initial conditions. To do so, we disregard the first several (typically 1 to 3) fractures in the trace path when computing clusters. Disregarding the first

fractures in a trace path limits the influence that the initial seeding has on clusters by allowing particles to initially disperse/coalesce in the system prior to being subject to analysis. Hyman et al. (2015b) observed that is took particles uniformly distributed across an inlet plane 250 meters before they exhibited strong flow channeling characteristics. Trimming initial fractures is an optional step in the clustering algorithm and only useful for certain use cases and under certain initial conditions. However, it provides flexibility for domain experts.

By visualizing the large clusters of particles, channelization becomes more apparent. This is an important tool for validating the candidate backbones and observing the global behavior of the flow network.

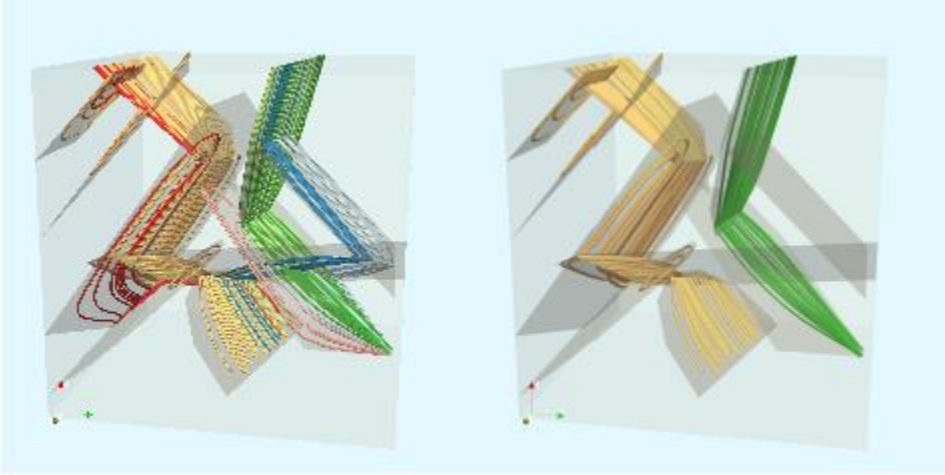

Figure 1-10. We use agglomerative hierarchal clustering to segment particles which take similar topological paths through the network. For this DFN the clustering is readily apparent, and each cluster is rendered with a unique color. In (b) we show the largest two clusters emphasizing that clustered particles take similar paths while traversing the DFN.

1.3.2.3 Analysis Driven Visualization

Exploratory visualization of the analysis results produced by our framework plays an integral role in evaluating the results of a DFN simulation. We have chosen to decouple visualization from the analysis process to maintain both flexibility and interactivity. Statistical plots are produced directly from the FTG using python scripts that generate plots either for the entire system, a subset of fractures representing candidate backbones, or sets of clustered particles. These plots can be combined and overlaid for comparison purposes. This is especially useful for comparing multiple simulated data sets. While we provide predefined python- based scripts to produce these plots, custom plots can also be created. Direct geometric visualization is handled through embedding analysis results directly into geometry files for both the DFN and particle traces. The one-to-one mapping between the FTG and DFN allows us to add per-fracture attributes to the DFN geometry files. Similarly, the statistical and clustering information for each particle is added as an attribute to the trace geometry files. To allow users to explore the results of parameter value changes, we sample a selected parameter space and embed all of the results into the output files. For example, when generating clusters we select multiple minimum distances to cut the agglomerative clustering hierarchy and allow users to select from clusters generated at each level. The number of cuts and minimum distance are user-defined options. By default the mean distance between particles is used as a base. Five subsequent cuts are also made by linearly sampling between the mean distance and one-tenth that distance. The candidate

backbones are embedded in two different ways, to aid users in identifying the most meaningful ones. Paths can be selected by the method and order that they are extracted or by the amount of flow occurring on each. The former allows users to better understand why the algorithm produced each candidate path and the latter gives a more natural ordering of the candidates. Individual traces and each fracture on a selected path retain their statistical properties along with cluster information. This allows each feature to be compared visually and the selections can be used to generate plots for the subset.

The decision to decouple visualization from analysis, rather than integrating both steps into a custom tool, makes possible the use of many standard visualization tools, such as the Paraview data analysis and visualization platform (Ahrens et al., 2005) . Our target user group, computational geoscientists studying flow in DFN simulations, preferred to leverage preexisting tools that they are already familiar with. By using well-maintained visualization tools, we ensure easy use and that the analysis tools can remain usable without support for a new software interface. Furthermore, by encapsulating the analysis methods in an offline process, large amounts of data can be processed. As the field continues to develop, DFNs are expected to become larger, more complex and are likely to require and increasing number of realizations to capture properties of the stochastic system.

We have a minimal set of requirements for visualization tools to effectively visualize the analysis files produced by our system. The first, and most important, is the ability to select subsets of data by setting thresholds for embedded attributes. This enables users to select particle traces by the cluster they belong to or the size of the cluster, and the particular cut in the hierarchy that the clusters are produced from. Thresholding also allows users to select candidate backbones by the method used and order in which they are extracted, or by the amount of flow occurring on each path. The second requirement is to overlay multiple geometry files using the absolute positions of vertices. Finally, the tool must allow users to apply colormaps to the geometry which corresponds to embedded per-cell attributes. Other features that we use to generate the examples provided in this paper, though not necessarily required for analysis, include: rendering lines as tubes of varying thickness and assigning glyphs to represent points and vectors.

1.3.3 Examples

We demonstrate our methodology by analyzing the flow and transport in DFN simulations at various scales. We begin with a medium sized DFN made up of two hundred fractures. Then we demonstrate our approach in two sub- surface applications with networks made up of thousands of fractures. The first of these is used to study unconventional hydrocarbon extraction based on a shale formation in the Tuscaloosa, Alabama. The second DFN model is loosely based on a subset of fractures in Forsmark, Sweden (a potential host location for spent civilian nuclear fuel). We selected these two site characterizations because they highlight different transport scenarios. The primary direction of flow in the hydrocarbon extraction model is radial, towards a horizontal well at the center of the domain, while in the DFN based on the Forsmark site, the imposed pressure gradient drives flow in one primary direction aligned with the Z-axis. We also use the method to compare multiple DFN realizations based on the same statistical distributions.

1.3.3.1 Two Hundred Fracture network

We created a medium sized DFN of two hundred circular and rectangular fractures constrained to a 12 meter cubed domain. This network is used to demonstrate how the combination of statistical and visualization analysis allows us to characterize transport behavior for DFN. A pressure gradient is applied along the X-direction to create flow through the network and about 500 particles are used to simulate fluid transport.

Figure 1-11 shows three backbones identified in the network along with particle trajectories. Backbones are large fractures aligned with principal direction of flow. The backbone along the bottom of the domain, colored purple, is primarily a single large fracture while the other two are composed of

several fractures. On the left, each path is represented by a different color and the clustered particles traveling along each path are represented by tubes whose colors indicate their cluster ID. On the right, fractures are colored by the mean tortuosity of particles on those fractures. The tortuosity values are close to one, indicating that particles traveling on these paths take a direct path towards the exit rather than dispersing into the rest of the network.

Figure 1-12 shows various particle based observables. Figure 1-12 (a) shows a scatter plot of particle density as a function of relation to the fracture area and reveals that a large percentage of transport in the network occurs on a single large fracture. Fracture radii are determined by sampling a power law distribution so there are a lot of small fractures and few large ones. There are a disproportionate number of particles on the largest fracture(s) when compared to the number of large fractures. Figure 1-12 (b) shows particle tortuosity and occupancy as a function of particle length from the exit plane, sampled at discrete points along particle traces. Most particles travel between 15 and 25 meters as they traverse the network; recall that minimum distance to traverse the cube is 12 meters. The tortuosity values indicate that most particles take a relatively direct path through the network. This is further emphasized by the graph in Figure 1-12 (c), which relates fracture tortuosity and the topological distance of each fracture from the exit. The graph also shows that the majority of particles travel along seven fractures or less and that after each transition to a new fracture their path becomes more direct towards the exit.

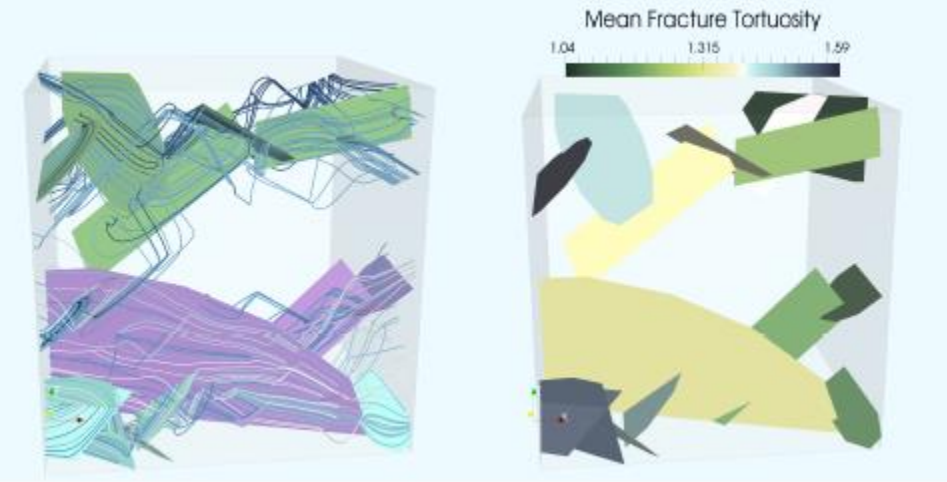

Figure 1-11. Three backbones in a 200 fracture network. On the left, each path is represented by a different color and the clustered particles traveling along each path are represented by tubes whose colors indicate their cluster ID. On the right, backbone fractures are colored by the mean tortuosity of the particles traversing these fractures (fracture tortuosity). The tortuosity values are close to one indicating that particles on the backbones take direct paths towards the exit, rather than dispersing throughout the network.

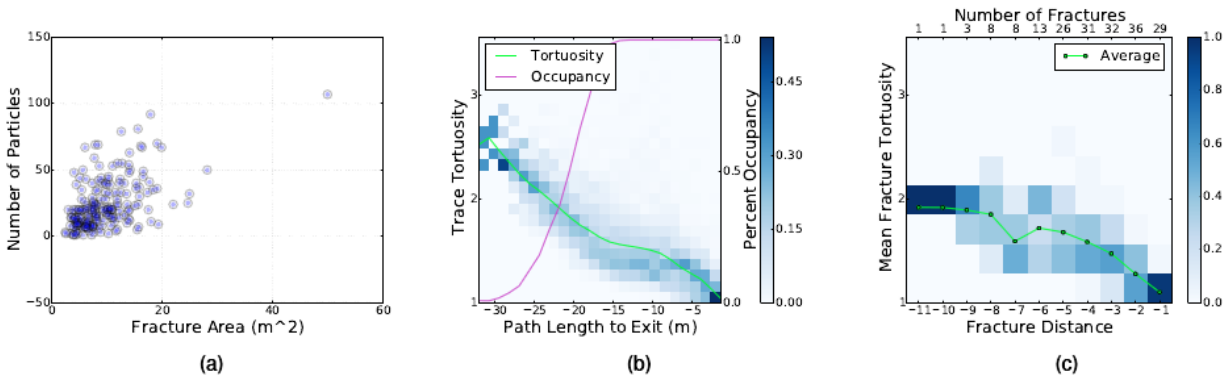

Figure 1-12. We produce statistical results based on the particle behavior in a 200 fracture DFN with around 500 advected particles. The scatter plot in (a) shows the number of particles that traverse through fractures of different sizes. This image indicate that particles are well distributed over fractures of different sizes, except for a single outlying fracture that is significantly larger than the rest on which a large portion of the transport occurs. We calculate a series histogram for the tortuosity by sampling particles at regular intervals of time, path length (b), or mean distance and topological distance (c).

1.3.3.2 Kilometer DFN of fractured granite

The Swedish Nuclear Fuel and Waste Management Company (SKB) has undertaken a detailed investigation of the fractured granite at the Forsmark site, Sweden as a potential host formation for a subsurface repository for spent nuclear fuel (SKB, 2011). We adopt a semi-generic subset of the statistical fracture model determined by SKB, details of the site characterization are provided in (SKB, 2011). Our fracture model uses three fracture sets whose radii are determined by a truncated power-law distribution and varying orientations. The largest fractures have a radius of 560 meters and the smallest have a radius of 15 meters. An example network is shown in Figure 1-13 (a). The domain is a cubic kilometer and each realization contains approximately five thousand circular fractures. The fractures colored orange are not visited by a particle during the transport simulation; only 30% of fractures in the domain are touched by a particle during transport simulations. These results indicate that the strong flow channeling is occurring along backbones in the DFN. Figure 1-13 (b) shows the backbones of the network along with the largest particle clusters for verification. The backbones are made up of large fractures and the particle trajectories tend to arrive on a fracture in a backbone and remain then remain along that path.

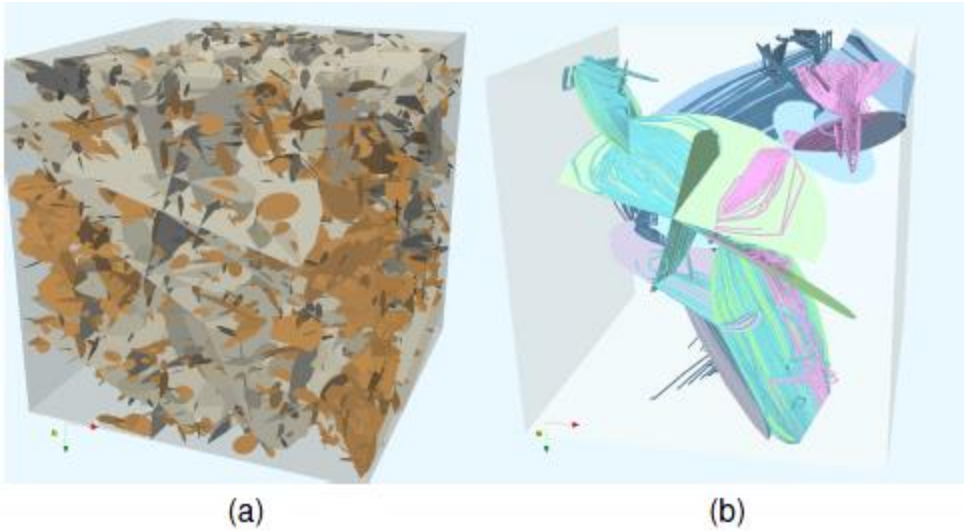

Figure 1-13. (a) A DFN realization based on the fractured granite at the Forsmark site in Sweden. The domain is a cubic kilometer and contains approximately five thousand circular fractures whose radii are sampled from a truncated power-law distribution. The fractures highlighted orange indicate that these fracture have not been visited by any particle during the transport simulation. (b) The backbones of the DFN along with the three largest trace clusters colored by the cluster ID. The backbones are primarily comprised of larger fractures that act as conduits for flow and transport through the network, as shown by the clustering of traces.

1.3.3.3 Network Comparison

DFN are generated stochastically and thus multiple realizations using the same underlaying statistics are required and these multiple DFN are compared to one another. This type of comparative analysis is desirable when trying to demonstrate ergodic behavior in upscaled transport distributions. For example, identifying universal fracture characteristics that lead to flow channeling, which is equivalent to particle clustering, requires numerous realizations. To demonstrate the utility of the proposed methodology in this regard, we compare networks generated using the same underlaying statistics. Comparisons between the networks are performed both visually and analytically to identify features and clusters in the networks.

Three independent DFN realizations based on the Forsmark site are created and the backbone of each network is determined, shown in Figure 1-14 (a-c). In the first and third realization, there is one large fracture that dominates transport through the system. In the second realization, shown in the middle, the backbone is made up of numerous medium sized fractures rather than a single large fracture. The methodology allows us to characterize and identify the key fracture characteristics that lead to flow channeling. One possible use of this methodology is to identify the characteristics of the fractures that make up the backbone and then create reduced DFN models that retain these backbones but omit fractures that do not significantly contribute to transport.

Figure 1-15 shows the particle tortuosity and percent occupancy of particles for the three DFN realizations. Although the backbones are different, particle ensemble statistics appear to have stabilized. Observed tortuosity values all scale linearly with path length to exit and little variability is observed between realizations. However, there are discrepancies in the observed cumulative distributions of percent of occupancy. Most notable, at large distances from the exit plane. One realization has fewer particles with long distances from the exit plane, and this is likely the result of the large fracture that dominants the backbone of DFN, cf. Figure 1-14 (a). In general, we can use such statistical comparisons

to ensure that any given realization of the network topology is equally valid. If there are major discrepancies between networks, we can use the feature analysis and clustering to determine where these differences stem from.

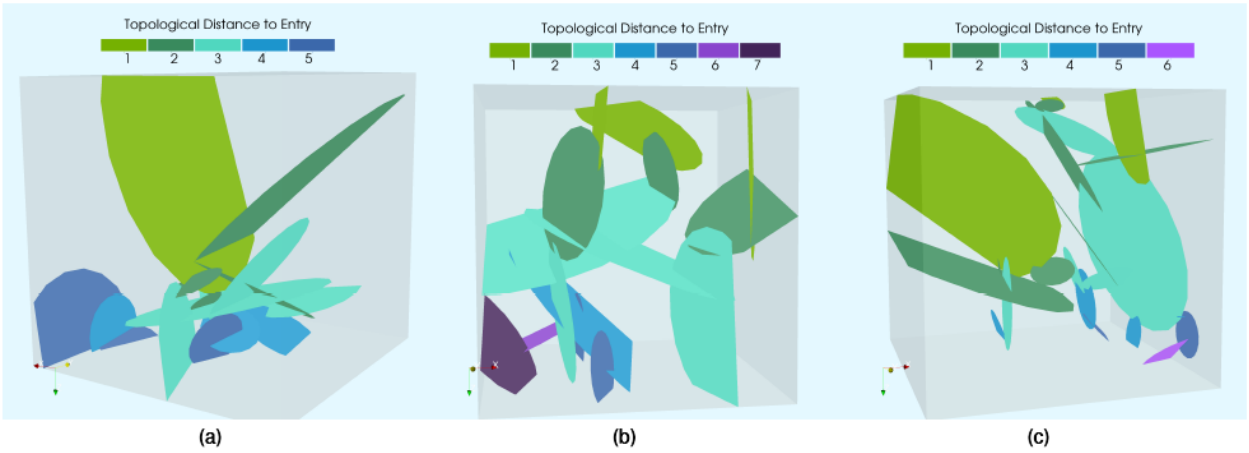

Figure 1-14. The backbones in three realizations of the DFN network topology, all modeling the same physical domain of the Forsmark repository site. Each network has different types of main backbones. This type of comparison, between DFN modeling the same physical site, is important due to the stochastic nature in which DFN are produced.

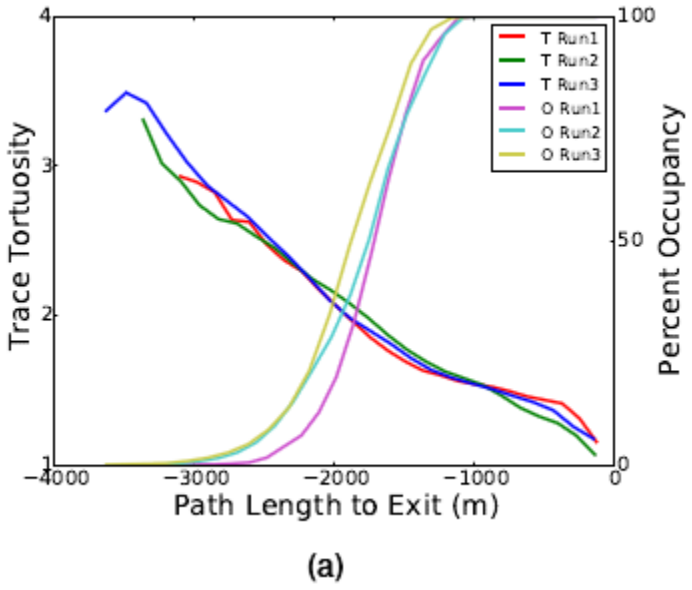

Figure 1-15. Particle tortuosity and percent occupancy of particles for the DFN used in Figure 1-14, which are generated by sampling the same fracture statistics. Similarities and differences in the curves can be explained by the backbone structures developed in each realization.

1.3.4 Conclusions and Future Work

We have introduced a flow topology graph method for the analysis of flow and transport in fractured rock that allows users to analyze simulated flow and transport in discrete fracture networks. Recent advancements in DFN simulation tools have made it possible to model and simulate flow at realistic scales with networks containing thousands of fractures. The methods presented here are part of a prototype system and toolset supporting the interactive, detailed exploration of simulated Lagrangian transport data. The methodology is both modular and flexible, allowing for rapid prototyping and modification of capabilities with changing goals and application needs. Visualization is decoupled from analysis, allowing users to interactively explore the results using tools they are familiar with.

Our FTG-based framework supports both global and localized statistical analysis, feature analysis for discovering channelization due to backbones, and intuitive clustering of particle paths in these large fracture networks. The methodology addresses the three main areas of analysis research identified by geoscientists concerned with flow and transport in fractured media: statistical analysis, topological path analysis, and topological trace clustering. The provided statistical analysis can be used to gain a better understanding of system-wide trends as well as identify potential problems in the simulation. The topological path analysis allows for the identification of important regions within the network, namely backbones, and allows for a systematic, integrative approach to identifying fracture characteristics that lead to flow channeling in fractured rock. The topological trace clustering identifies groups of particles that travel along similar paths and verify backbones. In combination, these tools can be used to identify geological structures that dictate flow and transport in the fractured rock. This characterization can potentially be utilized in the modeling of both static and adaptive control of subsurface processes, being relevant for areas including carbon sequestration, geothermal energy, contamination remediation, and unconventional oil and gas extraction.

While the results demonstrated with our prototype sys- tem are promising, it is important to note that more detailed case studies are needed to evaluate results more conclusively. More research needs to be done concerning the establishment of better metrics for improved path analysis, topological trace clustering, and comparative analysis. We have identified several metrics that produce reasonable results, and we currently allow a user to select what set of metrics to use. More studies are needed to determine which ones are most meaningful for a given DFN application. This aspect is especially relevant when performing comparative analysis, where a proper metric for measuring similarities and differences between multiple realizations of a DFN is crucially important (ensemble simulation and analysis). We do not currently directly visualize the graph as part of our analysis framework. However, developing a scalable algorithm for laying out the graph, especially for quickly comparing between multiple FTG, is the focus of ongoing research. Allowing users to directly interact with the FTG, and highlight features that may be difficult to describe algorithmically is also a future goal. Similarly, directly linking statistical plots with the geometry in a painting and linking style will be considered for future systems. This would require a more customized system, and thus some flexibility in the visualizing tools would be lost, however the benefit may outweigh the cost. Currently our prototype system is used for performing data analysis in a post-processing step. Considering the increasing size and complexity of simulated DFNs, we will consider *in situ* use of our analyses. We have kept this goal in mind during the development of our prototype to minimize the amount of implementation that will need to be done when transitioning our system from a post-processing to an *in situ* analysis system.

1.4 Task 9: Increasing the Realism in Solute Transport Modelling – Modelling the Field Experiments of LTDE-SD and REPRO Using Discrete Fracture Network Modeling

Task 9 focuses on the realistic modelling of coupled matrix diffusion and sorption in heterogeneous crystalline rock matrix at depth. This is done in the context of inverse and predictive modelling of tracer

concentrations of the in-situ experiments performed within LTDE-SD at the Äspö HRL in Sweden, as well as within the REPRO project at ONKALO in Finland, focusing on sorption and diffusion. The ultimate aim is to develop models that in a more realistic way represent retardation in the natural rock matrix at depth.

1.4.1 Task 9A: Long-Term Diffusion Sorption Experiment (REPRO)

Here we focus on REPRO (**R**ock matrix r**E**tention **PRO**perties) experiment, which is presently carried out by Posiva at the ONKALO underground rock characterisation facility in Finland. Today, LANL team has all necessary modelling capabilities to simulate matrix diffusion processes observed during REPRO experiment: computational tool for producing high quality mesh, and control volume HPC flow solver for water phase diffusion and sorption study. In the current section we start from brief explanation of REPRO experiment, giving previously in Task 9 description (Löfgren, 2014), and continue with algorithm of high quality computational mesh generating process.

1.4.1.1 REPRO Experiment

The description of REPRO experiment is given in Löfgren (2014).

A number of boreholes have been drilled into the non-fractured rock matrix from the REPRO niche at ONKALO underground rock characterisation facility, at about 400 m depth (see Figure 1-16). Borehole ONK-PP323 is utilised for the Water Phase Diffusion (WPDE) series of experiments, which are advection-diffusion-sorption experiments. They are carried out between ~18-20 m from tunnel wall. A 1.9 m long section has been packed off, and in this section a dummy has been placed. Its diameter is 54 mm whereas the borehole diameter is 56 mm, leaving a 1 mm gap between the borehole wall and the dummy. This gap is regarded as an artificial fracture of relatively well-defined geometry. In this gap a very low steady state water flow has been applied, directed towards the tunnel. This is achieved by injecting the water at the far end of the packed-off section, as shown to the upper right in Figure 1-16. In this water flow the tracers HTO, Na-22, Cl-36, and I-125 were injected in WPDE-1, and HTO, Na-22, Cl-36, Sr-85 and Ba-133 in WPDE-2. Injection was made as a few hours long pulse at the far end of the experimental section. As the pulse travels with the water flow, its tracers will diffuse into the rock matrix. As the pulse passes, the concentration gradients are reversed and the tracers will diffuse out of the rock matrix and into the flowing water. To date, two experiments have been performed at different flow rates; WPDE-1 (20 μL/min) and WPDE-2 (10 μL/min). The tracer concentrations were measured in water flowing out of the experimental section, both by on-line Na(Tl)I-scintillation detection and by analysing water samples in the laboratory. Breakthrough curves have been obtained over half a year and about one and a half a year for WPDE-1 and WPDE-2, respectively. The rock volume surrounding the experimental section, affected by in-diffusion, is not planned to be overcored.

The Through Diffusion Experiment (TDE) will be carried out between three parallel boreholes situated perpendicular to each other, in 1 m long packed-off sections, at a distance of about 11 to 12 m from the tunnel wall. Borehole ONK-PP326 will be used as the injection hole and boreholes ONK-PP324 and ONK-PP327 as observation holes (see Figure 1-16, upper left corner). The distances between the boreholes are between 10 and 15 cm. Any advective flow between the boreholes is foreseen to be insignificant, as the experiment takes placed in a rock volume that lacks in water-bearing fractures. The tracers HTO, Na-22, Cl-36, Ba-133, and probably Cs-134 are planned to be injected. The decreasing and (foreseen) increasing tracer concentrations in the injection hole and observations holes, respectively, will be analyzed. This is done on extracted samples in the laboratory; by liquid scintillation counting and High Resolution GXRS (gamma measurements). Furthermore, on-line measurements will be performed in the injection hole and observation holes by a High Performance Germanium detector and a Na(Tl)I-scintillation detector, respectively. Tracer concentrations in the injection hole will be measured at a higher frequency at the first part of the experiment, while focus will be shifted towards analyzing breakthrough concentrations in the observation holes as the experiment progresses. Breakthroughs of non-sorbing tracers are foreseen within the timeframe of Task 9, although unexpectedly low pore diffusivities may

prevent this from happening. The tracers were chosen to make overcoring and analysis of tracer penetration profiles possible, although this option is presently not included in the REPRO planning. As the REPRO project is on-going, it offers the possibility of both inverse and predictive modelling. The in-situ part of REPRO aims to tackle the topics of diffusion, sorption, anion exclusion, and rock matrix anisotropy. The laboratory part has, in addition, focused on small scale rock characterisation. This provides a wealth of input data that can be incorporated in the modelling.

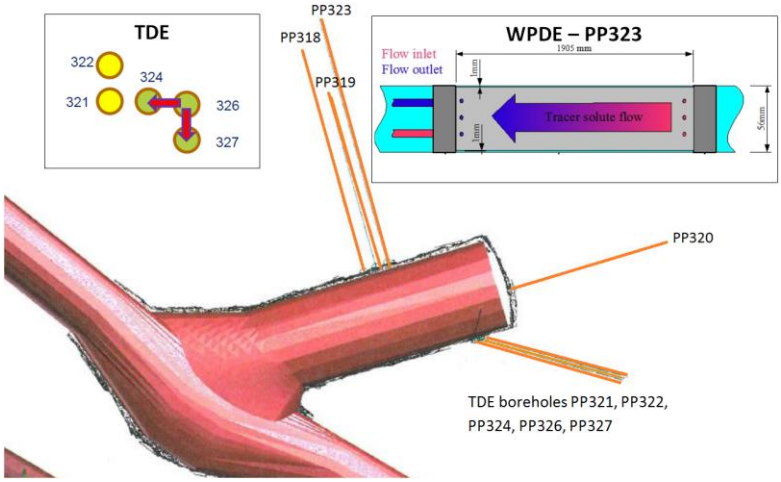

Figure 1-16. The REPRO niche at the 401 m level at ONKALO, and the nine boreholes drilled from the niche. Borehole PP323 is utilized for WPDE-1&2, and boreholes PP324, PP326, and PP327 for TDE.

1.4.1.2 Modeling of REPRO experiment. Phase 1: Producing high quality computational mesh on REPRO model.

In order to simulate water and tracer sorption into rock matrix the high quality computational mesh is required. We use Los Alamos Gridding Tool (LaGriT, 2013), meshing capability developed at LANL, to produce three dimensional computational mesh.

A cube of size 1.9 m x 1.9 m x 1.9 m is generated for WPDE experiment modeling, where only one borehole, drilled into non-fractured rock matrix, is considered (Figure 1-17). First, the structured tetrahedral mesh is produced in the cube. Then, the hole of 56 mm diameter is created on the center of the cube (Figure 1-18, right panel). Producing the cylindrical hole, which represents the borehole in the rock, requires to reform the structural grid to unstructured circular grid around the borehole. The mesh of the borehole is generated separately (Figure 1-18, left panel). The cylinder of 54 mm diameter represents the filled with dummy borehole. The last step is to merge three dimensional unstructured mesh of the cylinder with the cube, generating 1 mm meshed layer between dummy filled borehole and the rock matrix.

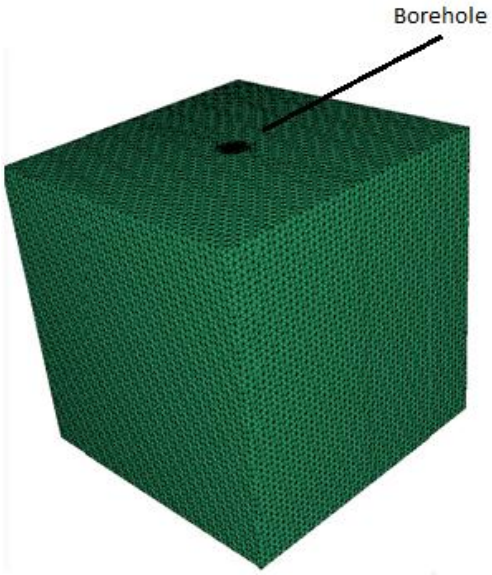

Figure 1-17. The cube with 1.9 m side length is generated with structured tetrahedral mesh. The borehole is modelled in the center of the cube along the z direction.

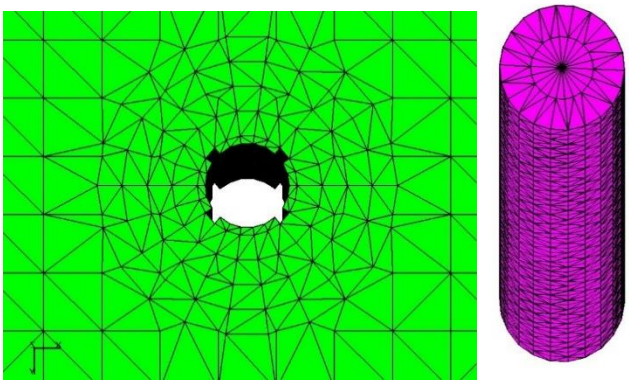

Figure 1-18. The first two steps of computational mesh generation for WPDE experiment modeling. On left side the part of the cube is shown, where the unstructured cylindrical mesh is merged to structural mesh of the cube, and the cut of the cylindrical hole is in the center of the cube. The right panel shows the cylindrical mesh created separately.

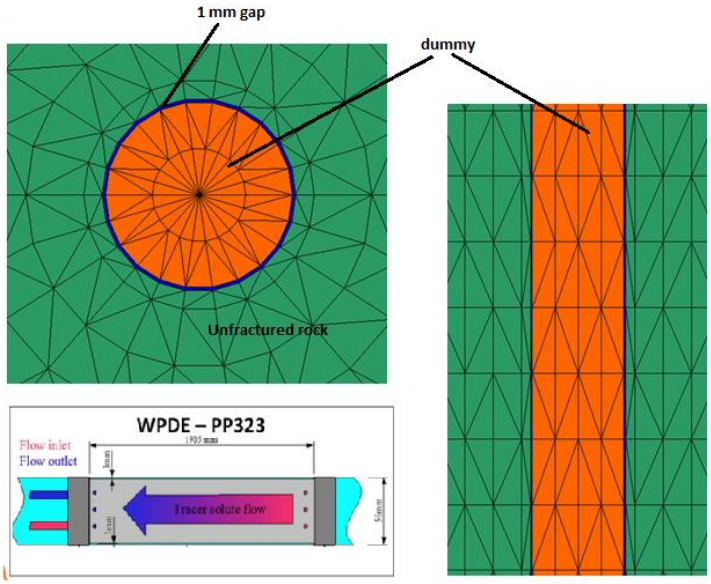

Figure 1-19. The final computational mesh for WPDE experiment modeling.

The final mesh for WPDE modeling is shown in Figure 1-19. The right upper panel shows the top view of the borehole inside the rock matrix. The dummy (orange mesh) is surrounded by 1 mm meshed layer (blue), representing gap between dummy and non-fractured rock. This layer will be used for applying boundary conditions and obtaining steady state water flow solution, as well as the source of tracer injections (as it is shown in figure 4 right bottom panel or Figure 1-16 right top panel). On the left panel in Figure 1-19 the cross section along the borehole in z direction is shown: dummy is colored by orange, 1 mm layer is blue and structured mesh of surrounding rock is colored by green. The final mesh consists of 2450 nodes and 11515 tetrahedral elements.

Similar procedure is applied to generate the mesh for TDE experiment, where three boreholes are considered in non-fractured rock. Figure 1-20 shows the top view of the parallelepiped, initially meshed structurally, with three cylindrical holes in it, where the distance between cylinders centers is 0.15 m. The meshed separately cylinders are merged into the parallelepiped creating a 1 mm layer around each borehole. Figure 1-21 (right panel) shows the whole mesh with three boreholes, which represent ONK-PP326, ONK-PP324, and ONK-PP327 boreholes in TDE experiment (Figure 1-21, left panel). Figure 1-22 shows the cross section along the boreholes and zoom in on borehole mesh, where the region filled with dummy is separated by 1 mm layer from the rock matrix. The entire mesh consists of 133650 nodes and 740174 tetrahedral elements.

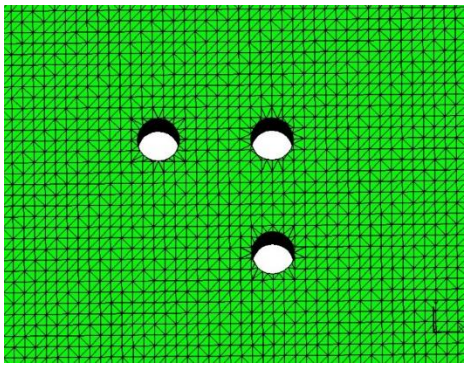

Figure 1-20. The top view of parallelepiped of size 0.7m x 0.7 m x 1.9 m. Three cylindrical holes are cut in 0.15 m distance between centers.

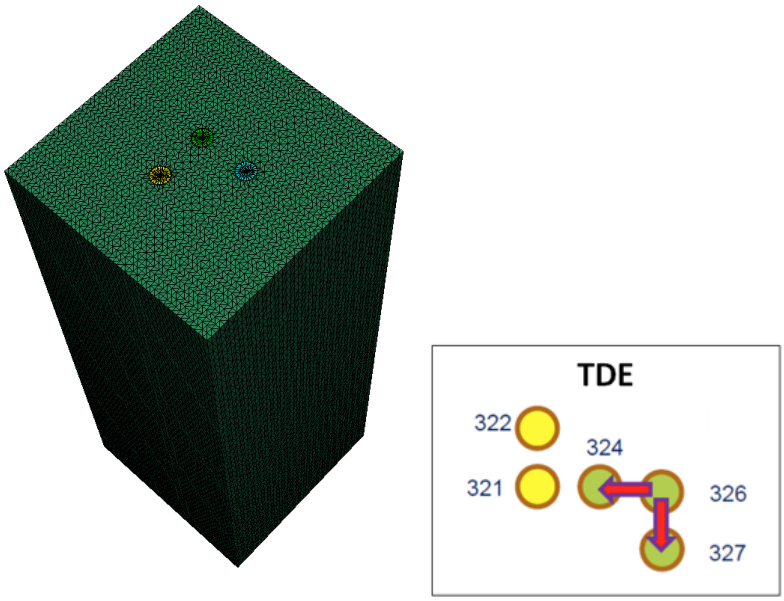

Figure 1-21. Right panel shows the whole mesh with three boreholes, which represent ONK-PP326, ONK-PP324, and ONK-PP327 boreholes in TDE experiment (left panel).

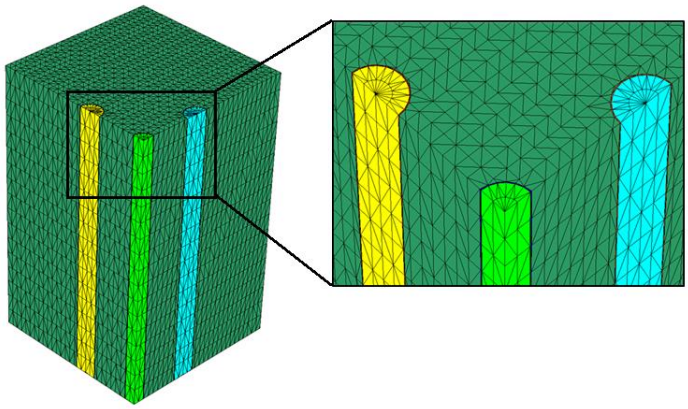

Figure 1-22. The cross section of the entire mesh along the boreholes, along z direction. The distance between central borehole and two others is 0.15 m. the zoom in figure shows the mesh of dummy filled boreholes and 1 mm layer between dummy and rock matrix.

At this point LANL team switched to Task 9B, modelling of LTDE experiment.

1.4.2 Task 9B: Increasing the Realism in Solute Transport Modelling – Modelling the Field Experiments of LTDE-SD

1.4.2.1 Long Term Sorption Diffusion Experiment (LTDE-SD)

The description of LTDE experiment is given in Löfgren (2014).

One of few recent in-situ studies focusing on tracer transport in the stagnant pore water of the rock matrix has been conducted in Sweden at the Äspö Hard Rock Laboratory, within the LTDE-SD campaign (Long Term Sorption Diffusion Experiment). In this study, a cocktail of both sorbing and non-sorbing tracers was allowed to contact a natural fracture surface, as well as the unaltered rock matrix, for a time period of 200 days. The decline in tracer concentration in the water phase was monitored. Thereafter the rock was overcored and analysed in regard to tracer concentration profiles in the rock matrix.

The illustration in the lower right of Figure 1-23 shows the location of LTDE-SD in the Äspö HRL tunnel system. In the centre of the figure, the local tunnel section is shown together with the different boreholes drilled from the site. These boreholes include the LTDE-SD borehole and the closely located pilot borehole. These two boreholes intersect a water-conducting natural fracture at a distance of about 11 m from the tunnel wall, which is the experiment's target fracture. The LTDE-SD borehole was drilled with different diameters, roughly described as follows. Up to the fracture plane the borehole has a large diameter and beyond the fracture plane a small diameter was used. This is simplistically illustrated in the lower left of Figure 1-23. The borehole is indicated by the solid black line and the intersected fracture is indicated by the curved blue line. Orange areas indicate packed-off volumes, whereas blue areas indicate volumes of the tracer cocktail. The red arrows symbolise in-diffusion of tracers from the large-diameter borehole through the fracture surface and into the underlying altered rock matrix. They also symbolise diffusion into the unaltered rock matrix from the small-diameter borehole. The dashed black line indicates the rock volume that was overcored at the end of the tracer test.

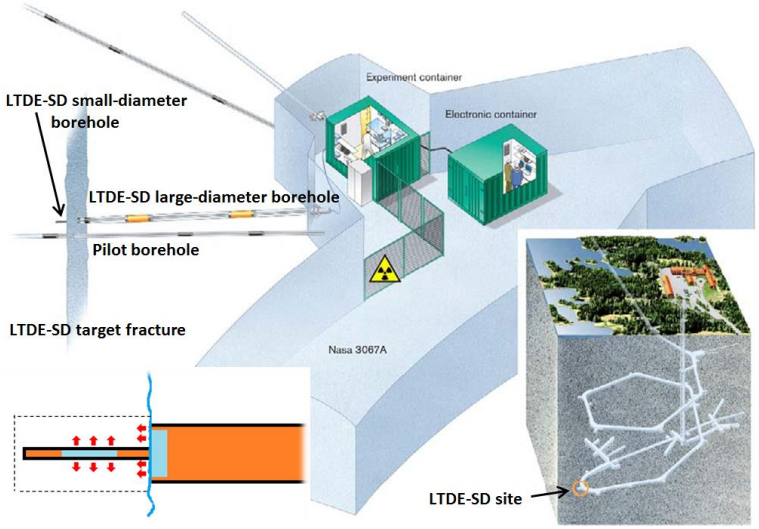

Figure 1-23. Illustrations of the LTDE-SD experimental setup.

The tracers injected were Na-22, S-35, Cl-36, Co-57, Ni-63, Se-75, Sr-85, Nb-95, Zr-95, Tc-99, Pd-102, Cd-109, Ag-110, Sn-113, Ba-133, Cs-137, Gd-153, Hf-175, Ra-226, Pa-233, U-236, and Np-237. Speciation calculations were made using PHREEQC. PEEK tubing connected the tracer cocktail volumes with experimental equipment in the tunnel. Hence, the decreasing tracer concentrations, as well as environmental parameters, could be monitored during the 200 days the tracer test progressed. After that the surrounding rock volume was overcored, and from the overcored volume a number of smaller drill cores were excavated, as illustrated on the left in Figure 1-24. Here the natural fracture surface is located on the right-hand side of the overcored rock volume.

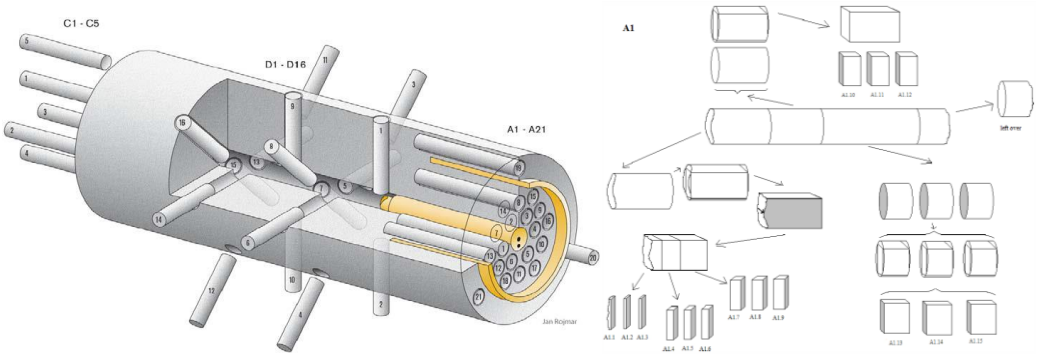

Figure 1-24. Illustration of the sampling of the overcored rock volume in LTDE-SD.

A large number of the drill core samples of Figure 1-24 were cut into subsamples as indicated to the right in Figure 1-24, enabling the obtaining of tracer penetration profiles. Tracer concentrations (or activities) in the rock were obtained by a number of analysis methods, including autoradiography on intact samples; direct activity measurements on intact and crush samples; and leaching or dissolution of intact and crush samples, followed by water phase measurements.

1.4.2.2 Problem Statement

Although the methodology and results from the experimental campaign have been reported, the outcomes have not yet been subjected to the scrutiny of a broader community of researchers and modellers. Concerning the shape of the penetration profiles, the predicted general shape discussed in the above paragraph was not observed; neither for the natural fracture surface nor for the unaltered rock matrix. Figure 1-25 shows the experimental shapes of the in-diffusing tracer Cs are shown by symbols, as well as the modelled profile by the dashed curve.

The following hypothesis is advanced during LTDE-SD experiment performance: the major diffusion of injected tracer into crystalline rock occurs through multiple micro fractures, which are observed in the rock samples. We propose to use dfnWorks modeling tool to inspect this hypothesis and to simulate diffusion and sorption processes detected by LTDE-SD experiments.

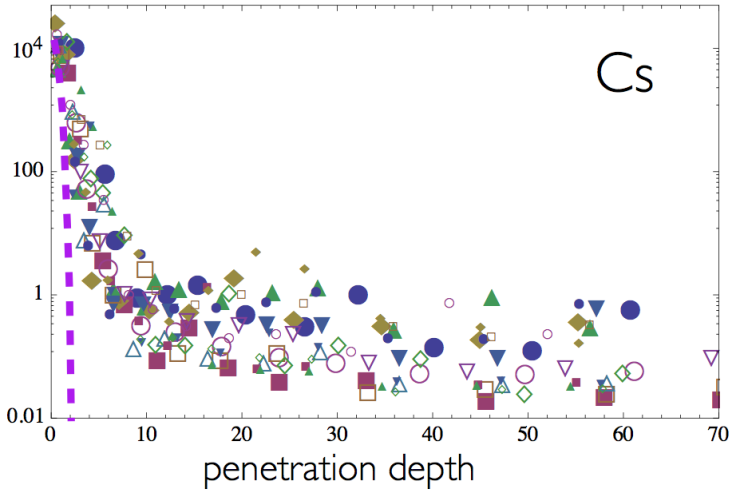

Figure 1-25. The measured experimental shapes of Cs penetration profile (symbols) do not satisfy modeled penetration profile (dashed line) (Data provided by V. Cvetkovic, TF Task9 meeting, Finland, 2015).

We use massively parallel reactive flow and transport model PFLOTRAN (Lichtner et al., 2015) to simulate flow in DFNs. PFLOTRAN allows to model transient multiphase flow, and tracer diffusion into rock matrix can be accurately measured.

In spite of the fact that dfnWorks was verified and used for large scale site simulations (e.g. Hyman et al., 2015b, Karra et al., 2015) it can be easily adapted to small scale micro fracture networks with given micro fracture statistical characteristics. Preliminary results, shown by Paolo Trinchero team, *AMPHOS 21, October 2015*, who are using DarcyTools and PFLOTRAN for modeling solute diffusion into crystalline rock (REPRO experiment, Task9A), indicate the importance of large fractures in interaction between flowing fractures and the matrix. Moreover, it is shown that the small fractures, represented by inter granular porosity in DarcyTool model, are dominating in the rock matrix. The conceptual model used in DarcyTool is shown in Figure 1-26. This concept gives us a confidence that LTDE-SD experiment can be modeled using discrete fracture network model, and dfnWorks software will provide realistic transport simulations.

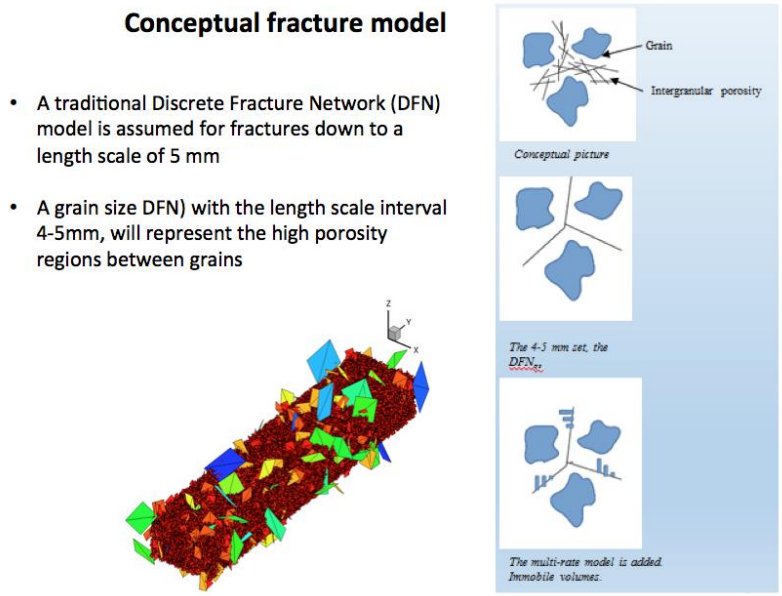

Figure 1-26. The conceptual fracture model used by AMPHOS 21 team to simulate LTDE-SD experiment.

1.4.2.3 Modeling Procedure

Base on conceptual fracture model, presented in Figure 1-26, the fracture network is generated, which represents connected micro fractures observed on the rock samples at small scale. These micro fractures are the porous spaces between grains and provide paths for tracer through the rock samples.

The domain size is 2 cm^3, where total volume of the simulation domain is 0.08m^3. There are three sets of square fractures, fracture's orientation follow Fisher Distribution, fracture's length based on Truncated Power Law distributions. The fracture statistical characteristics are presented in Table 1-5, and base on Äspö characteristics for the fracture data. Aperture of fractures is set to be uniform, 2.0×10^{-6} m. The

example of obtained DFN realization is shown in Figure 1-27. There are 36169 fractures in the DFN, the fracture intensity P_{32} = 864.718 1/m, fracture porosity P_{33} =0.0032, or 0.32%.

Table 1-5. Fracture characteristics that are used to generate micro fracture networks.

Set	**Trend**	**Plunge**	**Kappa**	**R_{Min}**	**R_{Max}**	**Alpha**	**P_{32}**
1	280	20	10	0.002	0.01	2.6	110
2	20	10	15	0.002	0.01	2.6	200
3	120	50	10	0.002	0.01	2.6	75

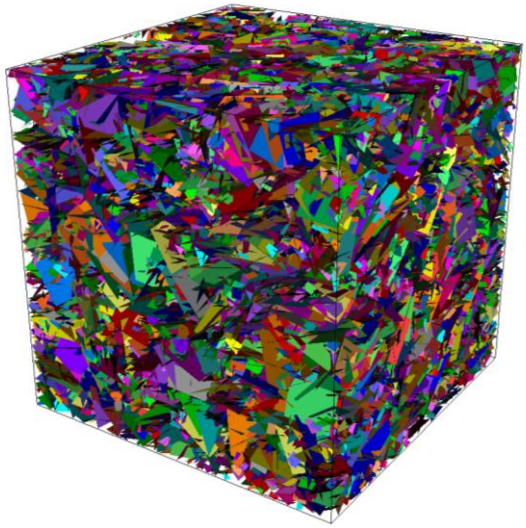

Figure 1-27. The example of DFN realization, where each micro fracture is shown by its own color. The size distribution follow truncated power low distribution, fracture characteristics are given in Table 1-5.

In order to verify that obtained DFN represents fractured rock sample, we compare two dimensional slice of the DFN with muscovite granite picture. Figure 1-28 shows the DFN slice (left) and granite picture (right), where black lines show the porous paths between grains. This visual verification allows us to proceed with flow and transport simulation for LTDE-SD modeling.

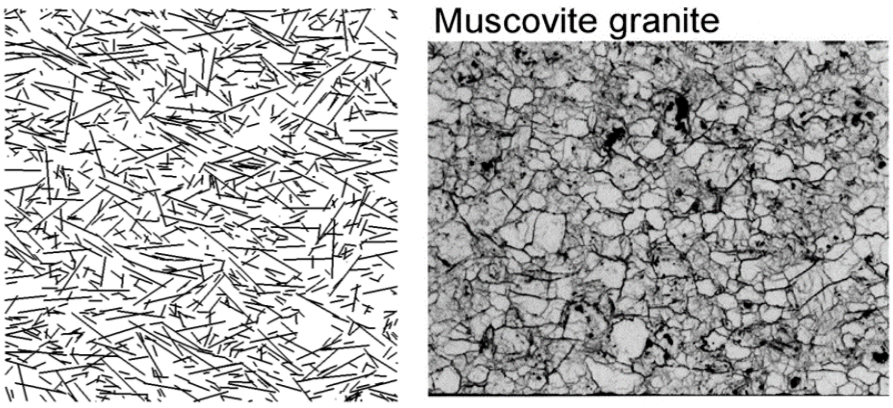

Figure 1-28. (Left) Two dimensional snapshot of a DFN realization, compared to (Right) picture of muscovite granite, where grains boundaries are black lines. Granite picture is from Maikki Siitari-Kauppi, TF #32.

DFN model represents fractures individually, where each fracture has its own permeability value. However, it completely neglects any interaction with rock matrix. LTDE experiment, on the contrary, is focused on diffusion processes. Therefore, the next step of the modeling is mapping connected micro fracture network into continuum model with following ADE simulation, where both, advective and diffusive transport processes can be modeled.

As the fracture network structure of the DFN is mapped into regular voxel mesh, each voxel is defined a permeability equal to fracture permeability that is crossing the voxel, or, if there is no fracture crossing, given rock matrix permeability value. The size of each voxel is chosen as 0.5 mm^3, what makes side length 4 times smaller than the smallest fracture length in the DFN (2mm). Figure 1-29 shows the continuum model, where red cells represent voxel crossed by fracture and blue cells represent the rock matrix. Obtained permeability and porosity profiles are shown in Figure 1-30.

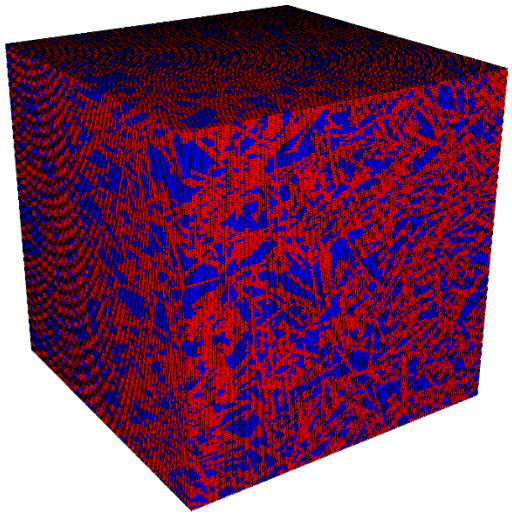

Figure 1-29. The DFN model is mapped into continuum. Red cells represent voxel crossed by fracture and blue cells represent the rock matrix.

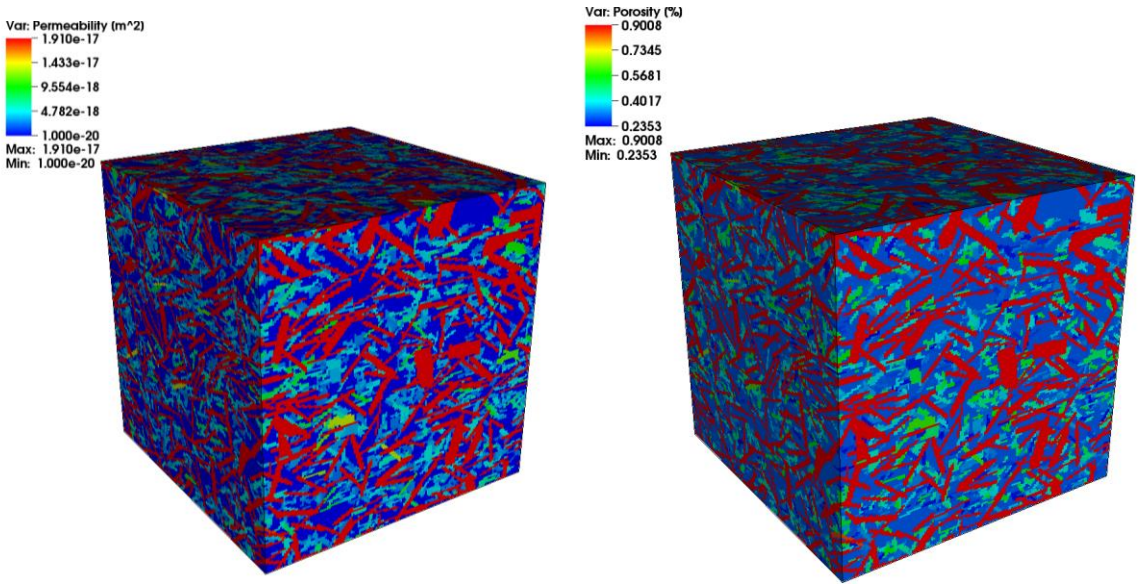

Figure 1-30. Permeability (Left) and porosity (Right) profiles are shown in the continuum simulation.

1.4.2.4 Preliminary Results

We use PFLOTRAN to run transport through the simulation domain. The tracer is injected uniformly on top face and moving toward bottom face along Z axis according ADE equation. The simulation is run for 25 days. One time frame is shown in Figure 1-31. We can see that tracer concentration is not uniform along fluid flow direction; the micro fracture cells provide faster paths for tracer than rock matrix cells due to higher permeability and higher porosity, and also advetive term.

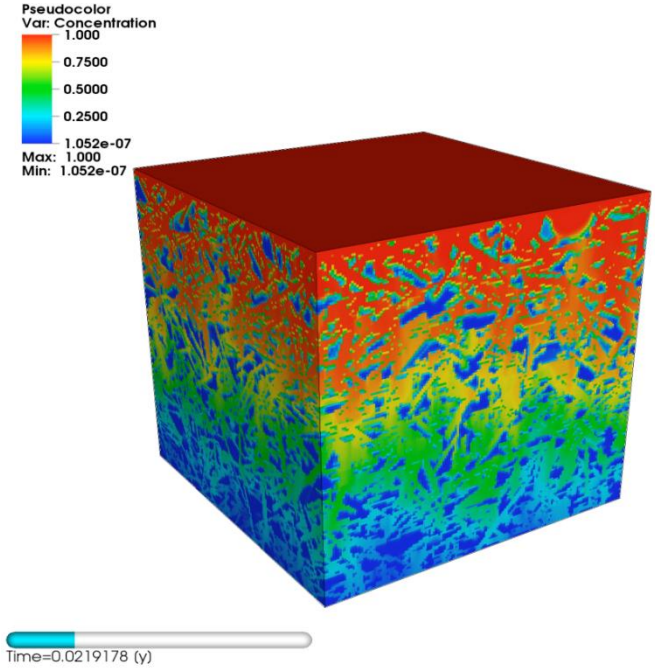

Figure 1-31. The tracer concentration of transport modeling in fractured continuum.

We measure tracer concentration and plot it versus penetration depth (Figure 1-32.) Left plot of Figure 1-32 shows our simulation results in two modeled cases: fractured system, where DFN is mapped into continuum (blue line) and uniform continuum (dashed green line). The same simulation settings, such as initial tracer location, boundary conditions and flow rates, are applied to both continuum models. This way we can clearly observe the role of micro fractures and advection part in transport. Right panel of Figure 1-32 repeats the plot of Figure 1-25 and placed here for comparison. We can see that pure diffusion case in uniform continuum model, shown in both plots by dashed lines, behave very similar and show a big difference with fractured continuum and experimental results.

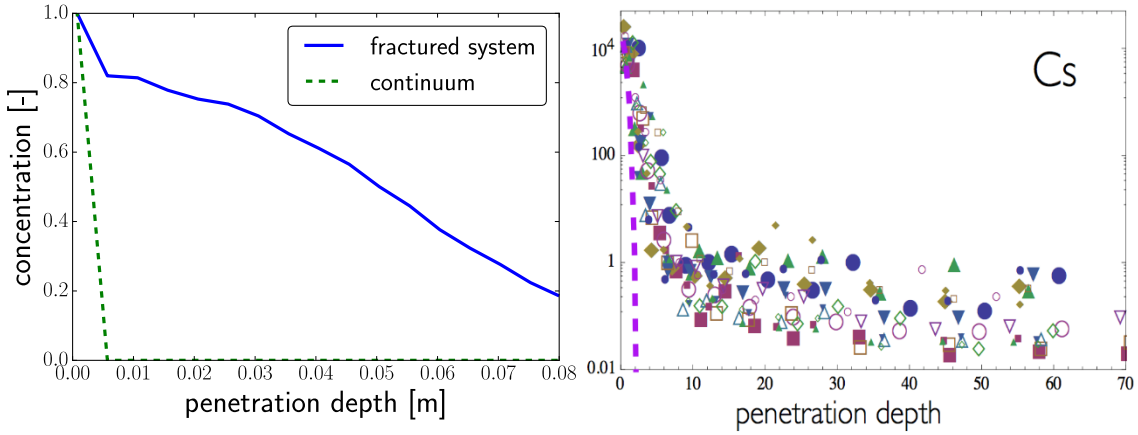

Figure 1-32. Left: the simulation results of tracer concentration plotted versus tracer penetration depth. Blue line corresponds to fractured continuum model with simulated ADE, dashed green line shows results for uniform continuum with simulated pure diffusion process. Right panel repeats plot of Figure 1-25 for comparison. Here dashed line corresponds to continuum pure diffusion modeling and symbols show the results of LTDE experiment.

1.4.2.5 Future Work

As a future work of modeling LTDE experiment using fracture network we propose following:

1. Understanding the difference between ADE simulated tracer concentration curve using fractured continuum model and the experimental results. Perhaps, the rock sample used in the experiment is a combination of both characteristics: it is fractured on boundaries, where micro fractures were induced at the stage of extracting rock sample, and it gets less fractured and become more homogeneous closer to the center. In order to check this hypothesis we can produce continuum model that will have both fractured and homogeneous parts, with following transport simulation and results comparison.

2. We have to verify several uncertainties, such as flow rate. We are not sure that flow rate observed in the experiment is similar to the flow rate we used in the simulation. Another uncertain parameter is the time: at what time the tracer concentration is shown.

3. Continuing improving our modeling tool, upgrade the procedure of mapping DFN into continuum. Moreover, in order to avoid statistical bias of stochastically generated fracture network, multiple DFN realizations required. We also need to explore the sensitivity of DFN input parameters and simulation settings.

1.5 References

Adler P. M., Thovert J. F., and Mourzenko V. V. (2012) *Fractured porous media*. Oxford University Press.

Ahmed R., Edwards M. G., Lamine S., Huisman B., and Pal M. (2015a) Control-volume distributed multi-point flux approximation coupled with a lower-dimensional fracture model, *J. Comput. Phys.*, 284, 462–489.

Ahmed R., Edwards M. G., Lamine S., Huisman B. A., and Pal M. (2015b) Three-dimensional control-volume distributed multi-point flux approximation coupled with a lower-dimensional surface fracture model, *J. Comput. Phys.*, 303, 470–497.

Ahrens J., Geveci B., and Law C. (2005) 36 paraview: An end-user tool for large-data visualization, *The Visualization Handbook*, 717.

Baghbanan A. and Jing L. (2007) Hydraulic properties of fractured rock masses with correlated fracture length and aperture, *Int. J. Rock Mech. Min.*, 44(5), 704–719.

Belfield W. C. (1998) Incorporating spatial distribution into stochastic modelling of fractures: multifractals and Lévy-stable statistics, *J. Struct. Geol.*, 20(4), 473–486.

Berkowitz B. (2002) Characterizing flow and transport in fractured geological media: A review, *Adv. Water Resour.*, 25(8-12), 861–884.

Bogdanov I., Mourzenko V., Thovert J.-F., and Adler P. (2007) Effective permeability of fractured porous media with power-law distribution of fracture sizes, *Phys. Rev. E*, 76(3), 036,309.

Bonnet E., Bour O., Odling N. E., Davy P., Main I., Cowie P., and Berkowitz B. (2001) Scaling of fracture systems in geological media, *Rev. Geophys.*, 39(3), 347–383.

Boussinesq J. (1868) Mémoire sur l'influence des frottements dans les mouvements réguliers des fluids, *J. Math. Pures Appl*, 13(377-424), 21.

Cacas M. C., Ledoux E., De Marsily G., Barbreau A., Calmels P., Gaillard B., and Margritta R. (1990) Modeling fracture flow with a stochastic discrete fracture network: Calibration and validation: 2. The transport model, *Water Resour. Res.*, 26(3), 491–500.

Charlaix E., Guyon E., and Roux S. (1987) Permeability of a random array of fractures of widely varying apertures, *Transport Porous Med.*, 2(1), 31–43.

Cvetkovic V. and Frampton A. (2012) Solute transport and retention in three-dimensional fracture networks, *Water Resour. Res.*, 48(2).

Cvetkovic V., Painter S., Outters N., and Selroos J. (2004) Stochastic simulation of radionuclide migration in discretely fractured rock near the Äspö hard rock laboratory Äspö hard rock laboratory, *Water Resour. Res.*, 40(2).

de Dreuzy J.-R., Davy P., and Bour O. (2001) Hydraulic properties of two-dimensional random fracture networks following a power law length distribution 2. Permeability of networks based on lognormal distribution of apertures, *Water Resour. Res.*, 37(8), 2079–2095.

de Dreuzy J.-R., Davy P., and Bour O. (2002) Hydraulic properties of two-dimensional random fracture networks following power law distributions of length and aperture, *Water Resour. Res.*, 38(12).

de Dreuzy J.-R., Darcel C., Davy P., and Bour O. (2004) Influence of spatial correlation of fracture centers on the permeability of two-dimensional fracture networks following a power law length distribution, *Water Resour. Res.*, 40(1).

de Dreuzy J.-R., Méheust Y., and Pichot G. (2012) Influence of fracture scale heterogeneity on the flow properties of three-dimensional discrete fracture networks, *J. Geophys. Res.- Sol. Ea.*, 117(B11).

Defays D. (1977) An efficient algorithm for a complete link method, *The Computer Journal*, 20 (4), 364–366, online Available: http://comjnl.oxfordjournals.org/content/20/4/364.abstract

Dershowitz W. (2014) *FracMan version 7.4-Interactive discrete feature data analysis, geometric modeling, and exploration simulation: User documentation*, http://fracman.golder.com/.

Dershowitz W., Winberg A., Hermanson J., Byegård J., Tullborg E., Andersson P., and Mazurek M., Äspö hard rock laboratory. Äspö task force on modelling of groundwater flow and transport of solutes. Task 6c. (2003) *A semi-synthetic model of block scale conductive structures at the Äspö HRL*, International Progress Report IPR-03-13, Swedish Nuclear Fuel and Waste Management Co., Stockholm.

Dverstorp B., and Andersson J. (1989) Application of the discrete fracture network concept with field data: Possibilities of model calibration and validation, *Water Resour. Res.*, 25 (3), 540–550.

Erhel J., De Dreuzy J.-R., and Poirriez B. (2009) Flow simulation in three-dimensional discrete fracture networks, *SIAM J. Sci. Comput.*, 31(4), 2688–2705.

Faybishenko B. (2005) *Dynamics of fluids and transport in fractured rock*, 162, American Geophysical Union.

Follin S., Hartley L., Rhén I., Jackson P., Joyce S., Roberts D., and Swift B. (2014) A methodology to constrain the parameters of a hydrogeological discrete fracture network model for sparsely fractured crystalline rock, exemplified by data from the proposed high-level nuclear waste repository site at forsmark, sweden, *Hydrogeology Journal*, 22 (2), 313–331.

Frampton A. and Cvetkovic V. (2010) Inference of field-scale fracture transmissivities in crystalline rock using flow log measurements, *Water Resour. Res.*, 46(11).

Gudmundsson A., Berg S. S., Lyslo K. B., and Skurtveit E. (2001) Fracture networks and fluid transport in active fault zones, *J. Struct. Geol.*, 23(2), 343–353.

Hartley L., Hunter F., Jackson P., McCarthy R., Gylling B., and Marsic N. (2006) *Regional hydrogeological simulations using connectflow*, Preliminary site description Laxemar subarea–version, 1.

Hatton C., Main I., and Meredith P. (1994) Non-universal scaling of fracture length and opening displacement, *Nature*, 367(6459), 160–162.

Hyman J. D., Karra S., Makedonska N., Gable C. W., Painter S. L., and Viswanathan H. S. (2015a) dfnWorks: A discrete fracture network framework for modeling subsurface flow and transport, *Comput. Geosci.*, 84, 10–19.

Hyman J. D., Painter S. L., Viswanathan H., Makedonska N., and Karra S. (2015b) Influence of injection mode on transport properties in kilometer-scale three-dimensional discrete fracture networks, *Water Resour. Res.*, 51(9), 7289–7308.

Ji S.-H., Park Y.-J., and Lee K.-K. (2011) Influence of fracture connectivity and characterization level on the uncertainty of the equivalent permeability in statistically conceptualized fracture networks, *Transport Porous Med.*, 87(2), 385–395.

Joyce S., Hartley L., Applegate D., Hoek J., and Jackson P. (2014) Multi-scale groundwater flow modeling during temperate climate conditions for the safety assessment of the proposed high-level nuclear waste repository site at forsmark, sweden, *Hydrogeol. J.*, 22(6), 1233–1249.

Kang P. K., Dentz M., Le Borgne T., and Juanes R. (2015) Anomalous transport on regular fracture networks: Impact of conductivity heterogeneity and mixing at fracture intersections, *Phys. Rev. E*, 92(2), 022,148.

Karra S., Makedonska N., Viswanathan H. S., Painter S. L., and Hyman J. D. (2015) Effect of advective flow in fractures and matrix diffusion on natural gas production, *Water Resour. Res.*, 51(10), 8646–8657.

Klimczak C., Schultz R. A., Parashar R., and Reeves D. M. (2010) Cubic law with aperture-length correlation: implications for network scale fluid flow, *Hydrogeol. J.*, 18 (4), 851–862.

Konzuk J. S. and Kueper B. H. (2004) Evaluation of cubic law based models describing single-phase flow through a rough-walled fracture, *Water Resour. Res.*, 40(2).

LaGriT (2013) *Los Alamos Grid Toolbox, (LaGriT)*, Los Alamos National Laboratory, http://lagrit.lanl.gov.

Levenshtein V. I. (1966) Binary codes capable of correcting deletions, insertions, and reversals, *Soviet physics doklady*, 10 (8), 707–710.

Lichtner P., Hammond G., Lu C., Karra S., Bisht G., Andre B., Mills R., and Kumar J. (2015) *PFLOTRAN user manual: A massively parallel reactive flow and transport model for describing surface and subsurface processes*, Tech. rep., (Report No.: LA-UR-15-20403) Los Alamos National Laboratory.

Löfgren M. (2014) *Increasing the realism in solute transport modelling – Modelling the field experiments of REPRO and LTDE-SD*, SKB Task force on Modelling of Groundwater Flow and Transport of Solutes.

Lu K., Chaudhuri A., Lee T.-Y., Shen H.-W., and Wong P. C. (2013) Exploring vector fields with distribution-based streamline analysis, *PacificVis*, 257–264.

Makedonska N., Hyman J. D., Karra S., Painter S. L., Gable C. W., and Viswanathan H. S. (2016) Evaluating the effect of internal aperture variability on transport in kilometer scale discrete fracture networks, *Adv. Water Resour.*, 94, 486-497.

Margolin G., Berkowitz B., and Scher H. (1998) Structure, flow, and generalized conductivity scaling in fracture networks, *Water Resour. Res.*, 34(9), 2103–2121.

McLoughlin T., Jones M. W., Laramee R. S., Malki R., Masters I., and Hansen C. D. (2013) Similarity measures for enhancing interactive streamline seeding, *Visualization and Computer Graphics, IEEE Transactions on*, 19 (8), 1342–1353.

Middleton R. S., Carey J. W., Currier R. P., Hyman J. D., Kang Q., Karra S., Jiménez-Martínez J., Porter M. L., and Viswanathan H. S. (2015) Shale gas and non-aqueous fracturing fluids: Opportunities and challenges for supercritical CO2, *Appl. Energ.*, 147, 500–509.

Molz F. J., Rajaram H., and Lu S. (2004) Stochastic fractal-based models of heterogeneity in subsurface hydrology: Origins, applications, limitations, and future research questions, *Rev. Geophys.*, 42(1).

Mustapha H. and Mustapha K. (2007) A new approach to simulating flow in discrete fracture networks with an optimized mesh, *SIAM J. Sci. Comput.*, 29, 1439.

National Research Council (1996) *Rock fractures and fluid flow: contemporary understanding and applications*, National Academy Press.

Neuman S. (2005) Trends, prospects and challenges in quantifying flow and transport through fractured rocks, *Hydrogeol. J.*, 13(1), 124–147.

Painter S. and Cvetkovic V. (2005) Upscaling discrete fracture network simulations: An alternative to continuum transport models, *Water Resour. Res, 41*, W02, 002.

Painter S., Cvetkovic V., and Selroos J.-O. (2002) Power-law velocity distributions in fracture networks: Numerical evidence and implications for tracer transport, *Geophys. Res. Lett.*, 29 (14), 20–1–20–4.

Patriarche D., Pili E., Adler P. M., and Thovert J.-F. (2007) Stereological analysis of fractures in the roselend tunnel and permeability determination, *Water Resour. Res.*, 43(9).

Pichot G., Erhel J., and De Dreuzy J. (2010) A mixed hybrid mortar method for solving flow in discrete fracture networks, *Appl. Anal.*, 89(10), 1629–1643.

Pichot G., Erhel J., and De Dreuzy J. (2012) A generalized mixed hybrid mortar method for solving flow in stochastic discrete fracture networks, *SIAM J. Sci. Comput.*, 34 (1), B86–B105.

Pobitzer A., Peikert R., Fuchs R., Schindler B., Kuhn A., Theisel H., Matković K., and Hauser H. (2011) The state of the art in topology- based visualization of unsteady flow, *Computer Graphics Forum*, 30 (6), 1789–1811.

Renshaw C. E. (1995) On the relationship between mechanical and hydraulic apertures in rough-walled fractures, *J. Geophys. Res.-Sol. Ea.*, 100(B12), 24,629–24,636.

Renshaw C. E. and Park J. C. (1997) Effect of mechanical interactions on the scaling of fracture length and aperture, *Nature*, 386(6624), 482–484.

Roubinet D., Liu H.-H., and De Dreuzy J.-R. (2010) A new particle-tracking approach to simulating transport in heterogeneous fractured porous media, *Water Resour. Res.*, 46(11).

Salzbrunn T., Jänicke H., and Wischgoll T. (2008) The State of the art in flow visualization: Partition-based techniques, *SimVis*, 75–92.

SKB (2011) *Long-term safety for the final repository for spent nuclear fuel at forsmark, main report of the sr-site project*, SKB TR-11-01.

Svensk Kärnbränslehantering AB (2010) *Data report for the safety assessment SR-site (TR-10-52)*, Tech. rep., Svensk Kärnbränslehantering AB.

Svensk Kärnbränslehantering AB (2011), *Data report for the safety assessment SR-site (TR-11- 01)*, Tech. rep., Svensk Kärnbränslehantering AB.

Trimmer D., Bonner B., Heard H., and Duba A. (1980) Effect of pressure and stress on water transport in intact and fractured gabbro and granite, *J. Geophys. Res.-Sol. Ea.*, 85 (B12), 7059–7071.

Uchida M. (1994) *Discrete-fracture modelling of the Äspö LPT-2, large-scale pumping and tracer test*, Svensk kärnbränslehantering AB.

Vermilye J. M. and Scholz C. H. (1995) Relation between vein length and aperture, *J. Struct.Geol.*, 17(3), 423–434.

Walmann T., Malthe-Sørenssen A., Feder J., Jøssang T., Meakin P., and Hardy H. H. (1996) Scaling relations for the lengths and widths of fractures, *Phys. Rev. Lett.*, 77, 5393–5396.

Wellman T. P., Shapiro A. M., and Hill M. C. (2009) Effects of simplifying fracture network representation on inert chemical migration in fracture-controlled aquifers, *Water Resour. Res.*, 45(1).

Willmann M., Lanyon G., Marschall P., and Kinzelbach W. (2013) A new stochastic particle-tracking approach for fractured sedimentary formations, *Water Resour. Res.*, 49(1), 352–359.

Wilson R. and Hancock E. (2004) Levenshtein distance for graph spectral features, *Pattern Recognition, 2004. ICPR 2004. Proceedings of the 17th International Conference on*, 2, 489–492.

Witherspoon P. A., Wang J., Iwai K., and Gale J. (1980) Validity of cubic law for fluid flow in a deformable rock fracture, *Water Resour. Res.*, 16(6), 1016–1024.

Xu C., Dowd P., Mardia K., and Fowell R. (2006) A connectivity index for discrete fracture networks, *Math. Geol.*, 38(5), 611–634.

Yu H., Wang C., Shene C.-K., and Chen J. H. (2012) Hierarchical streamline bundles, *Visualization and Computer Graphics, IEEE Transactions on*, 18(8), 1353–1367.

Zimmerman R. W. and Bodvarsson G. S. (1996) Hydraulic conductivity of rock fractures, *Transport Porous Med.*, 23(1), 1–30.

2. INTERPRETATION OF COLLOID-FACILITATED RADIONUCLIDE TRANSPORT EXPERIMENTS IN A CRYSTALLINE GRANODIORITE AT THE GRIMSEL TEST SITE, SWITZERLAND

2.1 Introduction

Three colloid-facilitated radionuclide transport experiments were conducted at the Grimsel Test Site (GTS) between 2002 and 2013. Additionally, a fourth test involving radionuclides but no colloids was also conducted in 2002. The GTS is an Underground Research Laboratory in a crystalline granodiorite in the Swiss Alps. The tests were conducted in a saturated shear zone at the GTS, called the MI shear zone, which is dominated by a steeply-dipping planar flow feature that intersects a major access tunnel (the AU tunnel). Fig. 2-1 shows the locations of selected boreholes within the MI shear zone, including the injection and extraction locations for each of the three colloid-facilitated radionuclide transport experiments and also the experiment in which radionuclides were injected without colloids.

The first of the three colloid-facilitated radionuclide transport tests was conducted as part of the Colloids and Radionuclide Retention (CRR) program in 2002. This test, CRR Run 32, was a 'dipole test' that was carried out between two boreholes intersecting the shear zone, with the radionuclide/colloid 'cocktail' being injected at ~10 mL/min into borehole CRR 99.002 and the pextraction hole, BOMI 87.010, being pumped at ~150 mL/min (Fig. 2-1). The mean conservative tracer residence time in the shear zone in this dipole configuration was on the order of about 2 hours, which ensured high recoveries of injected radionuclides

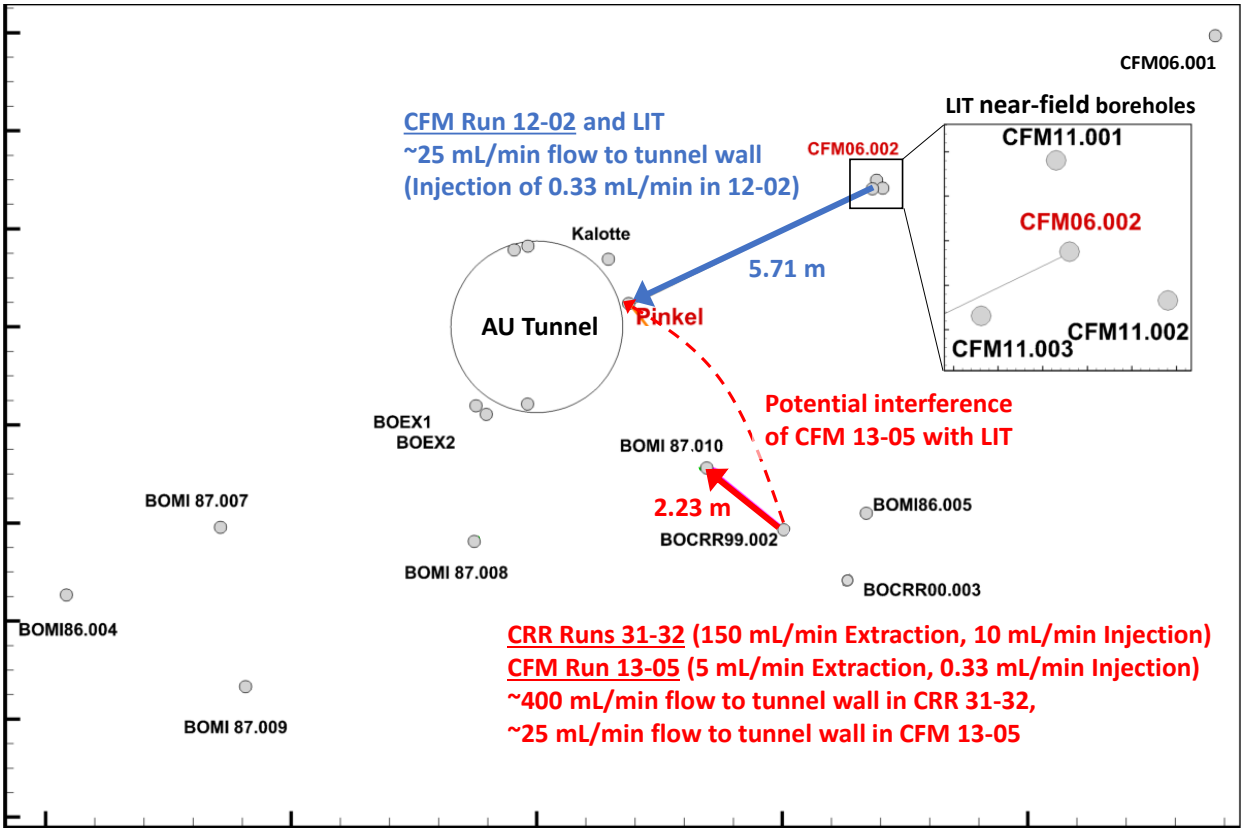

Figure 2-1. Configurations and flows in the GTS MI shear zone for the colloid-facilitated radionuclide transport experiments discussed in this report (underlined). LIT refers to the long-term in-situ test involving emplacement of a radionuclide-doped bentonite plug into CFM 06.002.

and minimal spread of contamination in the shear zone. CRR Run 32 was preceded by a radionuclide cocktail injection without colloids (CRR Run 31), which was conducted in an identical flow configuration as Run 32, thus offering the opportunity to compare the transport behavior of the same radionuclides in both the absence and presence of colloids. Details of the CRR transport experiments at the GTS, including Runs 31 and 32, are provided in Möri (2004).

A second colloid-facilitated radionuclide transport experiment was conducted in the MI shear zone in 2012 as part of the Colloids Formation and Migration (CFM) program, a successor program to the CRR program that was initiated in 2004. The U.S. Department of Energy participated as a partner in the CFM program from 2013 to 2015. In this second colloid-facilitated radionuclide transport experiment, CFM Run 12-02, a radionuclide-colloid cocktail was injected at ~0.33 mL/min into shear-zone borehole CFM 06.002, and the extraction location was a surface packer at the AU tunnel wall (called the Pinkel packer) that received shear zone water at a flow rate of ~25 mL/min (Fig. 2-1). The tunnel wall acts as a hydraulic sink for the shear zone, and it flows at several hundred mL/min if the flow is not held back with surface packers. An interpretation of this test was previously provided by the author in Chapter 2 of Wang et al. (2013); it was concluded that the mean water residence time in the shear zone in this test was about 36 hours, or about 18 times longer than in CRR Run 32. The injection interval for this test has since been filled with a radionuclide-doped bentonite plug that is being allowed to swell and erode to release radionuclides and colloids into the shear zone. This test is being called the Long-Term In-Situ Test, or LIT (Kontar and Rösli, 2014). Sampling for the LIT is being conducted both from three small boreholes completed near CFM 06.002 (see Fig. 2-1 inset) and at the Pinkel surface packer at the tunnel wall, which continues to receive shear zone water at ~25 mL/min.

A third colloid-facilitated radionuclide transport experiment, CFM Run 13-05, was conducted in 2013 using the same two boreholes as in CRR Runs 31 and 32 but with the injection and extraction flow rates reduced to 0.33 mL/min and 5 mL/min, respectively. This test was preceded by a series of conservative dye tracer tests that established that the injection of radionuclides and colloids into CRR 99.002 would not interfere with the LIT and also that high recoveries of injected radionuclides at BOMI 87.010 could still be expected despite the much lower flow rates than in CRR Runs 31 and 32. The mean conservative tracer residence time in CFM Run 13-05 was similar to that for CFM Run 12-02, i.e., over an order of magnitude greater than in CRR Run 32.

The purpose of this report is to provide internally consistent interpretations of the three colloid-facilitated radionuclide transport experiments so that the model parameters describing colloid-facilitated transport can be compared and contrasted in the same configuration at different shear zone residence times (CRR Run 32 and CFM Run 13-05) and also in different parts of the shear zone but at similar residence times (CFM Runs 12-02 and 13-05). These comparisons were expected to yield insights into both the time-scaling behavior of colloid-facilitated radionuclide transport and also heterogeneity of transport properties with the MI shear zone. This effort complements a previous effort by Kosakowski and Smith (2004) to model the CRR experiments.

2.2 Summary of Tracer Tests CRR 31-32, CFM 12-02 and CFM 13-05

The experimental parameters and test conditions associated with each of the GTS colloid-facilitated radionuclide transport experiments, including CRR Run 31 which had radionuclides but no colloids, are summarized in Table 2-1. The normalized tracer breakthrough curves (extraction concentrations divided by injection masses as a function of time) in each test are shown in Figures 2-2 through 2-5. The estimated percent recoveries of each radionuclide are listed in parentheses next to the radionuclide names in the legends of these figures. Additional information about each experiment can be obtained from Möri (2004) for the CRR tests and from the Quick-Look reports issued for CFM Runs 12-02 and 13-05 (Kontar and Gräfe, 2012 and Kontar et al., 2013, respectively). Several points are worthy of mention regarding the tests:

1. For the two CRR runs, ^{131}I was used as a conservative (nonreactive) tracer, and no fluorescent dyes were used. The radionuclide-colloid injections in both CRR tests were accomplished by interrupting the 10 mL/min flow of untraced shear zone water into CRR 99.002 with a 100-ml slug of the cocktail solution injected at the same flow rate (10 mL/min) for 10 minutes and then immediately switching back to a 10 mL/min flow of untraced shear zone water.
2. For the two CFM runs, Amino-G Acid (AGA) was used as a conservative tracer. In these tests, a 2250 mL container of radionuclide-colloid cocktail was inserted into a flow loop of approximately 1000 mL to create an injection circuit of approximately 3250 mL that contained all of the injection cocktail. The solution in this circuit was circulated through the packed-off injection interval in the shear zone at a rate of about 20 mL/min while maintaining a net inflow rate of ~0.33 mL/min to slowly force the cocktail into the shear zone. The circulation between the shear zone and the access tunnel allowed the injection circuit to be sampled over time. This injection method resulted in approximately an exponential decay of tracer/radionuclide concentrations in the injection circuit over time. The decay in concentrations occurred over time scales that were quite long relative to the transport time in the shear zone. Therefore, the resulting injection functions for the CFM tests had to be properly accounted for in test interpretations to ensure that transport parameters were estimated only for the time that radionuclides and colloids spent in the shear zone, not in the injection/circulation loop.
3. The colloids used in each experiment were generated from natural FEBEX bentonite (taken from a mine in Spain) by dispersing the bentonite in a synthetic GTS groundwater, collecting the colloidal fraction, ensuring the stability of the colloidal fraction over time, and then diluting the colloids to the target injection concentration (Möri, 2004). A "cocktail" was prepared for injection by adding all the radionuclides to the colloid dispersion prepared in this manner. The fraction of each radionuclide adsorbed to the colloids at the time of injection was determined by analyzing the supernatant of an ultra-centrifuged sample of the injection cocktail at approximately the time of injection. The colloid concentration in the CRR Run 32 injection cocktail was 20 mg/L, whereas the colloid concentration in the two CFM cocktails was ~100 mg/L.
4. The concentrations of the actinides Th, Pu, Am, U and Np were measured by ICP-MS at the Karlsruhe Institute of Technology (KIT), Karlsruhe, Germany. ^{99}Tc, which was used only in CRR Run 32, was also analyzed by ICP-MS at KIT. The concentrations of ^{22}Na, ^{85}Sr, ^{137}Cs and ^{133}Ba were measured by gamma spectrometry at KIT. Bentonite colloid concentrations and size distributions were measured in the field using a mobile laser-induced breakdown detection (LIBD) system operated by KIT personnel, and they were also measured offsite by LIBD at KIT. Additionally, for the two CFM runs, colloid concentrations were determined at KIT by background-subtracted ICP-MS measurements of Ni, as the bentonite colloids in these tests were labeled with Ni (Reinholdt et al., 2013), which had a very low background concentration in the shear zone water. The LIBD data were used to generate the colloid breakthrough curves for CRR Run 32, and the ICP-MS Ni data were used to generate the colloid breakthrough curves for the CFM tests.
5. As Table 2-1 indicates, the radionuclide associations with colloids (numbers in parentheses listed directly below each radionuclide mass) varied significantly in the different tests for some radionuclides. The most notable differences were for ^{133}Ba, ^{137}Cs, U, and ^{237}Np. The reasons for these differences are not readily explainable, but the most likely explanations are: (1) For ^{137}Cs, the concentrations in the CRR Run 32 injection cocktail were much higher than in the CFM cocktails, and the colloid concentration was lower in the CRR 32 cocktail than in the CFM cocktails; so it is likely that the combination of these factors resulted in suppression of the overall fraction of ^{137}Cs adsorbed to the colloids in the CRR run. (2) The times at which colloid associations were measured for the CRR Run 32 and CFM 12-02 cocktails were within a week of cocktail preparation, but the colloid associations in the CFM 13-05 cocktail were measured approximately 400 days after cocktail preparation (and the injection was also conducted long after cocktail preparation), so the longer contact times between the radionuclides and colloids

may have resulted in significantly different colloid associations in CFM Run 13-05 than in the other tests. It is also possible that the U(VI) and Np(V) added to the CFM 13-05 cocktail partially reduced to U(IV) and Np(IV), respectively, during the long time that this cocktail was stored. These lower oxidation states would be expected to be more strongly associated with the colloids than the higher oxidation states. The different initial radionuclide associations were accounted for explicitly in the model interpretations of the respective tests.

Table 2-1. Summary of experimental parameters and test conditions in the colloid-facilitated radionuclide transport tests (see Fig. 2-1 for test configurations).

Parameter	CRR 31	CRR 32	CFM 12-02	CFM 13-05
Extraction Flow Rate, mL/min	150	150	25	5
Injection Flow Rate, mL/min	10	10	0.33	0.33
Injection Volume, mL (includes circulation loop volume for CFM tests)	100	100	3218	3218
Injection Loop Circulation Flow Rate, mL/min	N/A	N/A	20	20
Amino G Acid Injected, mg	---	---	3.7	4.45
Colloid Mass Injected, mg	---	~2	~225	~225
^{131}I mas injected, μg	1.63×10^{-5}	1.21×10^{-5} (0)	---	---
^{22}Na mass injected, μg	---	---	0.005 (0-3.5%)	0.0065 (3.9%)
^{85}Sr mass injected, μg	1.09×10^{-4}	9.41×10^{-5} (0)	---	---
^{99}Tc mass injected, μg	---	0.103 (12%)	---	---
^{133}Ba mass injected, μg	---	---	0.21 (24-34%)	1.02 (59.3%)
^{137}Cs mass injected, μg	---	0.19 (8%)	0.24 (97-98%)	0.27 (63.9%)
^{232}Th mass injected, μg	0.26	0.255 (94%)	---	2.35 (99.1%)
$^{233 \text{ or } 238}$U mass injected, μg	22.6	20.2 (6%)	---	0.225 (83.5%)
^{237}Np mass injected, μg	22.4	25.8 (0.5%)	4.8 (<1%)	4.59 (30.9%)
$^{241 \text{ or } 243}$Am mass injected, μg	0.144	0.016 (99%)	0.035 (99+%)	0.235 (99.6%)
$^{238, 242 \text{ or } 244}$Pu mass injected, μg	0.242	0.165 (84%)	1.6 (99+%)	1.09 (99.6%)

Numbers in parentheses listed beneath each radionuclide mass are the percentage of injected mass estimated to be associated with colloids at the time of injection. Note that the colloid associations are quite different in the different tests. Differences between CFM 12-02 and CFM 13-05 may have been influenced by the different times after cocktail preparation that the associations were measured: 2-7 days for CFM 12-02 and 401 days for CFM 13-05. There were no colloids in the CRR 31 injection

cocktail. Injection concentrations can be calculated by dividing injection masses by the injection volumes listed in the third row of the table.

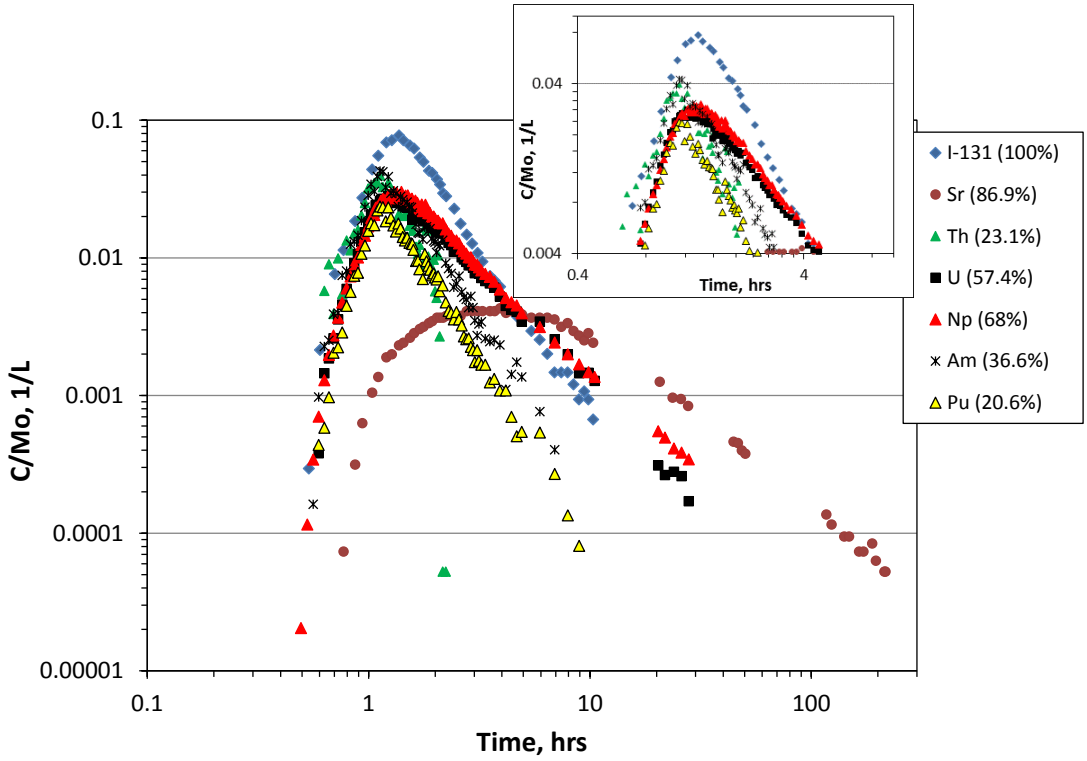

Figure 2-2. Normalized breakthrough curves in CRR Run #31 (recoveries indicated in parentheses). Inset shows details near peak concentrations.

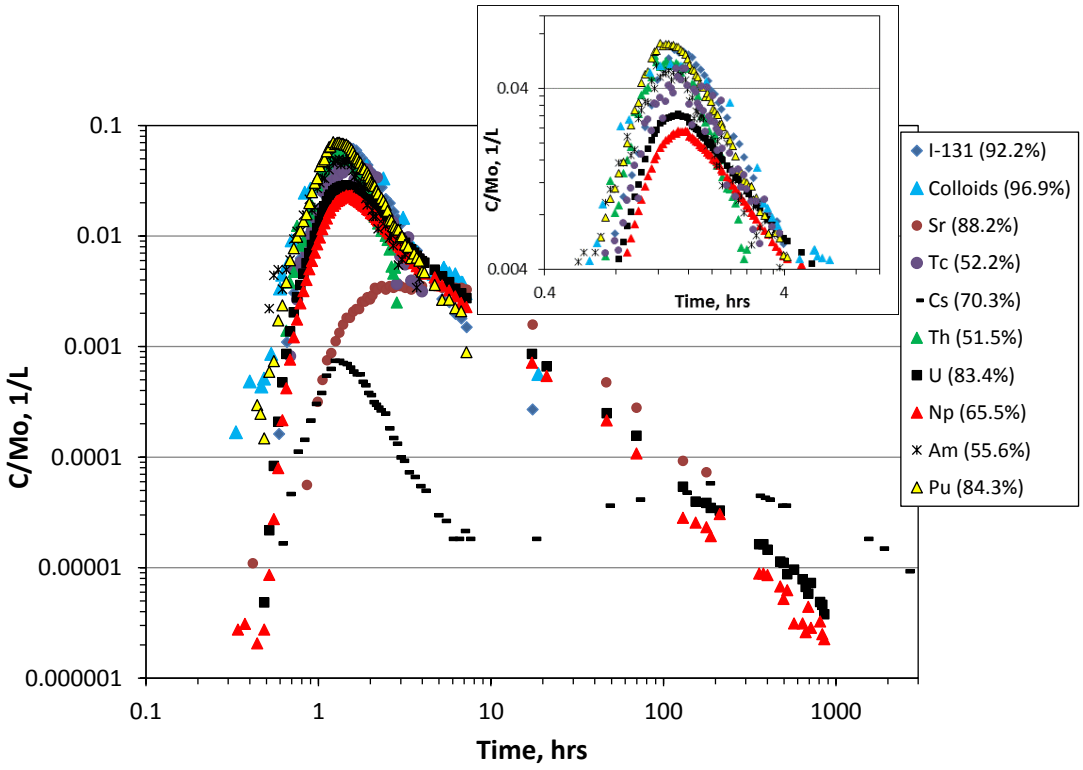

Figure 2-3. Normalized breakthrough curves in CRR Run #32 (recoveries indicated in parentheses). Inset shows details near peak concentrations.

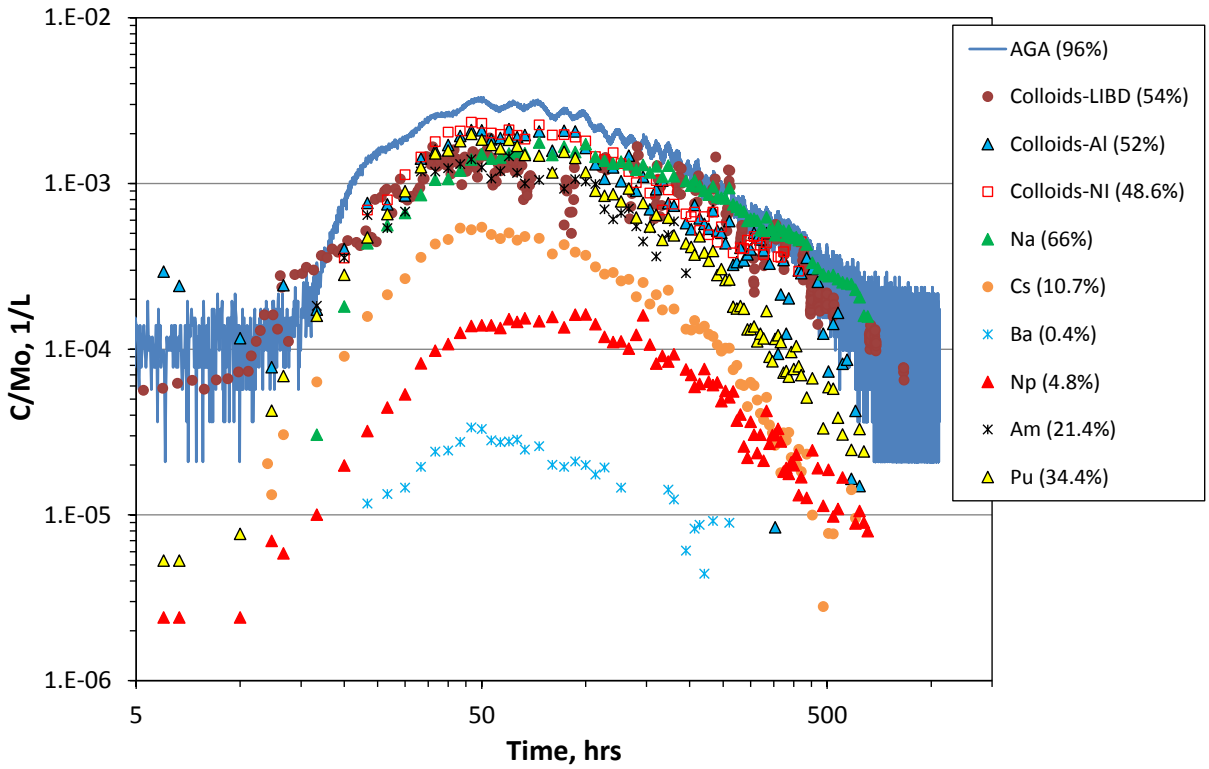

Figure 2-4. Normalized breakthrough curves in CFM Run 12-02 (recoveries indicated in parentheses).

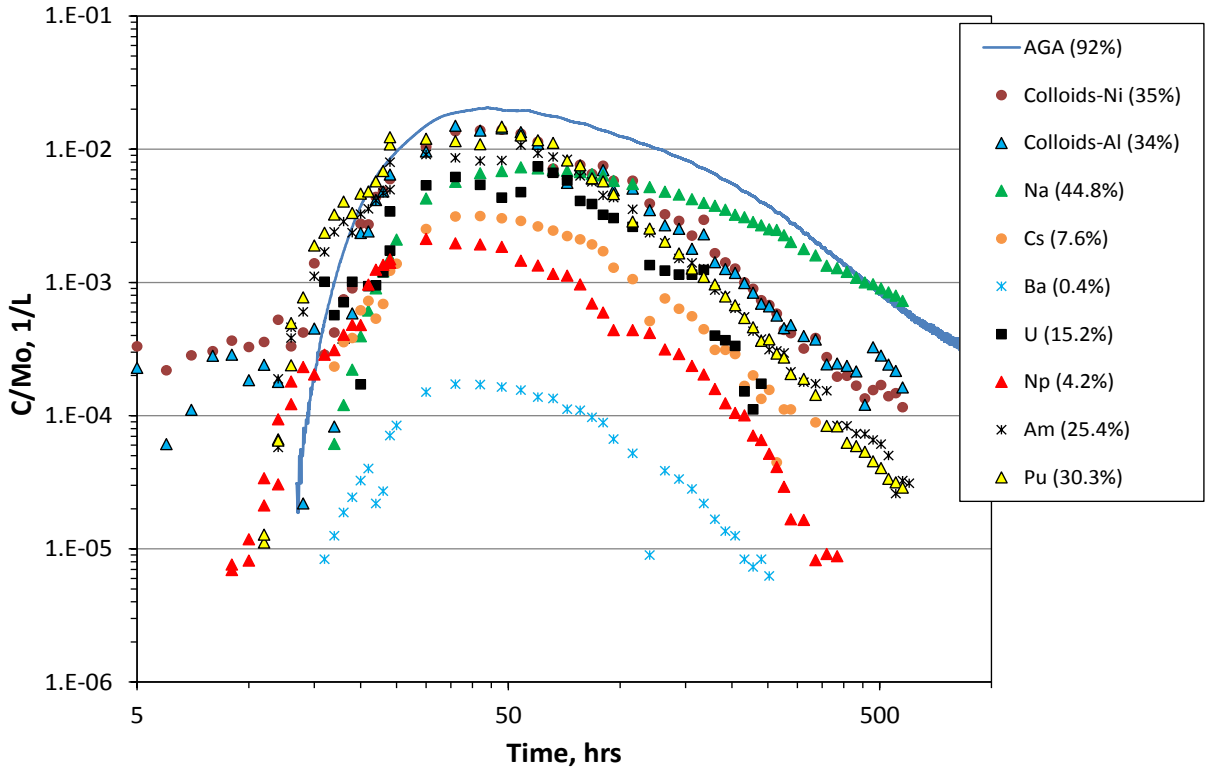

Figure 2-5. Normalized breakthrough curves in CFM Run 13-05 (recoveries indicated in parentheses).

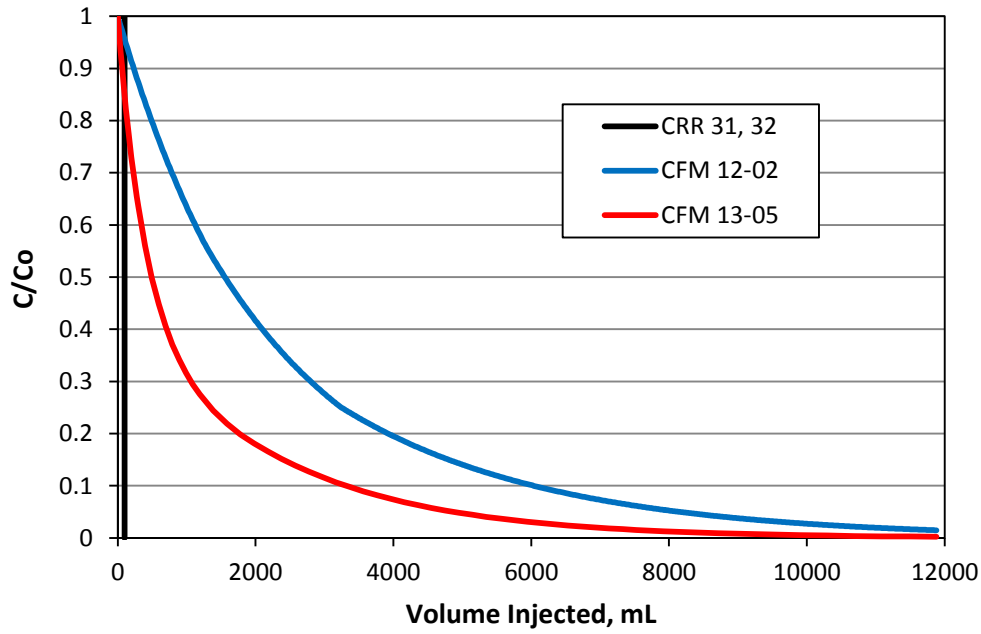

Figure 2-6. Normalized injection concentration histories as function of volume injected in the four radionuclide-colloid experiments. Note that CRR Runs 31 and 32 had same histories that were very short (100-mL) pulses.

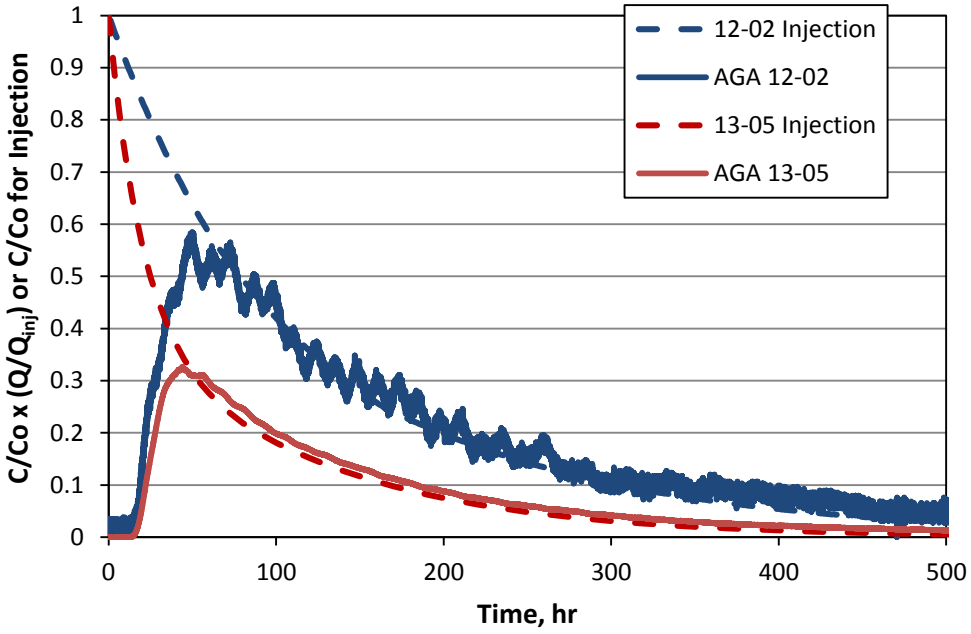

Figure 2-7. Normalized extraction and injection concentration histories in the two CFM tests.

Fig. 2-6 shows the normalized injection concentration histories (smoothed) for each of the four tests plotted as a function of volume injected. The injection histories for the two CRR tests were not measured but are inferred to be simple 100-ml pulses based on descriptions of how the tests were conducted. The injection histories for the two CFM tests were measured by sampling the injection circulation loops, and they show the roughly exponential decay of tracer concentration during the tests. Fig. 2-7 shows how the extraction concentration histories closely follow the injection concentration histories in both CFM tests after accounting for dilution (dilution factor = extraction rate divided by injection rate). This figure shows that much of the tailing in both of the CFM tests can be attributed to the slow decline in injection concentrations and not to dispersion of tracers in the shear zone. Note that the cyclic fluctuations in the extraction concentration history for CFM Run 12-02 shown in Fig. 2-7 were typical of all tests conducted between borehole CFM 06.002 and the Pinkel surface packer at the tunnel wall. These fluctuations are believed to be caused by cyclic changes in flow patterns in the shear zone caused by a combination of barometric effects and earth tides.

In Fig. 2-6 it is apparent that despite the two CFM tests having the same controlled injection rate of 0.33 mL/min, the Run 13-05 injection concentrations declined significantly faster than the 12-02 concentrations, which suggests that the actual injection rate in Run 13-05 was significantly faster than in Run 12-02 (at least during the early portion of the tests). The negative of the slope of a plot of the natural log of injection concentration vs. time multiplied by the circulation interval volume provides an estimate of the instantaneous injection rate in any given test. Fig. 2-8 shows the resulting estimated instantaneous injection rates as a function of time in the two CFM tests along with a dashed line to indicate the intended injection rate of 0.33 mL/min. Both tests exhibited greater-than-intended injection rates in the early portions of the tests, with a leveling off of the injection rates after a little more than 100 hours. The injection rate early in Run 13-05 greatly exceeded the planned injection rate. Furthermore, whereas the Run 12-02 injection was defined by two distinct injection rates with a clear break at around 120 hours, the Run 13-05 injection exhibited a continuous decline in injection rate up until about that same time. The reasons for this decline are unknown, but it is important that it be accounted for when interpreting the tracer test because the observed extraction concentrations are highly dependent on the rate at which

tracers/colloids/radionuclides leave the injection interval and enter the shear zone. The variations in injection rate also cause a time dependence of the dilution factor (ratio of extraction to injection rate), which must be accounted for when interpreting a test using a transport model that assumes only 1-D flow, as was done for this report (see next section). For Run 12-02, the injection rate variations were not large enough to cause significant errors in modeled concentrations, but for Run 13-05, the variations during the early portion of the test were large enough to have a big impact on modeled concentrations and thus a significant impact on test interpretations. Indeed, the magnitude of the Run 13-05 injection rate variations were far greater than in any previous CFM tracer test that the author has interpreted.

To account for the variations in apparent injection rates in CFM Run 13-05, the first step taken was to determine the mass associated with the injection function by effectively integrating the product of the deduced instantaneous injection flow rate and the observed instantaneous conservative tracer (AGA) injection concentration over time. The mass obtained by this procedure was about 1.2 times greater than the reported injection mass, which implies that either the estimated flow rates are too high or the observed concentrations are too high, or both.

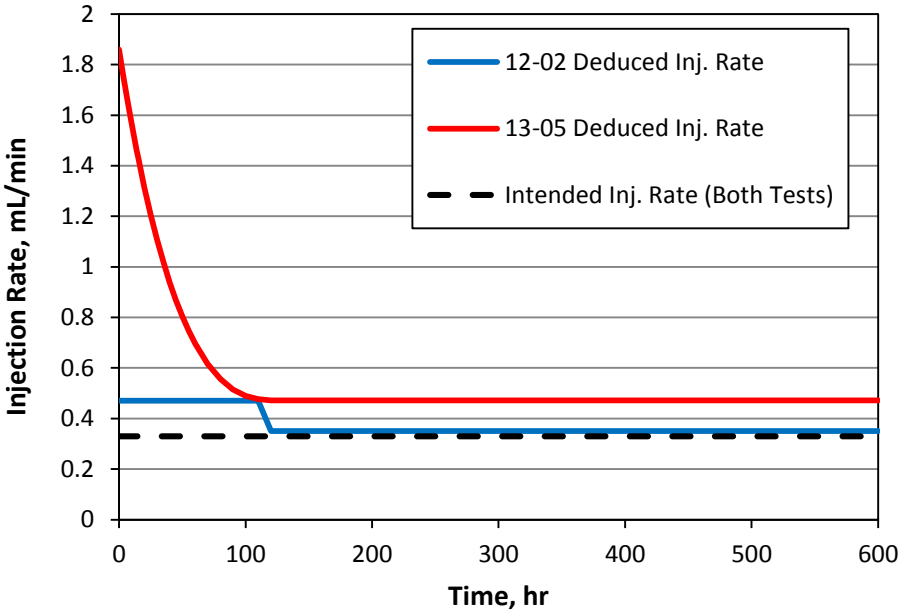

Figure 2-8. Estimated injection rates as a function of time in the two CFM tests based on the slope of the natural log of concentration vs. time multiplied by injection loop volume. The dashed line is the intended injection rate.

Because it is not possible to know whether the flow rate or concentrations are erroneous, two methods of ensuring mass balance were employed. In the first method, the injection flow rate for the entire test was assumed to be the flow rate that was observed after 120 hours (0.47 mL/min), and the initial injection concentration was assumed to be the reported injection mass divided by the injection interval volume. This approach guaranteed perfect mass balance in the injection interval. The second approach was to use the deduced flow rates, but to reduce the initial concentration in the injection interval by a factor of 1.2 to achieve mass balance. The resulting assumed AGA injection functions relative to the observed injection function are shown in Fig. 2-9. Although the constant-rate injection function has greater area under its curve in this figure, the mass associated with the two solid curves are the same because of the larger injection flow rate in the early portion of the test for the varying-inflow curve.

The interpretive modeling approach used in this report (discussed in the next section) involved the application of a numerical model that assumes only 1-dimensional flow, so there is no transverse dispersion to account for spatial variations of tracer concentrations that must occur near the injection borehole when injection rates vary. Instead, a dilution factor (ratio of extraction to injection flow rates) must be explicitly incorporated into the model calculations; i.e., the modeled extraction concentrations are divided by the dilution factor. The dilution factor in the case of assuming a constant-rate injection function was constant throughout the test (5/0.47 = 10.64), which is easy to implement in the model; but in the case of the varying-rate injection function, the dilution factor must be varied throughout the test. This poses a problem because the tracer arrival time at the extraction point is delayed relative to its injection time, so the instantaneous dilution factor at the time of tracer arrival can be quite different than the dilution factor at the time of injection. When the instantaneous dilution factors associated with the varying-inflow injection function were used without any time adjustments, it was found that the modeled tracer extraction mass recovery was far less than the injection mass because the dilution factors were always greater at the time of tracer recovery than the time of tracer injection. To address this problem, the dilution factor applied at any given time was taken to be the ratio of extraction to injection flow rates that occurred at an earlier time during the test. The offset in time was fixed throughout the test, and it was adjusted by trial-and-error until the calculated AGA tracer mass recovery was approximately 100%. It was found that a time offset of 50 hours, with the dilution factor during the first 50 hours of the test assumed to be equal to the initial dilution factor, yielded 100% mass recovery, so this offset was assumed for all the varying inflow rate test interpretations.

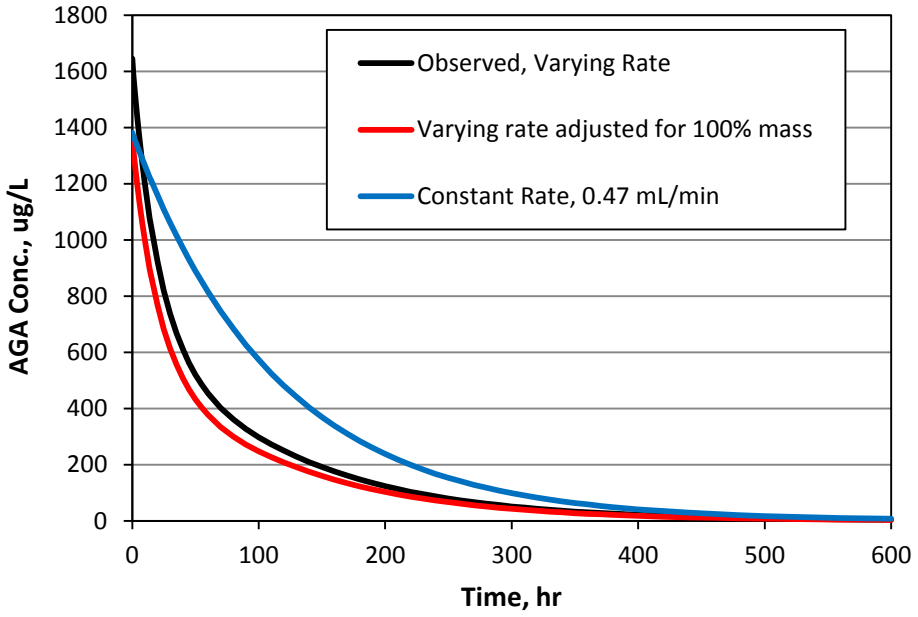

Figure 2-9. Observed (black) and two different assumed injection functions in CFM Run 13-05. The observed curve yields 120% mass injection, whereas the two assumed curves correspond to 100% mass injection.

Because colloid filtration and radionuclide interactions with shear zone surfaces are assumed to occur only while colloids and radionuclides are in the shear zone, it is important to know the conservative tracer residence time distributions in the shear zone for each of the tests. Fig. 2-10 shows the shear-zone-only residence time distributions for each test plotted as a function of volume extracted. There curves were obtained by effectively deconvoluting the conservative tracer injection functions from the conservative

tracer extraction functions in each test. This deconvolution was accomplished by matching the extraction functions using a 1-D advection-dispersion model while assuming that the injection functions were the observed injection concentration histories (or inferred concentration histories in the case of the CRR tests). The curves of Fig. 2-10 were calculated assuming that a 0.02-hr tracer pulse was injected directly into the shear zone, with the normalized concentrations being divided by the extraction flow rate in each test to make the areas under the curves the same. The shear-zone mean residence times and Peclet numbers (transport distance divided by longitudinal dispersivity) deduced for each test and used to generate the curves of Figure 2-10 are listed in Table 2-2. It is clear that the shear-zone transport functions for the two different CFM 13-05 injection functions are significantly different, with their only common feature being the extracted volume at which the peak concentration occurs. These different shear zone transport functions have a big effect on model-deduced transport parameters for the CFM 13-05 test. In this report, the model parameters deduced for both of the CFM 13-05 injection functions are treated as a reflection of parameter uncertainty resulting from uncertainty in knowledge of the true injection function. However, it will be shown later that the varying-rate injection function appeared to be superior to the constant rate injection function because the latter required time-dependent filtration and desorption rate constants to provide good model matches to the breakthrough curves of colloids and several radionuclides in CFM 13-05.

Table 2-2. Deduced mean residence times and Peclet numbers in shear zone for curves of Figure 2-10.

Parameter	CRR 31	CRR 32	CFM 12-02	CFM 13-05 Constant	CFM 13-05 Varying
Mean Residence Time, hr	1.8	1.9	36	28	140
Peclet number	9.5	11.5	10	27	1.5

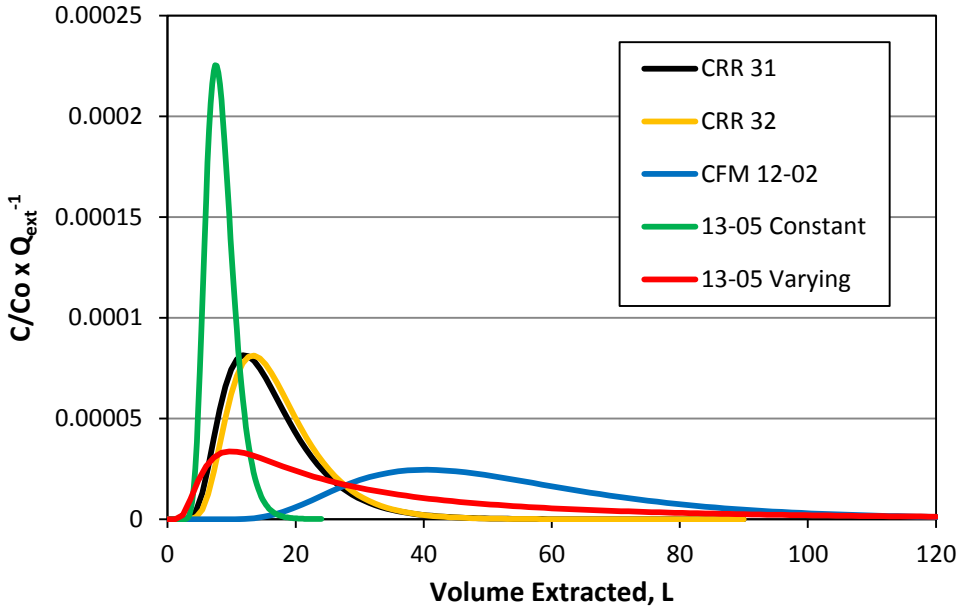

Figure 2-10. Deduced shear-zone-only residence time distributions in each test. For CFM 13-05, "constant" and "varying" refers to constant and varying injection rate functions.

2.3 Interpretive Modeling Approach

The first step in the interpretive modeling procedure was to use the RELAP (REactive transport LAPlace transform) semi-analytical model (Reimus et al., 2003) to approximately fit the conservative tracer extraction breakthrough curves by adjusting the mean residence time and Peclet number in the shear zone (Peclet number is transport distance divided by longitudinal dispersivity) as well as the fractional tracer mass participation in each test. This model was used to generate the shear-zone-only residence time distributions of Fig. 2-10 after the injection functions had been effectively deconvoluted from the extraction functions using the numerical model described below. Exponential-decay injection functions with a constant decay rate (i.e., constant injection flow rate) can be directly implemented in RELAP, but RELAP cannot accommodate varying injection rates, so for the CFM tests, RELAP provided only approximate estimates of the mean residence time and Peclet number to use as first guesses in the numerical model (which was then used to refine the estimates). RELAP was used to do all model interpretations of the CRR tests because these tests involved simple pulse injections that RELAP can readily accommodate.

RELAP is a semi-analytical model that uses a Fourier transform inversion method to solve the Laplace-domain transport equations in either a single- or a dual-porosity system. The model can account for diffusion between fractures and matrix, as well as linear, first-order reactions in both fractures and matrix. The very rapid execution of the model makes it ideal for the numerous simulations needed for transport parameter estimation. The fractional mass participation in each test was allowed to be an adjustable parameter because some of the tests did not have complete tracer recovery, indicating that some of the tracer mass drifted out of the hydraulic capture zone induced by extraction at the BOMI 87.010 borehole (or at the Pinkel surface packer in the case of CFM Run 12-02). A matrix porosity of 0.02 that extended 1 cm into the matrix from the fracture wall(s) was assumed in the shear zone for all test interpretations (the matrix was assumed to have a porosity of zero at distances greater than 1 cm from the fracture walls), and a solute matrix diffusion coefficient of 1×10^{-6} cm^2/sec was also assumed in all interpretations. Also, a shear-zone effective fracture aperture of 2 mm was assumed in all test interpretations, and the effective porosity within the shear zone was assumed to be 0.5 to allow for sorption to occur within the shear zone.

The mean residence time, Peclet number and fractional mass participation estimated for the conservative tracers using the above matrix diffusion parameters were not significantly different from estimates obtained assuming no matrix diffusion. However, matrix diffusion and sorption were found to be necessary to explain the transport behavior of the reactive solutes that were not strongly associated with colloids, so a small amount of matrix diffusion was allowed.

In addition to providing estimates of shear-zone transport parameters for the conservative tracers, RELAP was also used to estimate colloid transport parameters (filtration and resuspension rate constants) and reactive solute transport parameters (fracture and matrix adsorption and desorption rate constants for solutes not strongly associated with colloids, and colloid desorption rate constants for solutes strongly associated with colloids). These estimates were obtained by assuming that the mean residence time, Peclet number and fractional mass participation estimated for the conservative tracers also applied to the colloids and reactive solutes, and then the appropriate rate parameters were adjusted to fit the colloid or solute data.

The resulting best-fitting parameters from RELAP were used as initial parameter estimates in a 2-D numerical model that could account for processes that RELAP does not explicitly account for. The most important of these processes was the variable injection flow rates observed in the CFM tests and the simultaneous transport of colloids and reactive solutes (RELAP does not account for interacting species). In effect, RELAP was used to obtain initial estimates for the more robust numerical model. This procedure was found to be highly effective for refinement of parameter estimates; only relatively minor adjustments to the RELAP-estimated parameters were necessary, and these adjustments could be made rather quickly by hand. The mean residence times and Peclet numbers of the shear zone listed in Table 2-2 were obtained using this refinement procedure. Note that the 2-D model still simulated only 1-D flow, as the second dimension (perpendicular to flow) was used only to account for diffusive mass transport.

The 2-D numerical model simultaneously solves the following equations:

Colloid Transport in Fractures:

Mobile: $$\frac{\partial C_{col}}{\partial t} + v_f \frac{\partial C_{col}}{\partial x} - D_c \frac{\partial^2 C_{col}}{\partial x^2} + k_{fc} C_{col} - k_{rc} S_{col} + k_{fci} C_{col} - P_{col} = 0 \qquad (2\text{-}1)$$

Immobile: $$\frac{\partial S_{col}}{\partial t} - k_{fc} C_{col} + k_{rc} S_{col} - k_{fci} C_{col} = 0 \qquad (2\text{-}2)$$

Solute Transport in Fractures:

$$\frac{\partial C}{\partial t} + v_f \frac{\partial C}{\partial x} - D_f \frac{\partial^2 C}{\partial x^2} + k_{1f} C C_{col} \left(1 - \frac{C_1}{C_{col} S_1^0}\right) + k_{2f} C\, C_{col} \left(1 - \frac{C_2}{C_{col} S_2^0}\right) +$$
$$\left(\frac{\rho_f}{\eta}\right) k_{fa} C \left(1 - \frac{S_a}{S_a^0}\right) + \left(\frac{\rho_f}{\eta}\right) k_{fb} C \left(1 - \frac{S_b}{S_b^0}\right) + k_{1f} C S_{col} \left(1 - \frac{C_{filt,1}}{S_{col} S_1^0}\right) + k_{2f} C S_{col} \left(1 - \frac{C_{filt,2}}{S_{col} S_2^0}\right) - \qquad (2\text{-}3)$$
$$k_{1b} C_1 - k_{2r} C_2 - k_{1b} C_{filt,1} - k_{2r} C_{filt,2} - \left(\frac{\rho_f}{\eta}\right) k_{ra} S_a - \left(\frac{\rho_f}{\eta}\right) k_{rb} S_b - \frac{\phi D_m}{b\eta} \frac{\partial C_m}{\partial y}\bigg|_{y=b} = 0$$

Solute Transport on mobile colloids (in fractures) while adsorbed to colloid sites 1 and 2:

$$\frac{\partial C_1}{\partial t} + v_f \frac{\partial C_1}{\partial x} - D_c \frac{\partial^2 C_1}{\partial x^2} - k_{1f} CC_{col} \left(1 - \frac{C_1}{C_{col} S_1^0}\right) - k_{rc} C_{filt,1} + k_{1r} C_1 + k_{fc} C_1 - P_{col} S_a = 0 \quad (2\text{-}4)$$

$$\frac{\partial C_2}{\partial t} + v_f \frac{\partial C_2}{\partial x} - D_c \frac{\partial^2 C_2}{\partial x^2} - k_{2f} CC_{col} \left(1 - \frac{C_2}{C_{col} S_2^0}\right) - k_{rc} C_{filt,2} + k_{2r} C_2 + k_{fc} C_2 - P_{col} S_b = 0 \quad (2\text{-}5)$$

Solute Transport in Matrix:

$$\frac{\partial C_m}{\partial t} - D_m \frac{\partial^2 C_m}{\partial y^2} + \left(\frac{\rho_b}{\phi}\right) k_{fam} C_m \left(1 - \frac{S_{am}}{S_{am}^0}\right) + \left(\frac{\rho_b}{\phi}\right) k_{fbm} C_m \left(1 - \frac{S_{bm}}{S_{bm}^0}\right) - \left(\frac{\rho_b}{\phi}\right) k_{ram} S_{am} - \left(\frac{\rho_b}{\phi}\right) k_{rbm} S_{bm} = 0 \quad (2\text{-}6)$$

Immobile Solute in Fractures (sorption sites a and b):

$$\frac{\partial S_a}{\partial t} - k_{fa} C \left(1 - \frac{S_a}{S_a^0}\right) + k_{ra} S_a = 0 \quad (2\text{-}7)$$

$$\frac{\partial S_b}{\partial t} - k_{fb} C \left(1 - \frac{S_b}{S_b^0}\right) + k_{rb} S_b = 0 \quad (2\text{-}8)$$

Immobile Solute in Matrix (sorption sites a_m and b_m):

$$\frac{\partial S_{am}}{\partial t} - k_{fam} C \left(1 - \frac{S_{am}}{S_{am}^0}\right) + k_{ram} S_{am} = 0 \quad (2\text{-}9)$$

$$\frac{\partial S_{bm}}{\partial t} - k_{fbm} C \left(1 - \frac{S_{bm}}{S_{bm}^0}\right) + k_{rbm} S_{bm} = 0 \quad (2\text{-}10)$$

Immobile Solute adorbed onto Immobile Colloids in Fractures (colloid sites 1 and 2):

$$\frac{\partial C_{filt,1}}{\partial t} - k_{1f} C S_{col}\left(1-\frac{C_{filt,1}}{S_{col}S_1^0}\right) - (k_{fc}+k_{fci})C_1 + k_{rc}C_{filt,1} + k_{1r}C_{filt,1} = 0 \quad (2\text{-}11)$$

$$\frac{\partial C_{filt,2}}{\partial t} - k_{2f} C S_{col}\left(1-\frac{C_{filt,2}}{S_{col}S_2^0}\right) - (k_{fc}+k_{fci})C_2 + k_{rc}C_{filt,2} + k_{2r}C_{filt,2} = 0 \quad (2\text{-}12)$$

where, C_{col} = concentration of colloids in solute phase, g/cm^3
S_{col} = colloid concentration on fracture surfaces, g/cm^3
C = solution concentration of solute in fractures, g/cm^3
C_m = solution concentration of solute in matrix, g/cm^3
S_a = sorbed concentration of solute on fracture surface site *a*, g/g
S_b = sorbed concentration of solute on fracture surface site *b*, g/g
C_1 = concentration of solute sorbed to site 1 on mobile colloids, g/cm^3
C_2 = concentration of solute sorbed to site 2 on mobile colloids, g/cm^3
$C_{filt,1}$ = concentration of solute sorbed to site 1 on immobile colloids, g/cm^3
$C_{filt,2}$ = concentration of Pu on sorbed to site 2 on immobile colloids, g/cm^3
S_{am} = sorbed concentration of solute on matrix surface site a_m, g/g
S_{bm} = sorbed concentration of solute on fracture surface site b_m, g/g
P_{col} = colloid production rate in fractures, g/cm^3-s
v_f = fluid velocity in fractures, cm/s
D_f = solute dispersion coefficient in fractures, cm^2/s
D_c = colloid dispersion coefficient in fractures, cm^2/s
D_m = solute molecular diffusion coefficient in matrix, cm^2/s
ρ_f = effective bulk density within fractures, g/cm^3
ρ_B = bulk density in matrix, g/cm^3.
η = porosity within fractures
ϕ = matrix porosity
b = fracture half aperture, cm
k_{fc} = colloid filtration rate constant (1/s) = λv_f, where λ = filtration coefficient (1/cm)
k_{rc} = reverse colloid filtration (detachment) rate constant, 1/s.
k_{fci} = irreversible colloid filtration rate constant, 1/s
k_{fa} = rate constant for sorption of solute onto fracture surface site *a*, ml/g-s
k_{ra} = rate constant for desorption of solute from fracture surface site *a*, 1/s
k_{fb} = rate constant for sorption of solute onto fracture surface site *b*, ml/g-s
k_{rb} = rate constant for desorption of solute from fracture surface site *b*, 1/s
k_{fam} = rate constant for sorption of solute onto matrix surface site a_m, ml/g-s
k_{ram} = rate constant for desorption of solute from matrix surface site a_m, 1/s
k_{fbm} = rate constant for sorption of solute onto matrix surface site b_m, ml/g-s
k_{rbm} = rate constant for desorption of solute from matrix surface site b_m, 1/s
k_{1f} = rate constant for sorption of solute onto colloid surface site 1, ml/g-s
k_{1r} = rate constant for desorption of solute from colloid surface site 1, 1/s
k_{2f} = rate constant for sorption of solute onto colloid surface site 2, ml/g-s
k_{2r} = rate constant for desorption of solute from colloid surface site 2, 1/s

S_1^0 = maximum solute capacity on colloid sorption site 1, g/g colloid
S_2^0 = maximum solute capacity on colloid sorption site 2, g/g colloid
S_a^0 = maximum solute capacity on fracture sorption site *a*, g/g solid
S_b^0 = maximum solute capacity on fracture sorption site *b*, g/g solid
S_{am}^0 = maximum solute capacity on matrix sorption site a_m, g/g solid
S_{bm}^0 = maximum solute capacity on matrix sorption site b_m, g/g solid

Figure 2-11 shows the system geometry and boundary conditions assumed in the numerical model. The parallel-plate fracture domain is one node wide, implying that concentration gradients across the fracture aperture are rapidly leveled by diffusion and/or advective mixing. Solute diffusion between fractures and matrix is assumed to be perpendicular to the fracture flow direction. The matrix nodes can be specified to have variable spacing with different porosities and different solute diffusion coefficients as a function of distance away from the fracture wall. Thus, fracture coatings or gradients in porosity or diffusion coefficients can be simulated. The above equations and the geometry of Figure 2-11 also apply to RELAP, although simplifications are necessary to use the RELAP semi-analytical solution method (Reimus et al., 2003).

The reaction processes accounted for by equations 2-1 to 2-12 are depicted in Figure 2-12 (including diffusion between the fractures and matrix). Solutes can adsorb to and desorb from two different sorption sites that are assumed to be present on (1) fracture surfaces, (2) matrix surfaces, (3) mobile colloid surfaces, and (4) immobile colloid surfaces. The adsorption sites on each surface can be specified as being irreversible by simply specifying a zero desorption rate constant for that site. Colloids can attach either reversibly or irreversibly to fracture surfaces, but they are not allowed to diffuse into the matrix. When the colloids attach or detach, they carry any adsorbed solutes with them, although the solutes can still independently adsorb or desorb from colloids after the colloid transition. Additionally, colloid generation from fracture surfaces is allowed. The model ensures that a background colloid concentration given by P_{col}/k_{fci} is always maintained in the system, satisfying the steady-state condition that the colloid production rate must be balanced by an irreversible filtration rate (if this were not true either all colloids would disappear from the system or the system would plug with colloids). Each arrowhead in Figure 2-12 has a reaction rate that can be specified by the user (or a diffusion coefficient in the case of diffusion into/from the matrix).

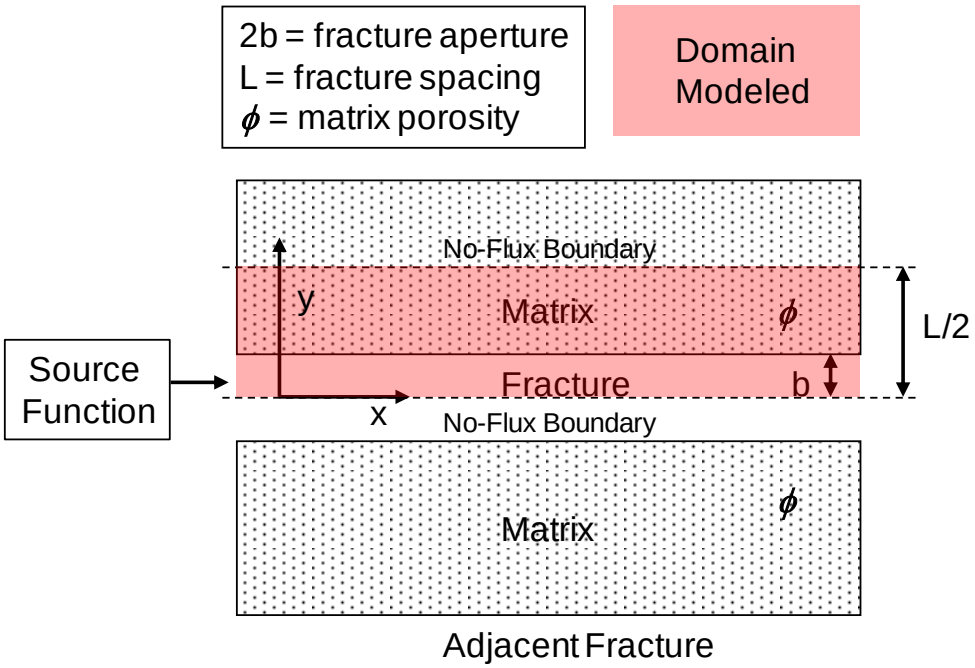

Figure 2-11. System geometry and boundary conditions assumed in the numerical model (also applies to the RELAP model).

With a few exceptions, the red-outlined boxes in Figure 2-12 were the only ones that were actually used to model the colloid and solute data from the colloid-radionuclide tracer tests. Specifically, only a single type of sorption site was assumed to be present on each of the surfaces present in the system (although the fracture, matrix, and colloid sites were allowed to have different adsorption and desorption rates). It was found that reasonable fits to the tracer data could be obtained without the black-outlined boxes, and it was considered desirable to not complicate the model with additional processes and parameters that did not significantly improve the fits.

2.4 Test Interpretations

The RELAP model matches to the radionuclide and colloid breakthrough curves for CRR Runs 31 and 32 are shown in Fig. 2-13 to 2-18. Each figure shows model results for multiple radionuclides or colloids. Figs. 2-19 and 2-20 show the results of numerical model matches to the AGA, radionuclides and colloids in CFM Run 12-02 (these were previously reported in Chapter 2 of Wang et al., 2013, although they are updated here). Finally, Fig. 2-21 shows the AGA and colloid model matches for CFM Run 13-05, and Figs. 2-22 through 2-28 show each individual radionuclide model match for CFM 13-05 along with the AGA data and the colloid model curves for comparison. For each of the CFM Run 13-05 figures, a pair of plots is shown: one for the constant-rate injection function and one for the varying-rate injection function. The best-fitting model parameters in each of the tests are listed by colloids or radionuclide in Tables 2-3 through 2-5. Table 2-3 lists the filtration rate constants for the colloids in each of the tests (note that a single irreversible filtration rate constant was used for all the tests, as the model matches to the colloid

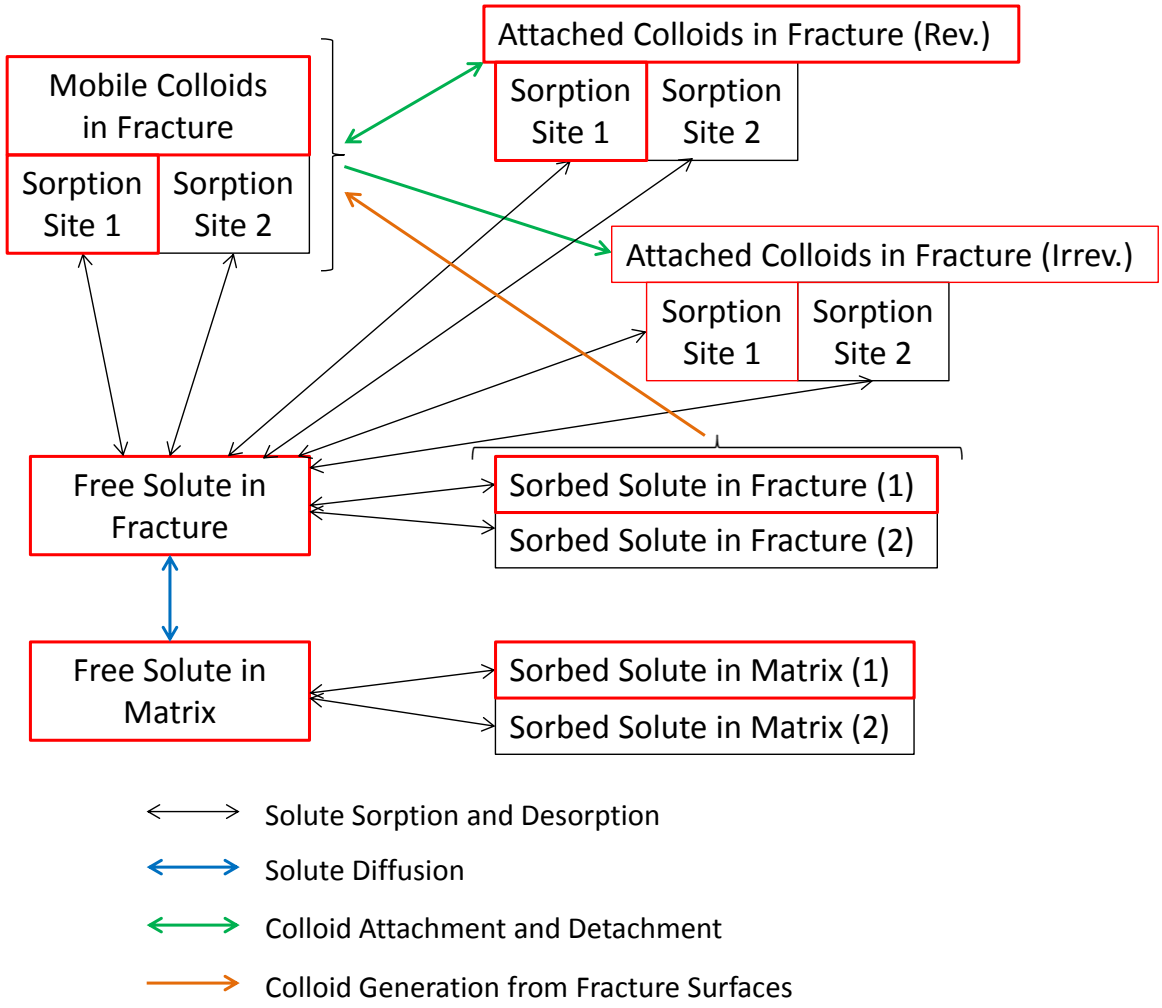

Figure 2-12. Reaction processes accounted for by equations 2-1 to 2-12 and implemented in the numerical transport model. Note that the red-outlined boxes were the only boxes actually used in the interpretation of the colloid-homologue or colloid-radionuclide tracer tests.

breakthrough curves were not significantly improved by assuming a reversible filtration reaction). Table 2-4 lists model parameters for the radionuclides that tended to be less strongly associated with colloids (although Cs was quite strongly associated with colloids in the CFM runs), and Table 2-5 lists the parameters for the actinides Th, Am and Pu, which tended to be quite strongly associated with colloids in all tests. In each table, two sets of parameters are listed for CFM Run 13-05; one assuming the constant-rate injection function, and another assuming the varying-rate injection function.

An underlying strategy in the test interpretations was to try to match the breakthrough curves for a given radionuclide using, to the extent possible, the same model parameters in each test in which the radionuclide was injected. The rationale for this was that the tests were all conducted in the same shear zone within a relatively short distance of each other, so the radionuclide transport parameters should be very similar in the different tests. A little more flexibility was allowed in the case of the parameter estimates for CFM Run 12-02 because this test was conducted in a different portion of the shear zone than all the other tests, which were performed in the same dipole (CRR 99.002 to BOMI 87.010). Because some of the model parameters

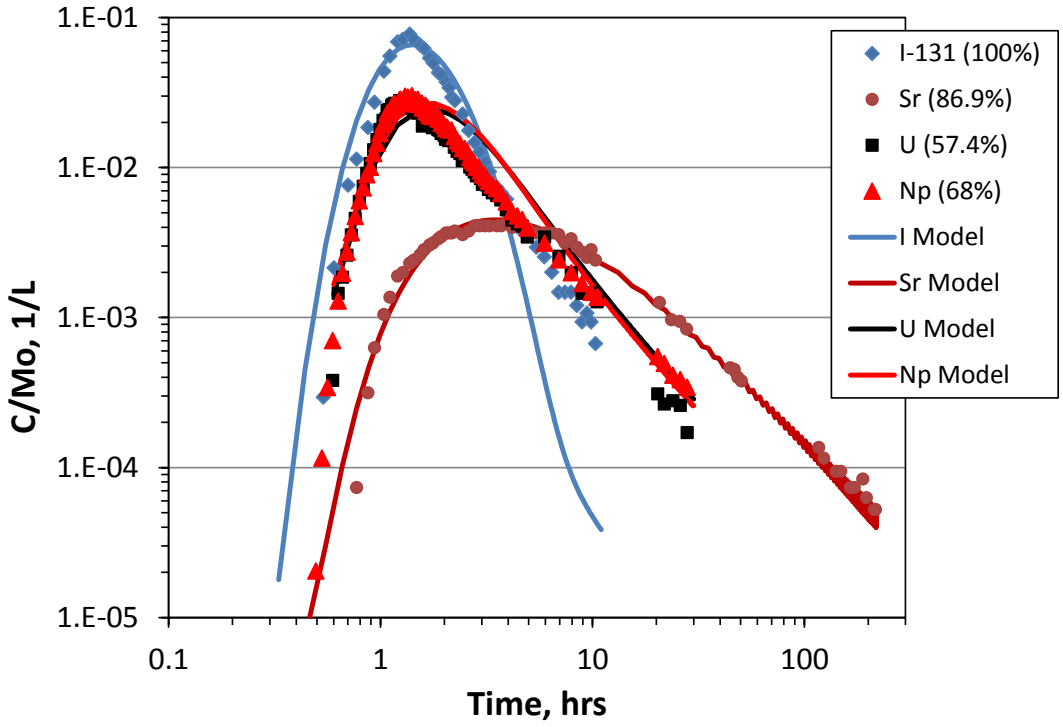

Figure 2-13. Model matches to ^{131}I, Sr, U, and Np data from CRR Run 31.

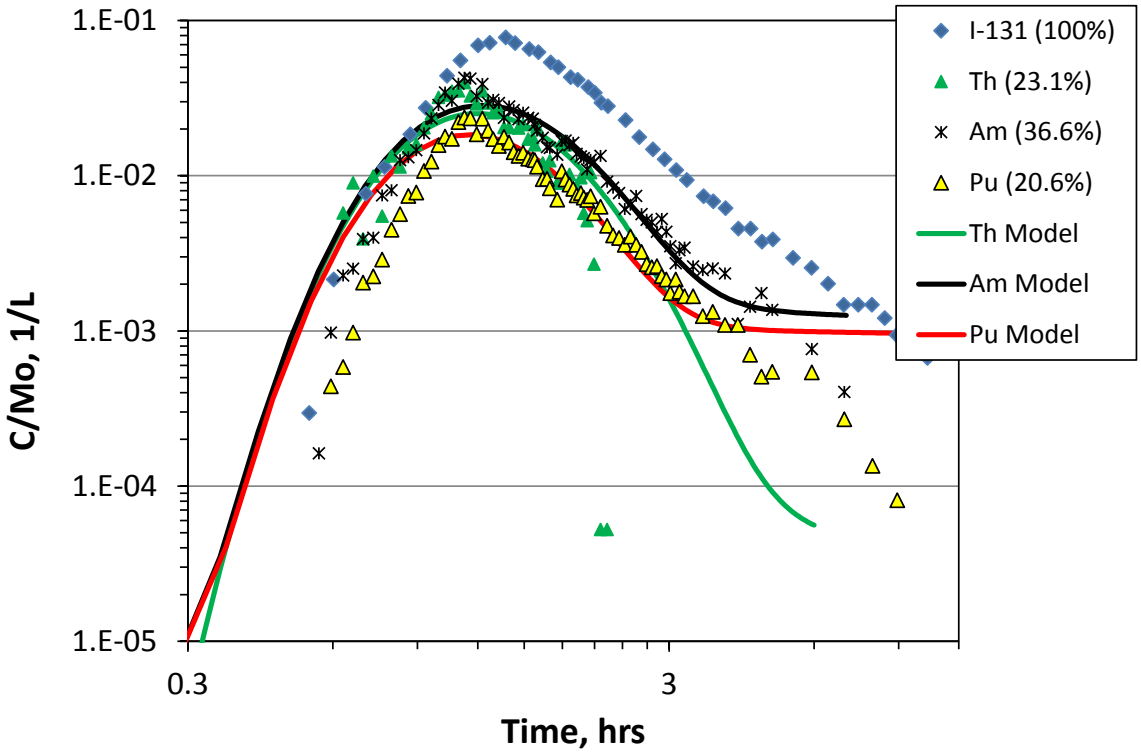

Figure 2-14. Model matches to Th, Am, and Pu data from CRR Run 31.

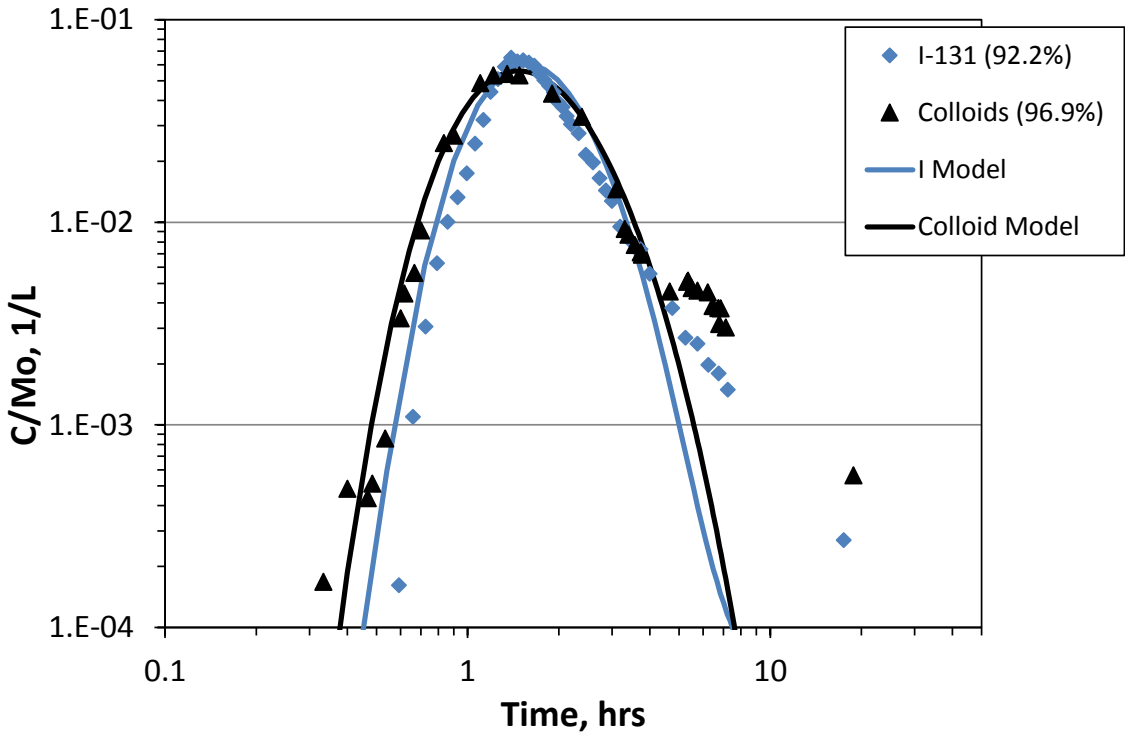

Figure 2-15. Model matches to ^{131}I and colloid data from CRR Run 32.

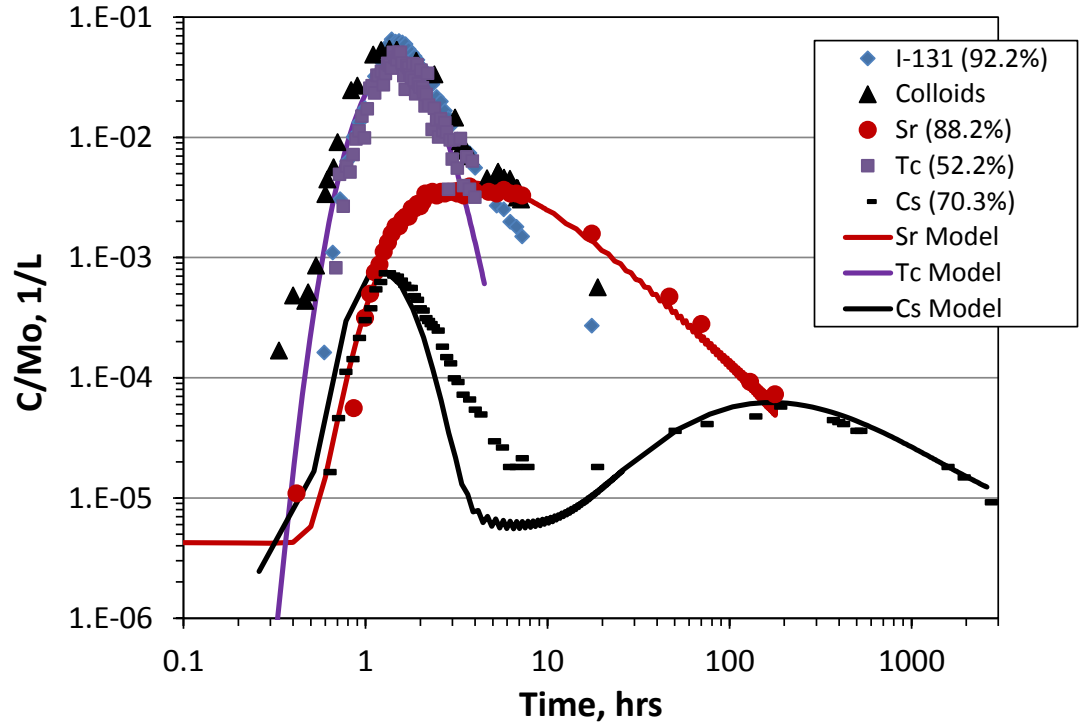

Figure 2-16. Model matches to ^{131}I, Sr, Tc,and Cs data from CRR Run 32. Sr and Tc modeled as solute transport. Cs early peak modeled as colloid-facilitated transport and late peak modeled as solute transport.

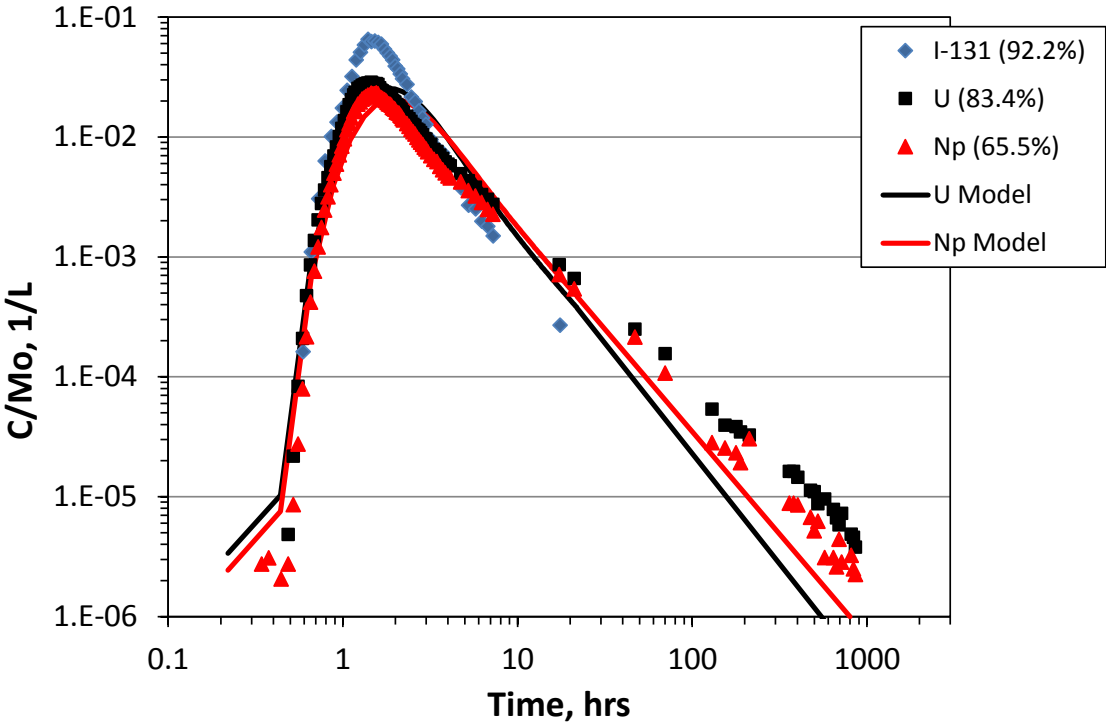

Figure 2-17. Model matches to U and Np data from CRR Run 32. Both species modeled as being dominated by solute transport (not colloid-facilitated transport).

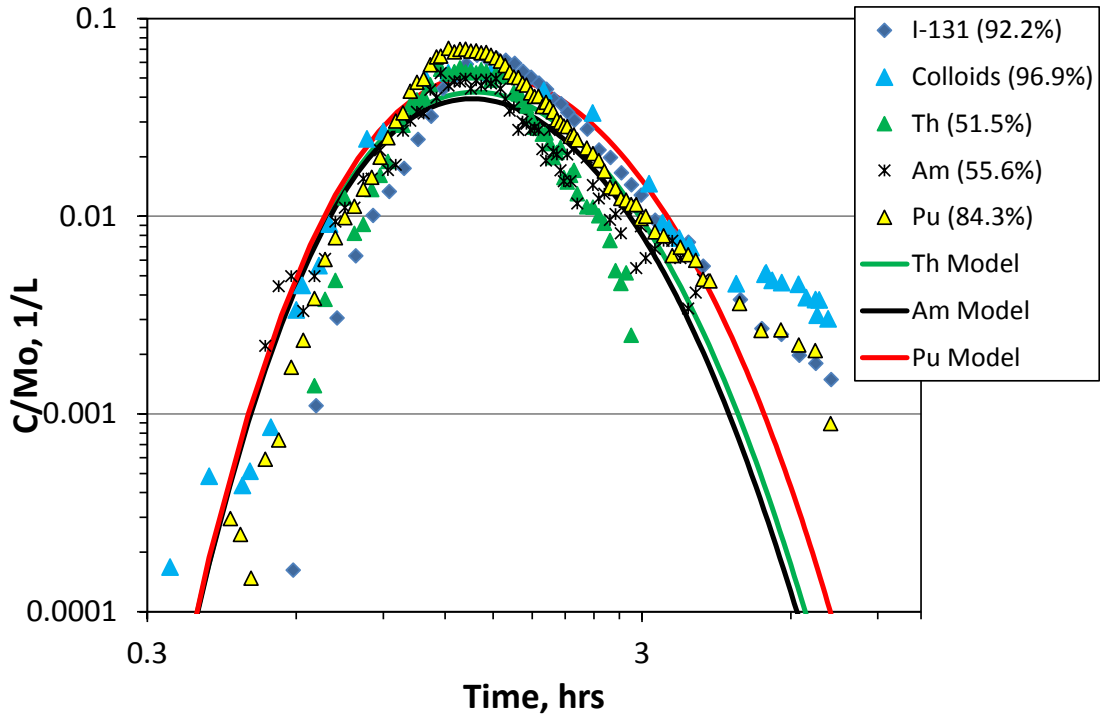

Figure 2-18. Model matches to Th, Am and Pu data from CRR Run 32. All species modeled as dominated by colloid-facilitated transport.

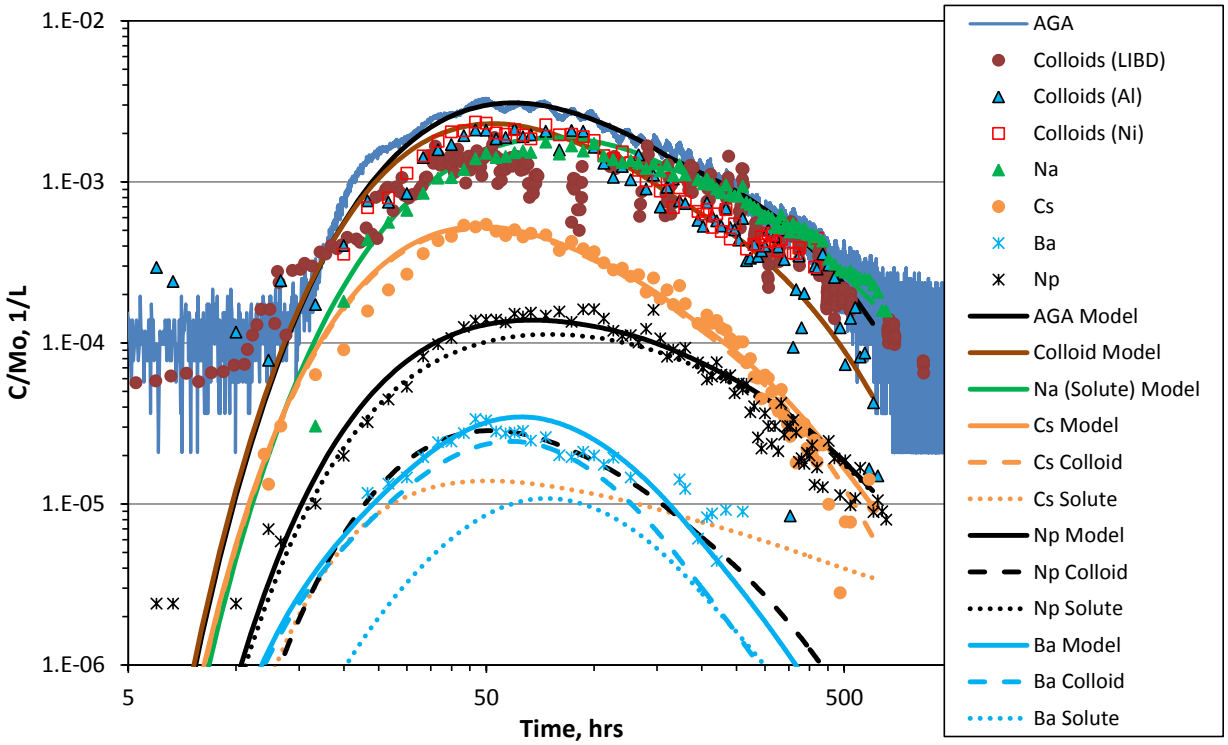

Figure 2-19. Model matches to the AGA, colloid, Na, Cs, Ba and Np breakthrough curves of CFM Run 12-02. Modeled solute and colloid contributions shown.

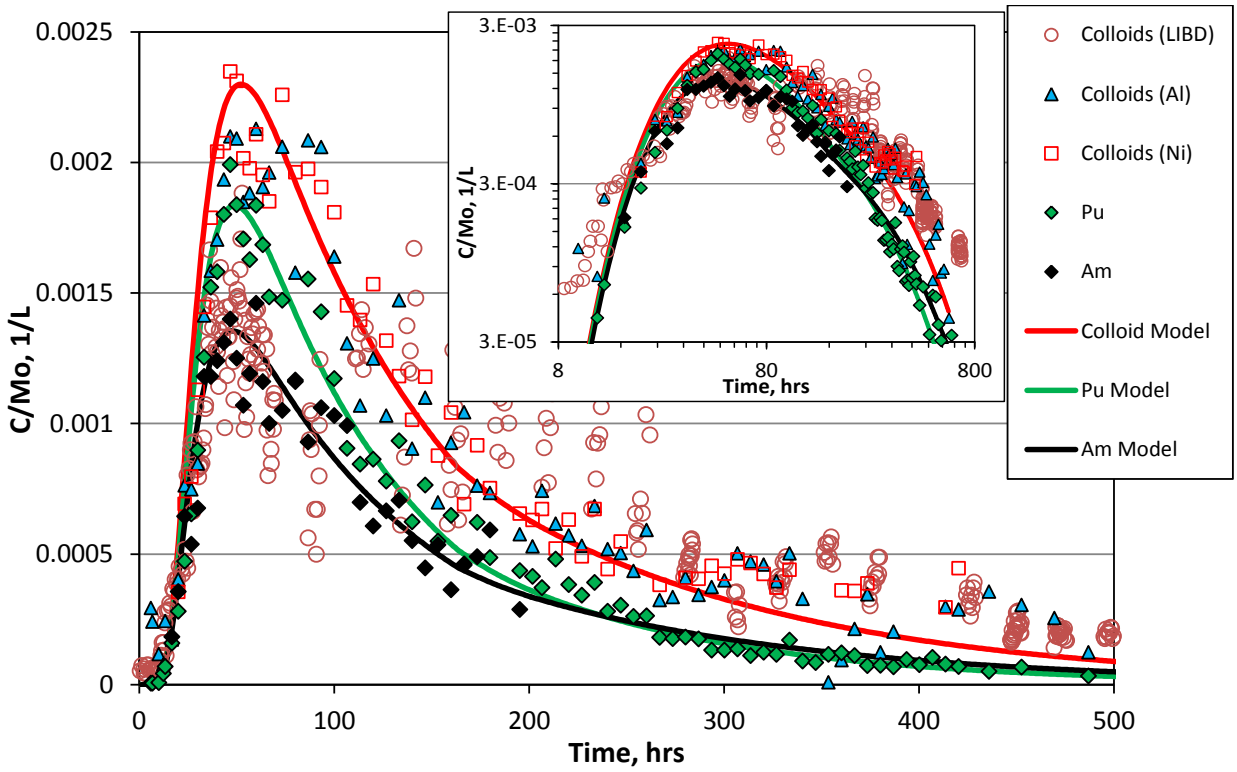

Figure 2-20. Model matches to the colloid, Pu, and Am breakthrough curves of CFM Run 12-02. Both species modeled as colloid-facilitated transport.

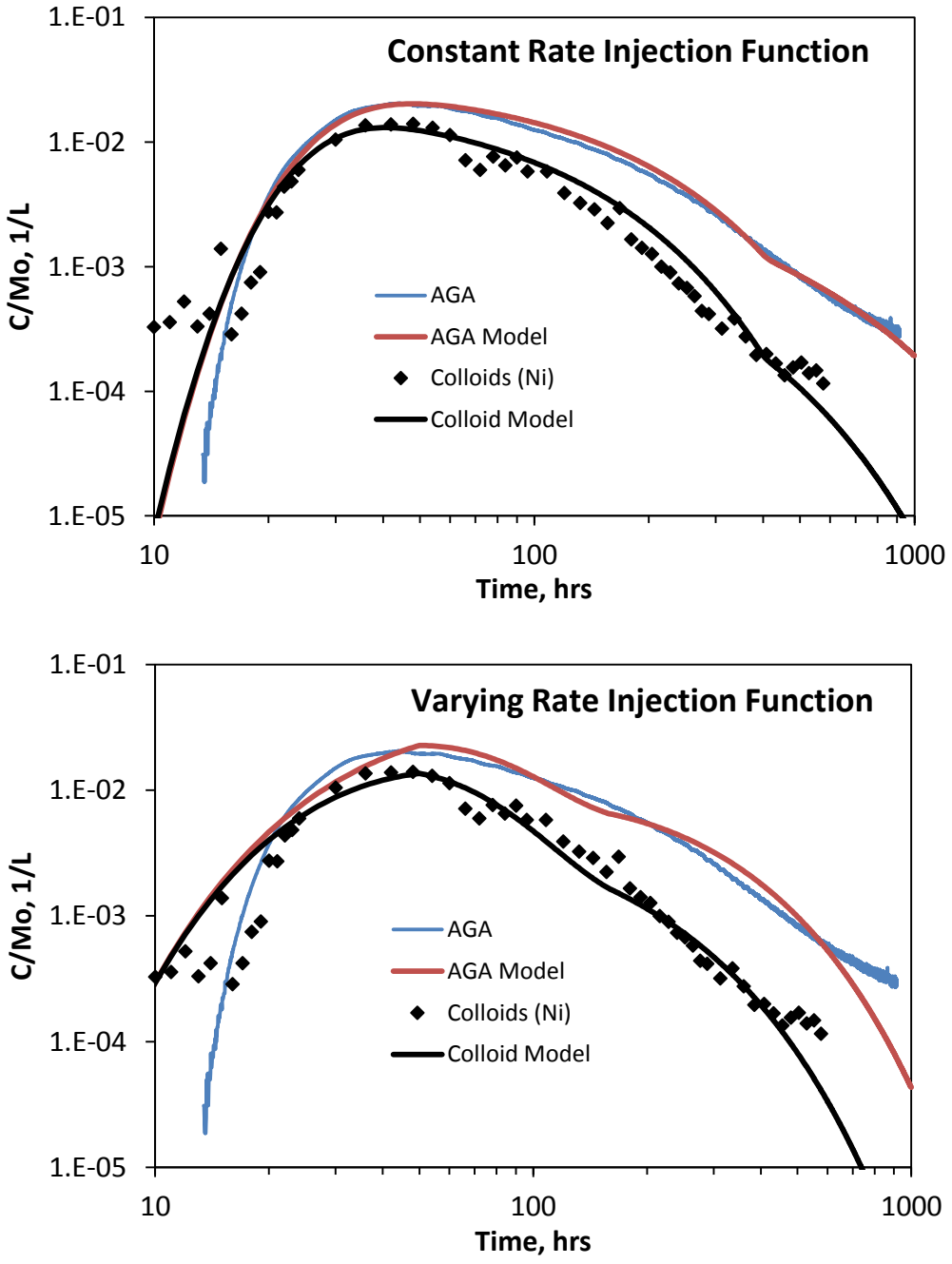

Figure 2-21. Model matches to the AGA and colloid breakthrough curves of CFM Run 13-05 assuming the two different injection functions.

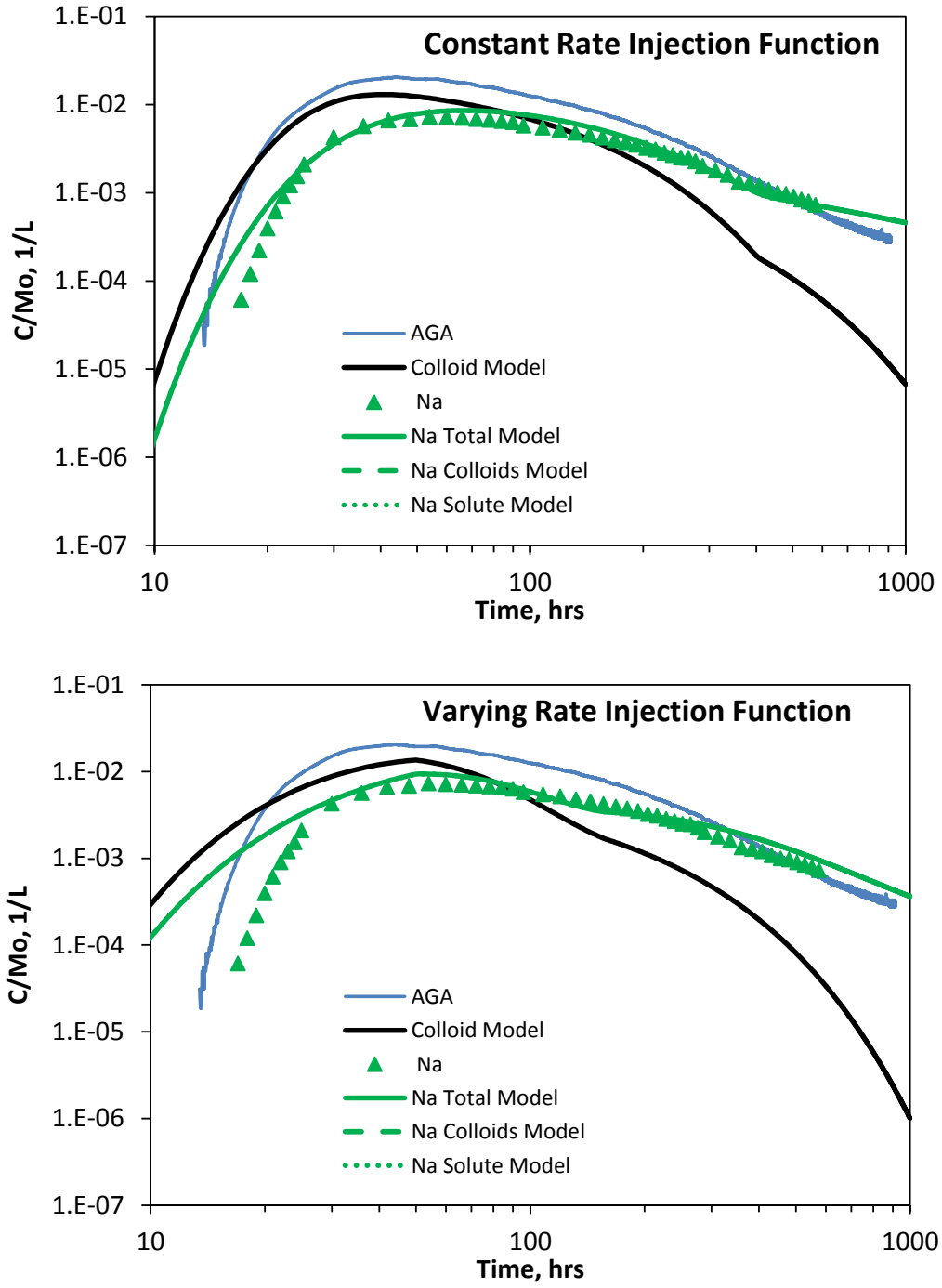

Figure 2-22. Model matches to the Na breakthrough curve of CFM Run 13-05 assuming the two different injection functions. Modeled solute and colloid contributions are shown (note that colloid contribution for varying rate injection function is negligible.

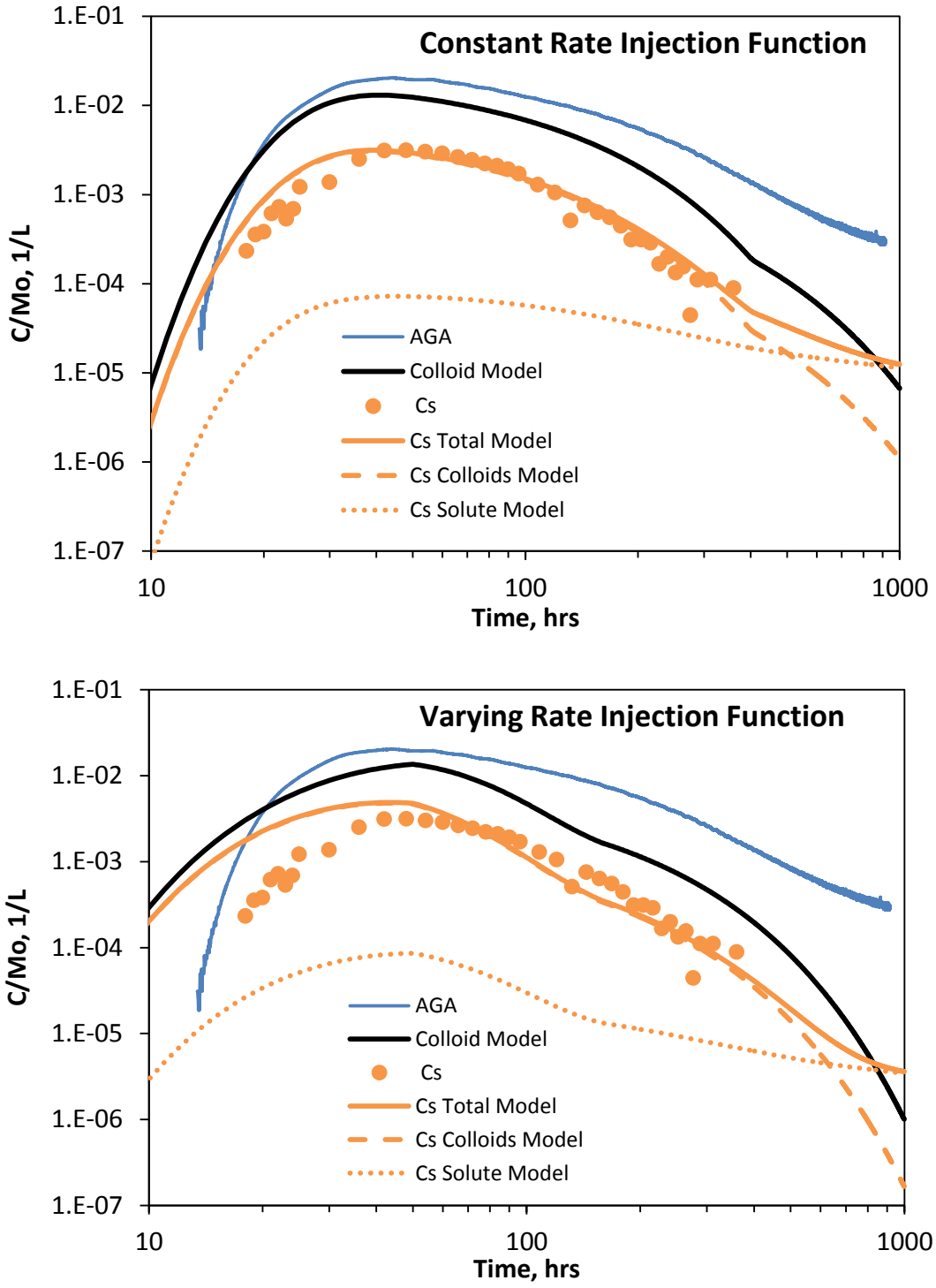

Figure 2-23. Model matches to the Cs breakthrough curve of CFM Run 13-05 assuming the two different injection functions. Modeled solute and colloid contributions are shown.

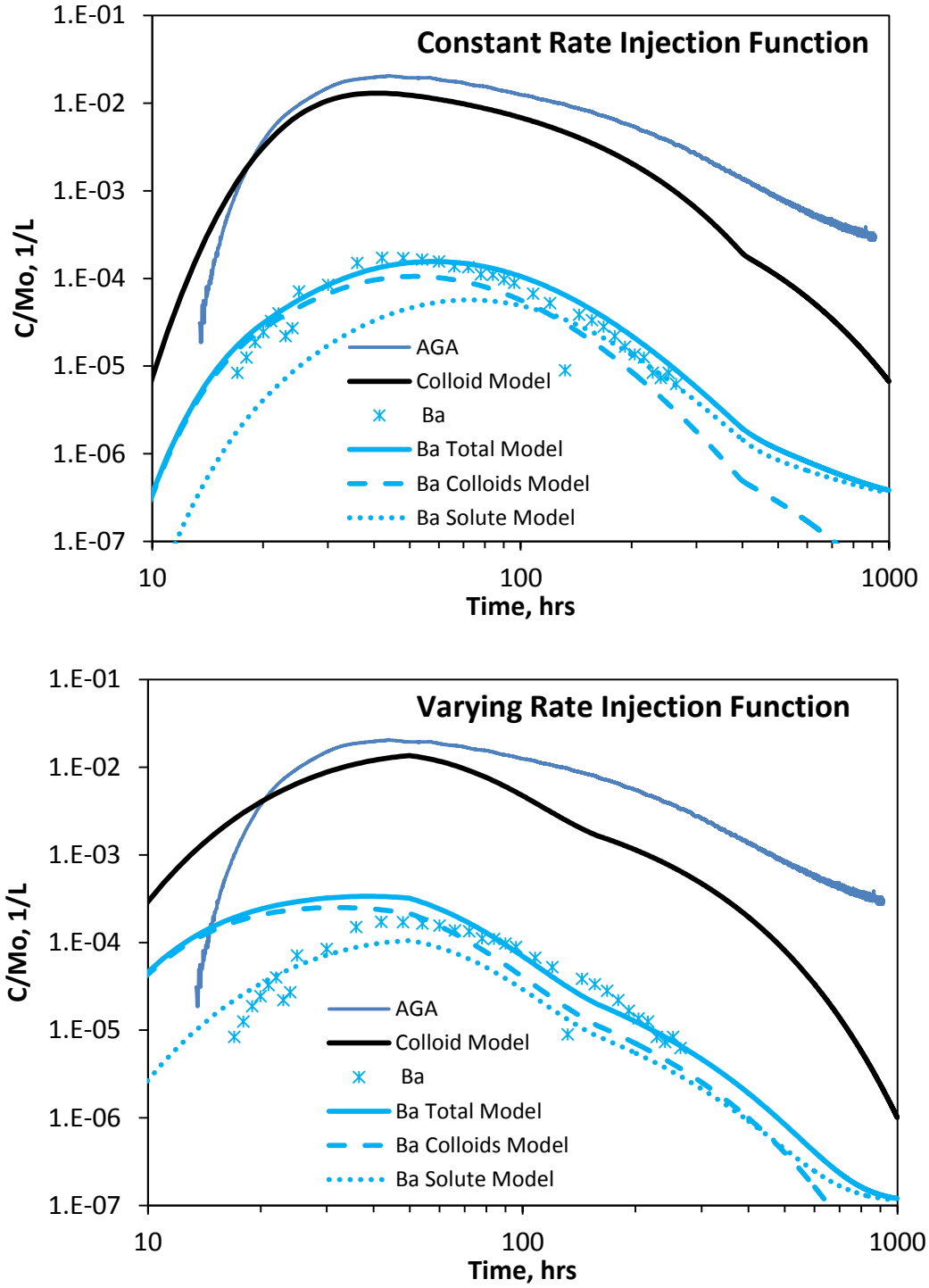

Figure 2-24. Model matches to the Ba breakthrough curve of CFM Run 13-05 assuming the two different injection functions. Modeled solute and colloid contributions are shown.

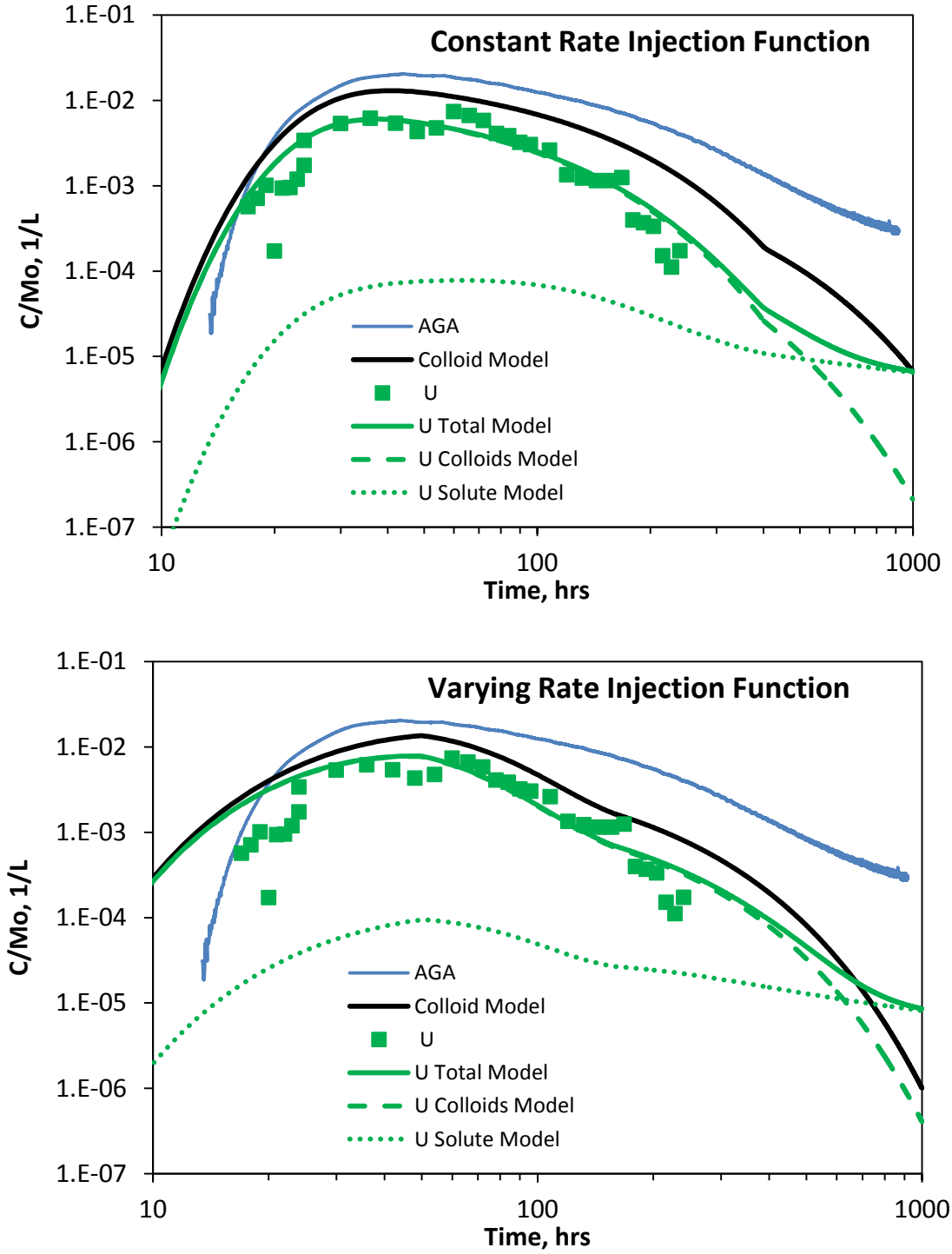

Figure 2-25. Model matches to the U breakthrough curve of CFM Run 13-05 assuming the two different injection functions. Modeled solute and colloid contributions are shown.

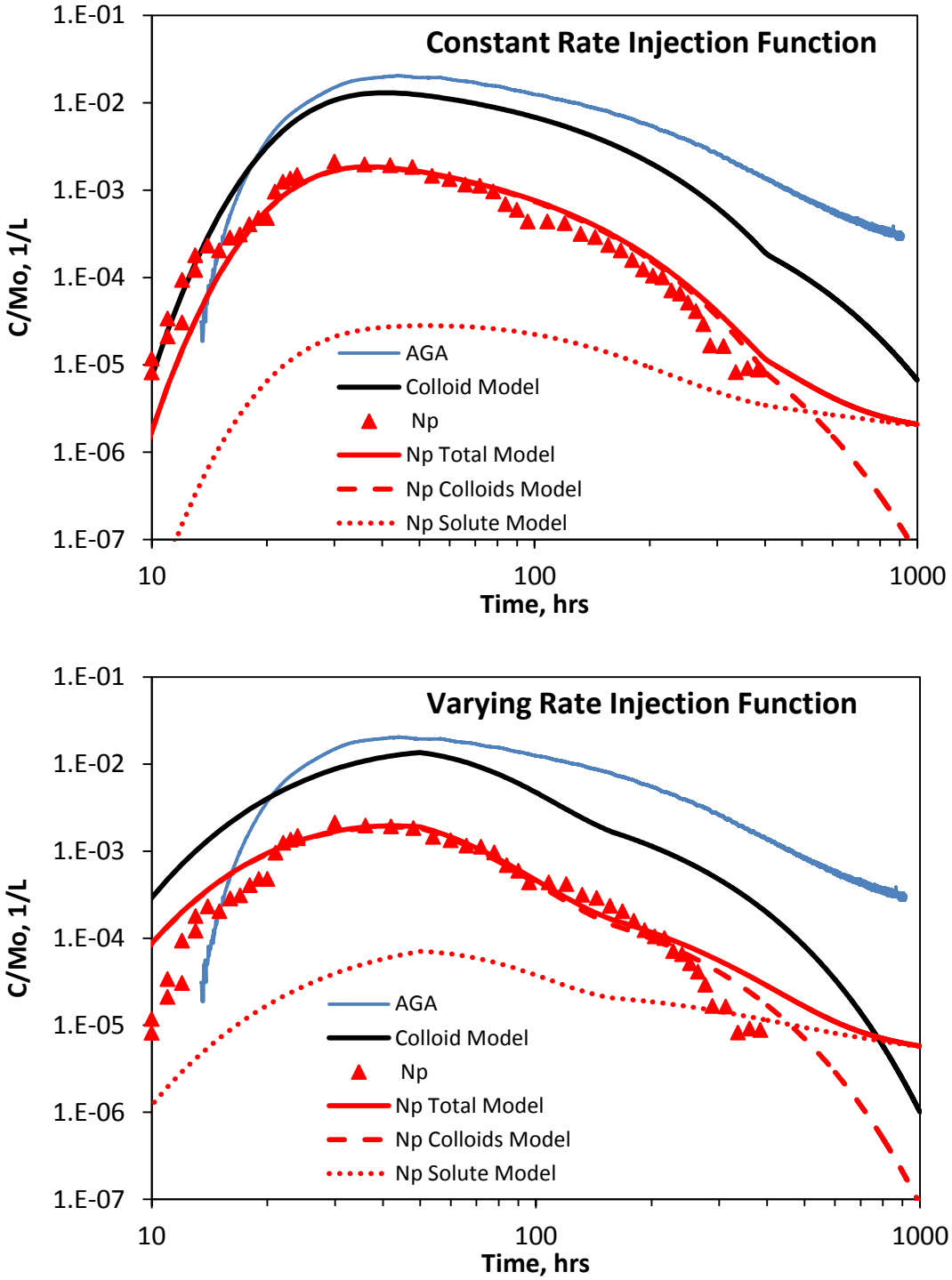

Figure 2-26. Model matches to the Np breakthrough curve of CFM Run 13-05 assuming the two different injection functions. Modeled solute and colloid contributions are shown.

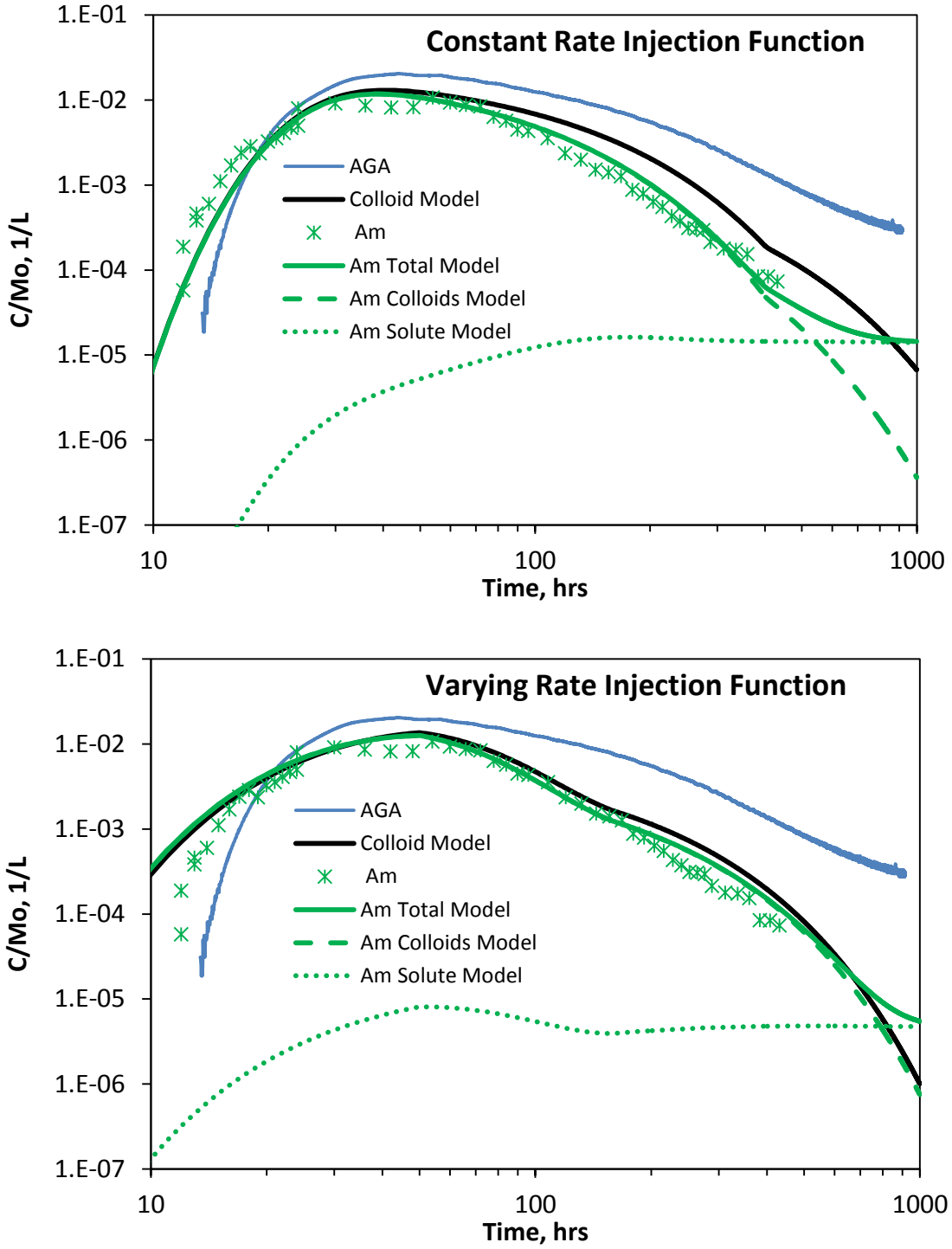

Figure 2-27. Model matches to the Am breakthrough curve of CFM Run 13-05 assuming the two different injection functions. Modeled solute and colloid contributions are shown.

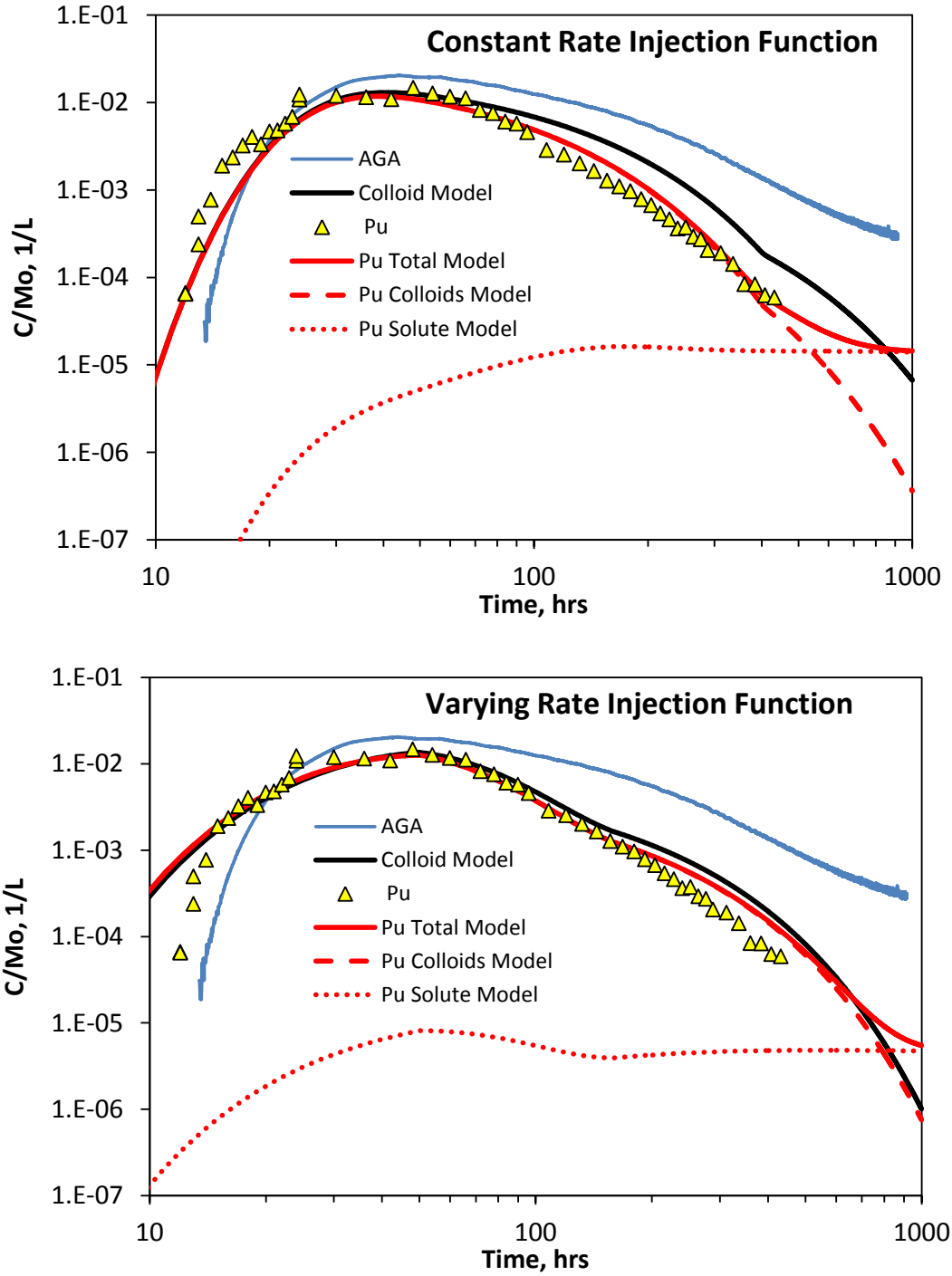

Figure 2-28. Model matches to the Pu breakthrough curve of CFM Run 13-05 assuming the two different injection functions. Modeled solute and colloid contributions are shown.

Table 2-3. Apparent colloid filtration rate constants in all tests (no colloids in CRR Run 31).

Test	k_{fci}^{*}, ml/g-hr
CRR 32	0.0
CFM 12-02	0.013
CFM 13-05 (constant)	0.017-0.12**
CFM 13-05 (varying)	0.02

*k_{fci} = irreversible filtration rate constant; note that it was not necessary to invoke a reversible filtration reaction to match the colloid data in any of the tests.

**In the CFM Run 13-05 with a constant injection rate function, it was necessary to increase the filtration rate constant in linear fashion from 0.017 ml/g-hr at the beginning of the test to 0.12 ml/g-hr at the end of the test to match the colloid data. A single filtration rate constant provided a poor match to the data. The filtration rate constant over the first 200 hours of the test, when most of mass was recovered, was 0.017 to 0.0194 ml/g-hr.

were rather poorly constrained in any given test, this strategy helped reduce the nonuniqueness of the parameter estimates to a greater degree than any single test could.

For each radionuclide in each test, the model matches to the breakthrough curves were generally found to be most sensitive to one or two model parameters, with a relatively high degree of insensitivity to all other model parameters. The most sensitive parameters are listed in red text in Tables 2-4 and 2-5. For the radionuclides that were strongly associated with colloids, the most sensitive parameter was generally the rate constant for radionuclide desorption from colloids. For radionuclides that transported mostly in the solute state, the ratio of adsorption to desorption rate constants in the matrix (after diffusion out of the shear zone) was typically the most sensitive parameter, or more specifically, lumped parameter. However, in CRR Run 31, which had no injected colloids, the radionuclides that were generally strongly associated with colloids transported either as if they strongly interacted with shear zone surfaces or as if they transported as intrinsic colloids that were filtered. The results from all the tests are discussed in the rest of this section by colloids or radionuclide.

2.4.1 Colloids

It is apparent from visual inspection of Fig. 2-15 that the bentonite colloids transported effectively without any filtration in CRR Run 32, so a filtration rate constant of zero is listed in Table 2-3 for this test. The colloid recovery was slightly greater than the ^{131}I recovery in this test, which supports a zero filtration rate constant. However, when the filtration rate constants deduced for the CFM tests were used to model the colloid transport in CRR Run 32, only a few percent of the colloids were predicted to be filtered, and the model match to the data was essentially no different than the match with a filtration rate constant of zero. Thus, apparent lack of colloid filtration in CRR Run 32 could be considered consistent with the observations in the CFM tests.

For CRR Run 32, a slightly different mean residence time and Peclet number were used for the colloids than for the ^{131}I when interpreting this test (2 hrs and 8, respectively, for colloids vs. 1.8 hrs and 9.5 for ^{131}I) to achieve a better match to the colloid data. This approach was considered reasonable given that the

Table 2-4. Adorption and desorption rate constants in the shear zone, on matrix surfaces and on colloids for reactive radionuclides that are not strongly associated (or variably associated) with colloids in different tests. Red numbers indicate parameters that model matches were most sensitive to.

	Shear Zone	Matrix	Colloids	
Test/Radionuclide*	**k_{fa} (ml/g-hr), k_{ra} (1/hr)**	**k_{fam} (ml/g-hr), k_{ram} (1/hr)**	**k_{1f} (ml/g-hr), k_{1r} (1/hr)**
^{22}Na / 12-02	0, 0	1, 3.76	0.1, 1
^{22}Na / 13-05(C)	0, 0	1, 2	0.1, 1
^{22}Na / 13-05(V)	0, 0	1, 2.7	0.1, 1
^{85}Sr / CRR 31	0, 0	2000, 5.1	N/A
^{85}Sr / CRR 32	0, 0	2000, 5.9	0, 0
^{99}Tc / CRR 32**	0.11, 0.0003	0, 0	10, 0.3
^{133}Ba / 12-02	3, 1	5, 0.00005	5000, 0.28
^{133}Ba / 13-05(C)	3, 1	5, 0.00005	5000, 0.28
^{133}Ba / 13-05(V)	3, 1	5, 0.00005	5000, 0.2
^{137}Cs / CRR 32	0, 0	100000, 3.5	5000, 1.6
^{137}Cs / 12-02	0, 0	100000, 3.5	30000, 0.1
^{137}Cs / 13-05(C)	0, 0	100000, 3.5	30000, 0.075
^{137}Cs / 13-05(V)	0, 0	100000, 3.5	30000, 0.04
U / CRR 31	0, 0	100, 3.2	N/A
U / CRR 32	0, 0	100, 5.0	0.1, 10
U / 13-05(C)	0, 0	100000, 1	30, 0.02-0.15***
U / 13-05(V)	0, 0	10000, 1	30, 0.02
^{237}Np / CRR 31	0, 0	100, 4.1	N/A
^{237}Np / CRR 32	0, 0	100, 3.1	0.1, 10
^{237}Np / 12-02	0.041, 0.00001	40, 40	30, 0.035
^{237}Np / 13-05(C)	0.041, 0.00001	100000, 1	30, 0.028-0.15***
^{237}Np / 13-05(V)	0.041, 0.00001	1000, 1	30, 0.035

*(C) refers to constant-rate injection function and (V) refers to varying rate injection function for CFM Run 13-05.

**For ^{99}Tc, the breakthrough curve could be matched equally well assuming either a slow, nearly irreversible sorption reaction in the shear zone, or by assuming the ^{99}Tc was initially associated with colloids and desorbed from colloids with a rate constant of 0.3 hr^{-1}.

***First number is initial desorption rate constant from colloids and second number is final desorption rate constant. When the constant-rate injection function was assumed for CFM Run 13-05, the desorption rate constants had to be varied linearly with time between these two values from beginning of test to end of test to achieve good model matches to the data.

Table 2-5. Sorption and desorption rate constants in the shear zone, on matrix surfaces and on colloids for Th, Am, and Pu (radionuclides strongly associated with colloids) in the different tests. Red numbers indicate parameters that model matches were most sensitive to.

	Fracture	Matrix	Colloids	
Test/Radionuclide	**k_{fa} (ml/g-hr), k_{ra} (1/hr)**	**k_{fam} (ml/g-hr), k_{ram} (1/hr)**	**k_{1f} (ml/g-hr), k_{1r} (1/hr)**	
Th / CRR 31	0.3, 0.0008	0, 0	N/A	
Th / CRR 32	10, 0.01	10, 0.01	10, 0.23	
Am / CRR 31	0.264, 0.035	0, 0	N/A	
Am / CRR 32	10, 0.01	10, 0.01	10, 0.29	
Am / 12-02	10, 0.01	10, 0.01	10, 0.018	
Am / 13-05(C)	10, 0.01	10, 0.01	30, 0-0.15*	
Am / 13-05(V)	10, 0.01	10, 0.01	30, 0.01	
Pu / CRR 31	0.415, 0.032	0, 0	N/A	
Pu / CRR 32	10, 0.01	10, 0.01	10, 0.07	
Pu / 12-02	10, 0.01	10, 0.01	10, 0.005-0.04 (0.01)*	
Pu / 13-05(C)	10, 0.01	10, 0.01	30, 0-0.15*	
Pu / 13-05(V)	10, 0.01	10, 0.01	30, 0.01	

* First number is initial desorption rate constant from colloids and second number is final desorption rate constant. When the constant-rate injection function was assumed for CFM Run 13-05, the desorption rate constants had to be varied linearly with time between these two values from beginning of test to end of test to achieve good model matches to the data. A time-varying colloid desorption rate constant was also found to improve the match to the Pu breakthrough curve in CFM Run 12-02. The number in parentheses for Pu in CFM Run 12-02 is the best-fitting time-invariant desorption rate constant for this test.

colloids would be expected to have greater dispersion in the shear zone because of their much smaller free-water diffusion coefficient than solutes. The greater expected dispersion for the colloids is consistent with Taylor dispersion theory in laminar flow (Taylor, 1953), particularly for the relatively short residence times of the CRR tests, where colloid diffusion across the width of a flow channel would be limited. This limited diffusion, in principle, will result in some colloids experiencing faster residence times and some experiencing slower residence times than a more diffusive solute would experience (because solutes can rapidly diffuse across all streamlines of different velocity in a flow channel and thus experience more of an average velocity).

The colloid filtration rate constants in CFM Runs 12-02 and 13-05 are in relatively good agreement, with a slightly greater apparent filtration rate in Run 13-05. The uncertainty in the colloid data for these two tests is likely smaller than for CRR Run 32 because the colloid concentrations in the CFM tests were quantified by ICP-MS measurements of Ni, which the bentonite colloids were doped with (Reinholdt et al., 2013). This offered higher precision measurements than the LIBD method used to measure the concentrations of undoped bentonite colloids used in CRR Run 32.

The colloid filtration rate constant for CFM Run 13-05 when assuming a constant-rate injection function is specified in Table 2-3 as a range that starts at 0.017 ml/g-hr at time zero and increases linearly with time to 0.12 ml/g-hr at the end of the test. It was necessary to specify such a time-dependent filtration

rate constant to avoid significant over-prediction of the colloid concentrations at the end of the test. This time dependence intuitively seems implausible, which perhaps serves as an independent indication that the varying-rate injection function (which does not require a time-dependent filtration rate constant) is a more accurate injection function to use for CFM Run 13-05 than the constant-rate injection function. However, it is also possible that a time-dependent filtration rate constant may reflect some filtration of colloids in the injection loop during the test and thus a greater decrease in injected colloid concentrations over time than were assumed in the model.

2.4.2 Sodium-22

^{22}Na was used in both CFM tests, but not in the CRR tests. It transported as though it were not facilitated at all by the bentonite colloids, which was not surprising given that it had very weak association with the colloids in the injection cocktails (Table 2-1). Its breakthrough curves were best matched by assuming rapid but weak and reversible adsorption in the matrix adjacent to the shear zone flow pathways. Assuming sorption in the shear zone flow pathways did not improve the model matches to the breakthrough curves. Also, parameters that assume rapid desorption from colloids of the little bit of ^{22}Na that was initially associated with colloids provide good matches to the data. However, in both tests there is so little ^{22}Na initially associated with colloids that the model matches are quite insensitive to values of the colloid adsorption and desorption rate constants provided the adsorption rate constant is relatively small.

The matrix sorption parameters for ^{22}Na were in relatively good agreement for the two CFM tests, and also for the two different injection functions assumed for CFM Run 13-05 (Table 2-4). In each case, it was the ratio of the adsorption and desorption rate constants in the matrix that dictated the quality of the model matches to the data. Larger rate constants than those listed in Table 2-4 provided equally good matches to the data provided the ratio of the two constants remained the same. Note that this ratio is equivalent to an equilibrium partition coefficient, or K_d value (ml/g), if both rates are fast relative to transport rates through the shear zone. In this case, the estimates of the ^{22}Na K_d values ranged from about 0.25 to 0.5 ml/g when the matrix adjacent to the shear zone was assumed to have a porosity of 0.02, the half-aperture of the shear zone was assumed to be 1 mm, and the matrix diffusion coefficient for ^{22}Na was assumed to be 1×10^{-6} cm^2/sec. The deduced K_d values should not be considered well-constrained estimates because they are highly dependent on the assumptions made for the matrix porosity, matrix diffusion coefficient and shear zone aperture in the system, which are not well known. The estimated K_d value is approximately inversely proportional to the assumed matrix diffusion coefficient and the square of the assumed matrix porosity, and approximately directly proportional to the square of the assumed aperture.

It was found that if the ^{22}Na matrix sorption-desorption rate constants were much smaller than those of Table 2-4, the matches to the breakthrough curves became worse even if the ratio of the rate constants was preserved because too much of the ^{22}Na was then predicted to move through the shear zone without interacting with the matrix, and the ^{22}Na concentrations thus became over-predicted.

Inspection of the two plots of Fig. 2-22 suggests that assuming the constant-rate injection function for CFM Run 13-05 yields a better match to the ^{22}Na breakthrough curve than the varying-rate injection function. However, most of the mismatch in the case of the varying-rate injection function occurs early in the test and is a result of the very small Peclet number in the shear zone that yields the best match to the conservative tracer (AGA) data when this injection function is used. This mismatch is also apparent for the AGA in Fig. 2-21, and it is a recurring theme throughout Figs. 2-23 to 2-28 when CFM Run 13-05 radionuclide responses are matched using the varying-rate injection function. Little weight is given to this early mismatch because it is taken to be an artifact of assuming only a single flow pathway in the shear zone, which forces this pathway to have a very small Peclet number that is dictated by the tail of the breakthrough curve. If multiple flow pathways were assumed (i.e., splitting the injected mass between two pathways with different mean residence times and Peclet numbers), this early mismatch would

disappear. In the case of the constant-rate injection assumption for CFM Run 13-05, the best-matching mean residence time and Peclet number for a single flow pathway results in a much narrower deduced conservative tracer residence time distribution in the shear zone (Fig. 2-10), which makes it inherently easier to match the early breakthrough of any constituent in the test.

2.4.3 Strontium-85

^{85}Sr was used only in the two CRR tests. It had very weak association with colloids in Run 32, and its transport in both tests was deduced to be dominated by adsorption/desorption in the matrix with negligible adsorption to shear zone surfaces and colloids. ^{85}Sr was modeled as having a much stronger interaction with the matrix than ^{22}Na. Good matches to the ^{85}Sr data in both CRR runs were obtained using similar values of the matrix adsorption and desorption rate constants, and as with ^{22}Na, the model matches were insensitive to the absolute values of the rates as long as the ratio of the rates stayed the same and the rates were relatively fast compared to transport rates through the shear zone. The model matches degraded if the rate constants became much lower than those of Table 2-4, and this was dictated by the much smaller desorption rate constant. The deduced matrix K_d value ranged from about 340 to 390 ml/g, or nearly 2 orders of magnitude greater than for ^{22}Na for the same assumptions of matrix porosity, shear-zone aperture and matrix diffusion coefficient.

2.4.4 Technetium-99

^{99}Tc was used only in CRR Run 32, although it had only a 12% association with colloids in the injection cocktail. Despite this weak association with colloids, it transported as if it were colloidal, or at least as if it did not interact with the matrix, because the assumption of reversible matrix sorption did not improve the matches to the ^{99}Tc breakthrough curve. Reversible matrix sorption should result in longer tailing relative to ^{131}I than was observed for ^{99}Tc (see, for example, the breakthrough curves of U and Np in CRR Run 32 in Fig. 2-17, which exhibit a classic matrix sorption response). Instead, ^{99}Tc behaved as if its observed transport was governed by an essentially irreversible reaction in the shear zone with a rate constant of about 0.11 ml/g-hr, assuming an effective porosity of 0.5 within the shear zone. This translates to a normalized rate constant of 0.3 hr^{-1} if the rate constant is multiplied by the mass of solids per mL of water in the shear zone, assuming a solids density of 2.65 g/ml. Given that ^{99}Tc(VI) in the form of pertechnetate anion (the form injected) is normally considered a conservative specie, the presumption is that the deduced rate constant reflects the rate of reduction of Tc(VI) to Tc(IV) in the shear zone, with the reduced oxidation state readily adsorbing or precipitating once it forms. However, this is a rather rapid rate constant for a reduction reaction that involves electron transfers, so it is unknown whether this is an appropriate explanation for the observed rate of ^{99}Tc removal from the system.

Note that if all the ^{99}Tc were associated with colloids, the deduced normalized rate constant of 0.3 hr^{-1} would correspond to the desorption rate constant of ^{99}Tc from the colloids (as indicated in Table 2-4, with a corresponding footnote). However, given that only 12% of the ^{99}Tc was initially associated with the colloids, the model results are relatively insensitive to the ^{99}Tc desorption rate constant from colloids, and in fact the desorption rate constant can vary from zero to a very large value without changing the deduced solute adsorption rate constant (or reduction rate constant) in the shear zone by very much.

2.4.5 Barium-133

^{133}Ba was used only in the two CFM tests, and its observed transport behavior could be matched reasonably well using almost the same set of parameters for each test and for each assumed injection function (in the case of Run 13-05). The only parameter that differed to achieve a match in the different tests or for the different injection functions in CFM Run 13-05 was the rate constant for desorption of ^{133}Ba from the colloids. ^{133}Ba had the lowest recovery of any radionuclide in the two tests in which it was used. It was also the only radionuclide that was best matched when adsorption and desorption was assumed to occur in the shear zone, the matrix, and on colloids (all 3 possible locations). With sorption only in the matrix, as was assumed for most other radionuclides that were not strongly associated with

colloids, ^{133}Ba was consistently predicted to break through and tail too early, and this malady could only be addressed by invoking weak reversible adsorption in the shear zone. Also, it is noteworthy that the sorption of ^{133}Ba in the matrix was essentially modeled as being irreversible because the desorption rate constant providing a good match to the data was exceedingly small (Table 2-4). The assumption of very strong but reversible sorption (over test time scales) in the matrix resulted in somewhat poorer matches to the data.

Interestingly, for CFM Runs 12-02 and 13-05, it was deduced that both the solute fraction of ^{133}Ba and the fraction adsorbed to colloids contributed significantly to the observed breakthrough curves. This also represents a departure from the modeled behavior of other radionuclides in most tests, which were deduced to either be dominated by colloid-facilitated transport or by solute transport and generally did not have significant contributions from both modes of transport. The colloid-associated fraction of ^{133}Ba was slightly more dominant in Run 12-02 than in Run 13-05 - despite the fact that the initial mass fraction associated with colloids was greater in Run 13-05 (see Figs. 2-19 and 2-24).

2.4.6 Cesium-137

^{137}Cs was used in all tests in which colloids were injected, but it was not used in the colloid-free CRR Run 31. It exhibited a bimodal breakthrough curve in CRR Run 32, which is readily explained by the colloid-associated fraction in the injection cocktail accounting for the first peak and the solute fraction accounting for the second peak. Only 8% of the ^{137}Cs mass was associated with colloids in the injection cocktail, and a majority of this mass was deduced to exit the flow system with the colloids before having a chance to desorb from the colloids. The transport of the remaining 92% of the ^{137}Cs that was injected in the solute phase was modeled as being governed by strong, fast and reversible sorption in the matrix, with effectively no adsorption occurring on shear zone surfaces. As with ^{22}Na and ^{85}Sr, the matrix adsorption and desorption rate constants listed in Table 2-4 could both be increased as long as their ratio stayed the same, but they could not both be decreased without degrading the model match to the data. The effective ^{137}Cs K_d value in the matrix was about 28,500 ml/g, assuming a matrix porosity of 0.02, a matrix diffusion coefficient of 1 x 10^{-6} cm^2/sec, and a shear zone half-aperture of 1 mm (the same assumptions used throughout this report).

For the two CFM tests, the observed ^{137}Cs breakthrough curve had only a single peak, and the ^{137}Cs transport was deduced to be dominated by colloid-facilitated transport. This result differs from CRR Run 32 mainly because there were much greater colloid associations of the ^{137}Cs in the CFM injection cocktails compared to the CRR Run 32 cocktail (see Table 2-1). These differences in colloid associations are likely attributable to the significantly lower ^{137}Cs concentrations and greater colloid concentrations in the two CFM cocktails relative to the CRR cocktail (see Table 2-1). Missana et al (2004) showed that there are abundant weak sorption sites and much less abundant strong sorption sites for ^{137}Cs onto bentonite colloids. Thus, when ^{137}Cs concentrations are low relative to colloid concentrations, most of the ^{137}Cs will become adsorbed to strong sites, but when ^{137}Cs concentration are high, the more abundant weaker sorption sites will dominate the observed bulk adsorption-desorption behavior. The predominant influence of the weaker bentonite sorption sites for the colloid-facilitated transport of relatively high ^{137}Cs concentrations in the Grimsel system was demonstrated in column experiments reported in Chapter 8 of Wang et al. (2015).

As Table 2-4 shows, whereas all the solute sorption parameters were kept identical in the model interpretations for each of the tests involving ^{137}Cs, the rate constants for the desorption of ^{137}Cs from the bentonite colloids were deduced to be over an order of magnitude smaller for the two CFM tests than for CRR Run 32. This result is considered a further reflection of the predominant influence of the stronger ^{137}Cs sorption sites on the colloids at the lower ^{137}Cs concentrations of the two CFM tests and the greater influence of the weaker sites at the higher ^{137}Cs concentrations (and somewhat lower colloid concentrations) in the CRR test. This behavior is entirely consistent with the two-site ^{137}Cs sorption model onto bentonite colloids of Missana et al (2004).

A two-site sorption-onto-colloids model was not invoked to simulate ^{137}Cs transport in the CRR and CFM tests because the initial fractions of ^{137}Cs adsorbed to weak and strong sorption sites on the colloids was not known. Rather, a single sorption site on the colloids was assumed when interpreting the tests, and the desorption rate constants were taken as a reflection of the dominant behavior of either the weak (CRR) or strong (CFM) sorption sites. It would be an interesting exercise to determine if a single set of adsorption-desorption parameters could be found for both the weak and strong sorption sites in a two-site model to predict both the initial colloid associations and the observed colloid-facilitated transport behavior of the ^{137}Cs in all the tests. Such an exercise would have to include the specification of a limited number of strong sorption sites on the colloids so that the strong sites would lose their influence at higher ^{137}Cs concentrations, as shown in Chapter 8 of Wang et al. (2015).

2.4.7 Uranium Isotopes

Uranium (U), as either ^{233}U or ^{238}U, was injected in both CRR tests and in CFM Run 13-05. It was not used in CFM Run 12-02. Interestingly, U was weakly associated with colloids in CRR Run 32, but it was strongly associated with colloids in the CFM Run 13-05 injection cocktail. The explanation for the stronger colloid association in CFM Run 13-05 is probably analogous to the explanation for the stronger association of ^{137}Cs in the CFM tests relative to CRR Run 32; i.e., the U concentrations in the CRR Run 32 injection cocktail were significantly higher than in the CFM Run 13-05 cocktail (and the colloid concentrations were slightly lower), which resulted in a greatly reduced influence of relatively low-abundance strong colloid sorption sites in the CRR test. Thus, there was essentially no colloid-facilitated transport of U in the CRR test, but colloid-facilitated transport appeared to be dominant in CFM Run 13-05. However, unlike ^{137}Cs, which could be matched in all tests using the same matrix adsorption and desorption rate constants (or K_d values), the matrix sorption parameters for U differed significantly in the CRR and CFM tests, with much stronger matrix sorption needed to match the data in the CFM tests (Table 2-4). It seems plausible that the matrix had an abundance of weak U sorption sites and a small number of strong U sorption sites, analogous to the colloids. This would explain why the apparent matrix K_d value (ratio of adsorption to desorption rate constants) for U in the two CRR tests ranged from about 20 to 30 ml/g whereas the range was 10,000 to 100,000 in CFM Run 13-05 (depending on the injection function used). Such a dramatic difference, particularly in the same dipole configuration within the shear zone, suggests an increased influence of less-abundant, stronger matrix sorption sites in CFM Run 13-05 because of the much lower U injection concentrations. The model matches to the U breakthrough curves in all tests were not improved by assuming U sorption to surfaces within the shear zone. This was even true for CRR Run 31, which had no colloids.

The rate constants for U desorption from colloids for the two different assumed injection functions for CFM Run 13-05 were in reasonably good agreement (Table 2-4), although it was necessary to increase the U desorption rate constant linearly with time throughout the test in the case of the constant-rate injection function to avoid a significant over-prediction of colloid-facilitated U transport at the end of the test. This time-dependent increase in the desorption rate constant was superimposed on a similar time-dependent increase of the colloid filtration rate constant when the constant-rate injection function was used (Section X.4.1). In contrast, a time-invariant desorption rate constant was sufficient to obtain a reasonable match to the U data when the varying-rate injection function was assumed in CFM Run 13-05. These results would seem to lend additional support to the superiority of the varying-rate injection function over the constant rate injection function for Run 13-05. However, they might also suggest that some desorption of U from the colloids occurred in the injection circulation loop prior to injection of the cocktail into the shear zone.

2.4.8 Neptunium-237

The ^{237}Np transport behavior in both CRR tests and in CFM Run 13-05 was very similar to the U transport behavior in these tests. Essentially everything that was stated for U in the preceding section also applies to ^{237}Np, with the values of best-matching rate constants (or K_d values) differing only slightly for

the two different actinides. ^{237}Np seemed to desorb from the colloids slightly faster than U in CFM Run 13-05.

^{237}Np was also used in CFM Run 12-02, which did not include the injection of a U isotope. The ^{237}Np was much less strongly associated with colloids in the Run 12-02 injection cocktail than in the Run 13-05 injection cocktail (Table 2-1), so desorption rates from colloids had little influence on the model matches to the ^{237}Np breakthrough curve in Run 12-02 as they did for Run 13-05. Rather, the ^{237}Np transport behavior in CFM Run 12-02 seemed to be dominated by a slow, essentially irreversible adsorption process occurring on shear zone surfaces, with much weaker matrix sorption interactions than in all the other tests. This slow, irreversible sorption process is considered to be indicative of ^{237}Np reduction from the Np(V) oxidation state (injected) to the Np(IV) oxidation state, which is much less soluble and more strongly adsorbing than the higher oxidation state. Reduction reactions involving electron transfers are typically slower than reactions that don't involve electron transfers. Note that the deduced normalized rate constant for the irreversible shear zone reaction in Run 12-02 was 0.11 hr^{-1}, which corresponds to a characteristic reaction time of 9.2 (1/0.11) hrs. This means that 63% of the ^{237}Np was predicted to be irreversibly sorbed/reduced in the shear zone in 9.2 hours, and 63% of the remaining ^{237}Np was predicted to react in the next 9.2 hours, and so on.

Because residence times in the shear zone were similar in CFM Runs 12-02 and 13-05, the slow, irreversible process in the shear zone (with same rate constant) was also assumed to occur for ^{237}Np in Run 13-05. However, this process had much less influence on the predicted ^{237}Np behavior in CFM Run 13-05 because ^{237}Np transport in that test was modeled as being dominated by the colloid-associated ^{237}Np, which was not a factor in Run 12-02.

The much weaker deduced matrix adsorption of ^{237}Np in CFM Run 12-02 compared to all the other tests (Table 2-4) is difficult to explain. CFM Run 12-02 was conducted in a different part of the shear zone than the other tests (Fig. 2-1), but such differences in matrix adsorption-desorption parameters were not necessary for any of the other radionuclides that were used in both shear zone locations. Attempts to achieve reasonable matches to the ^{237}Np breakthrough curve in CFM Run 12-02 using the same matrix parameters as other tests were not successful. Adjusting colloid sorption parameters had little effect because very little of the ^{237}Np in the injection cocktail was associated with colloids, and only a limited amount of adjustment of the shear zone adsorption/reduction rate could be tolerated before it became impossible to achieve good matches to the ^{237}Np data. The truncated tail of the ^{237}Np breakthrough curve in CFM Run 12-02, coupled with the lack of association of ^{237}Np with colloids, precluded a strong reversible matrix interaction for ^{237}Np because such a strong reversible interaction results in extended tailing. Also, the inclusion of an irreversible sorption/reduction reaction in the matrix (which seems logical if such a reaction is occurring the shear zone) did not improve the model matches. In fact, the inclusion of such a reaction actually forced the reversible matrix sorption reaction to become weaker to compensate, which increased the difference between the matrix parameters in CFM Run 12-02 and all other tests.

2.4.9 Thorium-232

^{232}Th was analyzed only in the two CRR tests. It was also injected into CFM Run 13-05, but as of the writing of this report, reliable results had not been reported. Although there were no colloids present in CRR Run 31, the ^{232}Th transported very much like it was facilitated by colloids with a finite desorption rate from the colloids. The ^{232}Th transport could also be interpreted as though the ^{232}Th itself was colloidal (i.e., an intrinsic colloid), with partial filtration of these colloids occurring in the shear zone. However, the observed ^{232}Th behavior is also consistent with a slow, irreversible solute adsorption reaction occurring in the shear zone, and because of the lack of colloids in CRR Run 31, the parameters listed for ^{232}Th in this test in Table 2-5 reflect this interpretation. Nonetheless, it is possible that the ^{232}Th was partially in colloidal form in the Run 31 injection cocktail, either as intrinsic colloids or as a colloidal precipitate, or perhaps adsorbed to a small (unintentional) concentration of pre-existing colloids. Indeed,

Kosakowski and Smith (2004) speculated that the transport of ^{232}Th in CRR Run 31 may have been at least partially colloidal.

It is clear from comparing the ^{232}Th breakthrough curves and recoveries in CRR Runs 31 and 32 (especially relative to ^{131}I – see Figs. 2-14 and 2-18, respectively) that the bentonite colloids in Run 32 facilitated the transport of ^{232}Th through the CRR dipole (even if part of the ^{232}Th transport in Run 31 was colloidal). Given that the ^{232}Th was almost entirely associated with colloids in the Run 32 injection cocktail, the ^{232}Th breakthrough curve in this test was interpreted as being governed by the rate of desorption of ^{232}Th from the colloids. The ^{232}Th sorption parameters for the shear zone and matrix in CRR Run 32 were set so that any ^{232}Th that desorbed from the colloids rapidly became associated with these surfaces for the remainder of the test. Note that the ^{232}Th parameters listed in Table 2-5 for CRR Run 32 reflect that the ^{232}Th that was desorbed from colloids in this test did not follow the same shear zone transport behavior as in CRR Run 31 (i.e., a slow, irreversible reaction in the shear zone). If this slow, reversible reaction were assumed to apply, it would have the effect of increasing the colloid desorption rate constant in Run 32 because some of the ^{232}Th desorbed from colloids would then be predicted to transport through the system as a solute.

It should be noted that the colloid-facilitated transport of ^{232}Th was evaluated in 3 other CFM tests conducted in the same flow configuration as CFM Run 12-02, but without other radionuclides (CFM Runs 08-01, 10-01 and 10-03). Interpretations of these tests are reported in Chapter 2 of Wang et al. (2013). In general, it was found that the governing rate constant for desorption of ^{232}Th from the colloids in these tests was about an order of magnitude smaller than the rate constant reported for CRR Run 32 in Table 2-5 and similar in magnitude to the rate constants deduced for Am and Pu in CFM Runs 12-02 and 13-05 that are listed in Table 2-5.

2.4.10 Americium Isotopes

Americium (Am) isotopes (either ^{241}Am or ^{243}Am) were injected in all the tests. Am transported in a very similar manner as ^{232}Th, with its transport in CRR Run 31 (without colloids) interpreted as being governed by a slow, irreversible adsorption reaction in the shear zone, and its transport in all other tests as governed by a slow desorption reaction from colloids with rapid and strong adsorption of the Am to both shear zone and matrix surfaces once it desorbed from colloids. As for ^{232}Th, transport of Am partially in a colloidal state cannot be ruled out for CRR Run 31; this possibility was also speculated by Kosakowski and Smith (2004). Am was interpreted as having a slightly slower solute shear-zone reaction rate in CRR Run 31 than ^{232}Th but as having a slightly faster desorption rate from colloids than ^{232}Th in CRR Run 32 (Table 2-5). However, these differences may not be significant, as they could be swamped by errors associated with analytical measurements, including measurements of radionuclide associations with colloids in the Run 32 injection cocktail (which can have a significant impact on the deduced desorption rate constants).

The interpretations of Am transport in CFM Runs 12-02 and 13-05 were generally consistent with that of CRR Run 32, although the rate constant for Am desorption from colloids was notably smaller in the CFM tests than in the CRR test. Whereas differences in the observed colloid-facilitated transport of Cs and U in the CRR and CFM tests were qualitatively explained by the greater influence of strong colloid sorption sites at the lower injection concentrations in the CFM tests (Sections X.4.6 and X.4.7), no such explanation can be invoked for Am because its injection concentrations in all the tests were quite similar. Nonetheless, it is still possible that there were both strong and weak Am sorption sites on the colloids, or more specifically, sites with slower and faster desorption rate constants. In this case, the faster sites would have more influence on the bulk behavior observed in the shorter-duration CRR test, and the slower sites would have greater influence in the CFM tests with longer shear-zone residence times. The fact that the colloid concentrations were about five times lower in the CRR test than in the CFM tests may have also resulted in a greater influence of weaker colloid sorption sites on Am transport (expressed as faster Am desorption rates from colloids) in the CRR tests.

The Am desorption rate constant from colloids in CFM Run 13-05 was smaller than in CFM Run 12-02 despite the fact that the residence time for the majority of the injected mass was shorter in the former test than the latter test. Although the differences in the desorption rate constants may not be significant because of errors and uncertainties in the data, one possible explanation for this result is that the CFM Run 13-05 injection cocktail was "aged" for 401 days before its injection whereas the Run 12-02 injection cocktail was injected within 7 days of its preparation. This would have given the Am more time to become associated with strong sorption sites on the colloids in the Run 13-05 cocktail, thus resulting in a slower apparent rate constant for desorption from colloids in this test. However, it is also possible that the desorption rate constants were different in the two tests simply because the tests were conducted in different parts of the shear zone.

Finally, it should be noted that, as for U and Np in CFM Run 13-05, the Am rate constant for desorption from colloids when a constant-rate injection function was assumed in Run 13-05 had to be specified as steadily increasing with time to obtain a reasonable match to the Am breakthrough curve. Without such a time-dependent desorption rate constant, the Am concentrations near the end of the test were significantly over-predicted.

2.4.11 Plutonium Isotopes

Plutonium (Pu) isotopes (either ^{238}Pu, ^{242}Pu or ^{244}Pu, or some combination of these) were injected in all the tests. Pu transported in a manner very similar manner to ^{232}Th and Am, with its transport in CRR Run 31 (without colloids) interpreted as being governed by a slow, irreversible adsorption reaction in the shear zone, and its transport in all other tests as being governed by a slow desorption reaction from colloids with rapid and strong adsorption of the Pu to both shear zone and matrix surfaces once it desorbed from the colloids. Pu was interpreted as having the fastest shear-zone solute reaction rate of these three radionuclides in CRR Run 31, and also as having the slowest rate of desorption from colloids in all the other tests (Table 2-5). However, its desorption rate from colloids was indistinguishable from that of Am in CFM Run 13-05.

All of the statements about Am transport in the last two paragraphs of Section X.4.10 also apply to Pu, so they are not repeated here. However, one exception is that the rate constants for desorption of Pu from colloids were deduced to be almost identical in CFM Runs 12-02 and 13-05, whereas this desorption rate constant for Am was deduced to be somewhat smaller in Run 13-05 than in Run 12-02.

2.5 Discussion and Conclusions

The comprehensive model interpretations presented in this report for all the CRR and CFM tests involving reactive radionuclides at the Grimsel Test Site yield some valuable insights for modeling of radionuclide transport, and particularly of colloid-facilitated radionuclide transport, in saturated fractured crystalline rocks. Nonuniqueness in the model interpretations was reduced by minimizing the differences in the reactive transport parameter estimates for a given radionuclide in different tests, with the rationale being that all the tests were conducted within a few meters of each other in the same shear zone, so the model parameters for a given radionuclide should be similar in all tests. However, nonuniqueness in the parameter estimates could not be completely eliminated, particularly for parameters for which the model simulations of a given radionuclide were insensitive. Also, it should be made clear that a rigorous parameter estimation algorithm was not applied, so the parameter estimates of Tables 2-3 through 2-5 should not be considered formally optimized.

For the most part, a relatively consistent set of reactive transport parameter estimates was obtained for each radionuclide, and these could be readily applied to all CRR or CFM tests in which that radionuclide was injected. However, adjustments to the most sensitive reactive transport parameters were inevitably necessary to improve model matches to breakthrough curves for a given radionuclide when interpreting different tests. Some of these adjustments can be readily justified as being attributable to differences in

injection concentrations of the radionuclides or to differences in the locations of the tests in the shear zone.

The conclusions from this work are summarized in the remainder of this section.

The transport of the FEBEX bentonite colloids in all the tests involving radionuclides could be explained quite well with an irreversible filtration rate constant, which was deduced to be similar in magnitude in each of the tests. No colloid filtration was apparent in the very short-duration CRR Run 32, but the predicted amount of filtration in this test was negligible when the filtration rate constants deduced from the longer-duration CFM tests were applied, so the lack of observed filtration in the CRR test is considered to be consistent with the CFM test results. In effect, CRR Run 32 was too short to provide constrained estimates of colloid filtration rate constants, and this test should not be used to draw any conclusions about colloid filtration rates in the MI shear zone other than placing an upper bound on what the filtration rate might be.

The transport of radionuclides that were not strongly associated with colloids but nevertheless had significant interactions with rock surfaces (^{22}Na, ^{85}Sr, ^{133}Ba, U and Np in tests other than CFM Run 13-05, and ^{137}Cs at high concentrations or in the absence of colloids) appeared to be dominated by sorption and desorption in the matrix (after diffusion out of the shear zone), rather than by sorption and desorption within the shear zone itself. This was true despite the relatively small matrix porosity of the Grimsel granodiorite, which should presumably limit diffusion of radionuclides into the matrix. In most cases, the matrix adsorption and desorption rates could be considered rapid relative to conservative tracer residence times in the tests, so the sorptive interaction in the matrix could be approximated with a partition coefficient, or K_d value (ml/g), rather than explicitly accounting for rate-limited adsorption and desorption reactions. This result is consistent with the observations of Andersson et al. (2002) in the fractured granite system at the Aspö site in Sweden, where it was also observed that strongly-adsorbing radionuclides tended to behave as if sorption in the matrix dominated their transport behavior despite a small matrix porosity.

The transport of radionuclides that were strongly associated with colloids (^{232}Th, Am, Pu) tended to be governed by their rates of desorption from the colloids, with the assumption that once the radionuclides desorbed from the colloids, they quickly became strongly associated with immobile surfaces in the system (either in the shear zone or in the matrix), thus removing them from further participation in the test. The mass recoveries of these radionuclides were governed by their colloid desorption rate constants, with larger desorption rate constants resulting in lower recoveries.

In the absence of colloids (CRR Run 31), the transport of radionuclides that were otherwise strongly associated with colloids (^{232}Th, Am, Pu) appeared to be governed by a slow, essentially irreversible reaction occurring in the shear zone. There was little evidence that these radionuclides interacted at all with the matrix, although a limited amount of matrix interaction cannot be ruled out. The transport behavior of these radionuclides in the absence of colloids was also consistent with colloid-facilitated transport with a finite desorption rate from the colloids or with transport of intrinsic colloids (e.g., colloidal precipitates) with a finite filtration rate of the colloids. These possibilities are considered plausible, particularly given the low solubilities and apparent lack of matrix interactions of these radionuclides despite the strong matrix interactions observed for other radionuclides.

The injection function for CFM Run 13-05 had more uncertainty than any other CFM tracer test previously conducted with a circulating injection loop (see Chapter 2, Wang et al., 2013), because the deduced conservative tracer mass associated with the injection function was about 20% higher than the reported injection mass. This uncertainty was addressed by performing model interpretations assuming (1) a varying-rate injection function that closely followed the observed injection function behavior but with concentrations scaled down by 20% to preserve mass and (2) a mass-conserving constant-rate injection function at the injection rate observed over the last several hundred hours of the test. Because the model interpretations assuming the latter injection function required both a time-dependent colloid

filtration rate constant and time-dependent colloid desorption rate constants for U, ^{237}Np, Am and Pu, the varying-rate injection function is considered to be the more plausible function. It is recommended that the reactive transport parameters for radionculides deduced assuming this injection function in CFM Run 13-05 be given more credence than those obtained assuming the constant rate function.

Although it was hoped that the tests would provide some insights into the time and distance scaling behavior of colloid filtration rate constants, it appears that little can be said about such scaling behavior. The colloid filtration rate constants in the CFM tests were deduced to be quite similar in the two test configurations. The CRR tests had much shorter time scales than the CFM tests, but there was no observed colloid filtration in CRR Run 32, so it was not possible to obtain a constrained estimate of the colloid filtration rate constant in this test. The reader is referred to the Chapter on CFM test interpretations in Chapter 2 of Wang et al. (2013) for a discussion of apparent time-scale dependence of colloid filtration rate constants observed in non-radionuclide CFM tests that were conducted in the same configuration as CFM Run 12-02 but with varying residence times. That discussion, which includes CFM Run 12-02 as one of the tests considered, provides more insights into the scaling behavior of colloid filtration rates than can be gleaned from the radionuclide tests described in this report.

The rate constants for desorption of radionuclides from bentonite colloids were consistently greater for ^{137}Cs, Am and Pu in the shorter-duration CRR Run 32 than in either of the longer-duration CFM tests. These were the only colloid-facilitated radionuclides for which comparisons between the CRR and CFM tests were possible. The suggested time-scale dependence of the desorption rate constants may be an artifact of the assumption in the interpretative modeling that there was only a single type of radionuclide sorption site on the colloids. For ^{137}Cs, there is independent evidence (Missana et al., 2004; Chapter 2 in Wang et al., 2013) that at least two different sorption sites of different strengths exist on the bentonite colloids, with the stronger sorption site having much lower abundance on the colloid surfaces. In this case, the observed ^{137}Cs behavior can be at least partially attributed to the much higher concentration of Cs in the injection cocktail in the CRR test than in the CFM tests. The higher Cs concentration in the CRR test would be expected to result in a predominant influence of the more abundant weaker sorption sites on the colloids, whereas there would be expected to be a greater influence of the less-abundant, stronger sorption sites on the colloids in the CFM tests. The fact that the Cs was much more strongly associated with colloids in the CFM injection cocktails than in the CRR injection cocktail is consistent with this explanation. For Am and Pu, the reasons for the larger apparent desorption rate constants in the CRR test cannot be attributed to differences in concentrations of the radionuclides in the injection cocktails because the concentrations in all cocktails were similar. However, the smaller concentration of colloids in the CRR Run 32 cocktail relative to the CFM tests (by about a factor of five) may have still resulted in a greater percentage of Am and Pu in the CRR test being associated with weaker colloid sorption sites than in the CFM tests.

The model interpretations documented in this report are generally consistent with the interpretations of CRR Runs 31 and 32 reported by Kosakowski and Smith (2004), who did a somewhat more sophisticated set of analyses that included both 1-D and 2-D models, with the latter accounting for 2-D flow through the shear zone around the CRR dipole.

It is of interest to compare the Am and Pu desorption rate constants from colloids in the GTS field tests to the rates measured in the laboratory experiments of Huber et al. (2011). Huber et al. (2011) measured desorption rate constants for Am and Pu from colloids in a ternary system involving the bentonite colloids, fracture fill material from GTS, and a synthetic GTS ground water at two different starting concentrations of the nuclides. Using the Am and Pu injection concentrations in the GTS tests, the desorption rate constants predicted by the experiments of Huber et al. (2011) would be approximately 0.01 hr^{-1} for Am and 0.002 hr^{-1} for Pu. The desorption rate constants deduced in CFM Runs 12-02 and 13-05 were in reasonably good agreement with these values, although they tended to be slightly higher than in the laboratory tests. This agreement is nonetheless considered to be quite good, and the higher

rates in the field experiments could just reflect that the shear zone surface area available for competitive sorption with the colloids was somewhat higher in the field test than in the lab experiments.

Generally speaking, the results of the GTS colloid-facilitated radionuclide transport tests indicate that the actinides Th, Pu and Am, and the fission product ^{137}Cs, are the most likely radionuclides to experience colloid-facilitated transport over long time and distance scales (at least for bentonite colloids in a fractured crystalline setting). However, the time and distance scales of the GTS tests were very short relative to time and distance scales of relevance for nuclear waste repository performance assessments, so it should not necessarily be concluded that colloid-facilitated transport of these radionuclides will be a concern in such performance assessments. The GTS results collectively suggest that colloid-facilitated radionuclide transport is likely to be more efficient at lower radionuclide concentrations than at higher concentrations because a greater fraction of the radionuclide mass will then tend to become associated with strong, low abundance adsorption sites on the colloids. Stated differently, the GTS results suggest that colloid-facilitated transport over very long time and distance scales is much more likely to involve very small concentrations of radionuclides rather than large concentrations.

2.6 Acknowledgments

The author is grateful to CFM project participants who provided access to the CRR and CFM test data as well as descriptions of the conduct of the tracer tests. In particular, special thanks go to Thorsten Schafer (KIT), Bill Lanyon (Fracture Systems, Ltd.), and Ingo Blechschmidt (NAGRA). Funding for this report was provided by the U.S. Department of Energy, Nuclear Energy Office, Fuel Cycle R&D Program, Used Fuel Disposition Campaign.

2.7 References

Andersson P., Byegard J., Dershowitz W., Doe T., Hermanson J., Meier P., Tullborg E., and Winberg A. (2002) *TRUE Block Scale project. Final report 1(4). Characterisation and model development*. Technical Report 02-13, Swed. Nucl. Fuel and Waste Management Co., Stockholm.

Huber F., Kunze P, Geckeis H., and Schäfer T. (2011) Sorption reversibility kinetics in the ternary system radionuclide-bentonite colloids/nanoparticles-granite fracture filling material, *Appl. Geochem.*, 26, 2226-2237.

Kontar K. and Gräfe K. (2012) *GTS Phase VI CFM Project Tracer Test Run 12-02,* Q*uick-Look Report,* AN 12-302, CFM Project, Switzerland.

Kontar K., Gräfe K., and Rösli U. (2013) *GTS Phase VI, CFM Phase 2, Tracer Test Run 13-05,* Q*uick-Look Report,* AN 13-617, CFM Project, Switzerland.

Kontar K. and Rösli U. (2014) *GTS Phase VI, CFM Project, Long-Term In-Situ Test (LIT): Bentonite source term packer system, surface equipment extension, QA and installation report*, AN 14-362, CFM Project, Switzerland.

Kosakowski G. and Smith P. (2004) *Modelling the Transport of Solutes and Colloids in a Water-Conducting Shear Zone the Grimsel Test Site*, Nagra Techncial Report 04-01, Nagra, Wettingen, Switzerland.

Missana T., Garcia-Gutierrez M., and Alonso U. (2004) Kinetics and irreversibility of cesium and uranium sorption onto bentonite colloids in a deep granitic environment, *Appl. Clay Sci.*, 26, 137-150.

Möri A. (Ed.) (2004) *The CRR final project report series I: Description of the Field Phase – Methodologies and Raw Data*. Nagra Technical Report NTB 03-01. Nagra, Wettingen, Switzerland.

Reimus P. W., Pohll G., Mihevc T., Chapman J., Papelis L., Lyles B., Kosinski S., Niswonger R., and Sanders P. (2003) Testing and parameterizing a conceptual model for radionuclide transport in a fractured granite using multiple tracers in a forced-gradient test, *Water Resour. Res.*, 39(12), 1350, doi:10.1029/2002WR001597.

Reinholdt M. X., Brendle J., Tuilier M-H., Kaliaguine S., and Ambroise E. (2013) Hydrothermal synthesis and characterization of Ni-Al montmorillonite-like phyllosilicates, *Nanomaterials*, 3, 48-69, doi:10.3390/nano3010048.

Taylor G. I. (1953) Dispersion of soluble matter in solvent flowing slowly through a tube, *Proc. Roy. Soc.* A., 219, 186–203.

Wang Y., et al. (2013) *Used Fuel Disposition Campaign Milestone Report FCRD-UFD-2013-000628; Chapter 2, Interpretations of Colloid-Facilitated Transport Experiments at the Grimsel Test Site from 2008 through 2012*. Natural System Evaluation and Tool Development – International Collaborations: FY13 Progress Report.

Wang Y., et al. (2015) *Used Fuel Disposition Campaign Milestone Report FCRD-UFD-2015-000125; Chapter 8, Laboratory Investigation of Colloid Facilitated Transport of Cesium by Bentonite Colloids in a Crystalline Rock System*. Used Fuel Disposal in Crystalline Rocks: FY15 Progress Report.